Thermodynamic and optical investigations of transport phenomena in lipid monolayers

I n a u g u r a l d i s s e r t a t i o n

zur

Erlangung des akademischen Grades eines

Doktors der Naturwissenschaften (Dr. rer. nat.)

der

Mathematisch-Naturwissenschaftlichen Fakultät

der

Universität Greifswald

vorgelegt von

Florian Gellert

Greifswald, 09.08.2023

Dekan*in: Prof. Dr. Gerald Kerth

1. Gutachter*in: Prof. Dr. Christiane A. Helm

2. Gutachter*in: Prof. Dr. Doris Vollmer

Tag der Promotion: 12.12.2023

Contents

1. Introduction ..... - 1 -

1.1. Transport of reactive oxygen species from the subphase towards a lipid monolayer ..... - 2 -

1.2. Transport of surfactant material in the LE-phase towards domain boundaries ..... - 3 -

1.2.1. Non-equilibrium growth of two-dimensional lipid monolayer domains – a chronological overview of the findings from the past ..... - 3 -

1.2.2. Non-equilibrium growth of two-dimensional lipid monolayer domains – what remains to be investigated ..... - 5 -

2. Theoretical background ..... - 7 -

2.1. Monolayers at the air-water interface ..... - 7 -

2.2. Hydrodynamic classification of the erucic acid monolayers ..... - 8 -

2.2.1. The Navier-Stokes equations - a brief overview ..... - 9 -

2.2.2. Preconditions for Marangoni flow ..... - 11 -

2.3. The (modified) Ivantsov solution ..... - 14 -

2.3.1. Derivation of the local normalized supersaturation Δ according to Ivantsov ..... - 14 -

2.3.2. The modified Ivantsov solution (diffusion plus convection) ..... - 17 -

3. Materials and Methods ..... - 20 -

3.1. Lipids and fatty acids ..... - 20 -

3.2. Langmuir Blodgett trough and isotherms ..... - 21 -

3.3. Brewster angle microscopy ..... - 23 -

4. Conclusions ..... - 25 -

4.1. Article 1: Oxidation of Unsaturated Phospholipids: A Monolayer Study ..... - 25 -

4.2. Article 2: Seaweed and Dendritic Growth in Unsaturated Fatty Acid Monolayers ..... - 26 -

4.3. Article 3: Influence of Surface Flows on the Shape of Fractal Domains ..... - 27 -

5. Further investigations and outlook ..... - 29 -

5.1. Comparison of hydrodynamic theory with results ..... - 29 -

5.1.1. Boussinesq numbers ..... - 29 -

5.1.2. Cross-over length between diffusive and advective transport ..... - 29 -

5.2. Comparison of Ivantsov theory with results ..... - 30 -

5.2.1. Classification of experimental results according to the Péclet numbers ..... - 30 -

5.2.2. Determination of the diffusion zone ..... - 31 -

5.3. The big picture ..... - 34 -

6. Summary ..... - 36 -

7. Bibliography ..... - 40 -

8. Symbol directory ..... - 45 -

9. Abbreviations ..... - 48 -
10. Author contributions ..... - 49 -
11. Scientific achievements (Publications & Conferences) ..... - 50 -
11.1. Publications ..... - 50 -
11.2. Conference Contributions ..... - 50 -
11.2.1. Conference talks ..... - 50 -
11.2.2. Poster presentations ..... - 51 -
12. Publications ..... - 52 -
12.1. Article 1 ..... - 52 -
12.2. Article 2 ..... - 61 -
12.3. Article 3 ..... - 79 -
13. Eigenständigkeitserklärung ..... - 88 -

Dedicated to my wife.

1. Introduction

Self-assembly[1, 2] is a fascinating natural phenomenon. Disordered components arrange to a more ordered system spontaneously, leading to an energetically more favorable one. A superior driving mechanism determines the molecular alignment with the environment. One of the prime examples of self-assembly are amphiphilic molecules.[3, 4] For instance, lipids build vesicles or bilayers spontaneously, when dispersed in water.[5] The driving mechanism is the hydrophobic effect.[4, 6, 7] Consequently, hydrophobic and hydrophilic parts of the lipids are strictly separated from each other, giving the cell membrane its barrier function.[8]

When lipids are spread on a water surface, a monolayer forms. Again, an ordering of the molecules takes place: The hydrophilic, polar head group points towards the water surface and the hydrophobic acyl chains are directed towards the air. Since a biological membrane can be considered as two weakly coupled monolayers, lipid monolayers have proven to be powerful model systems to study many aspects of membrane biophysics.[9, 10] Dependent on the lateral pressure and temperature, these lipids exist in different phases.[9, 11] A phase transition can be enforced by compressing the lipid monolayer. The most important transition is from the liquid expanded phase (LE-phase) to the liquid condensed phase (LC-phase).[9, 11] From a biological perspective, the cell membranes need to preserve their fluidic state to maintain their function and interaction with their surroundings.[12] Therefore, the cell has mechanisms to stay in the LE-phase.[13, 14]

At the LC-phase, the lipids are packed denser, which allows the formation of two-dimensional structures, the so-called domains.[15, 16] They originate from nuclides, which are caused by density fluctuations within the monolayer. The nuclides are stable and will not decay anymore as soon as the gained free enthalpy ΔG (released either by latent heat or impurities) exceeds the energy loss of building a boundary by ordering the lipid molecules between the domains in the LC-phase and the LE-phase. Therefore, one can find a critical domain radius r from which the domain will start growing, provided that surfactant molecules (lipid or fatty acid molecules) will be transported towards its boundary.

Usually, diffusion of the molecules in the LE-phase is the main transport mechanism, leading to circular or bean-shaped domains, respectively. The so gained boundary minimization is a consequence of the line tension γ,[17, 18] which pulls the molecules together at the domain edge. However, far from thermodynamic equilibrium, diffusion is not the only transport process. Hydrodynamic and surface flows respectively arise and lead to instabilities at the LE/LC boundary of the domain.[19, 20] Such a rippled boundary eventually causes fractal growth.

This work investigates several mechanisms of how material will be transported towards the lipid monolayer and the domains in particular and its consequences on the molecular structure and domain shape, respectively. Particularly suitable for these investigations is the combination of a Langmuir Blodgett trough[11] with a Brewster angle microscope (BAM):[21-23] Once the lipids are spread on an aqueous (salt) solution in a Teflon trough, the lateral pressure π can be easily adjusted by compressing the film.

Dependent on the provided area, the lipids exist in the LE- or LC-phase, respectively. The phase behavior can be studied by recording an area vs. lateral pressure curve ($\pi - A$ plot) during compression at constant temperature, which is called an isotherm.[11] Simultaneously, the film at the air-water interface is optically observed with a BAM. The recording of videos allows a time-resolved investigation of the formation and growth of the domains.

The next sections of chapter 1 provide an overview of the issues addressed in this thesis. The achieved findings led to three publications (articles 1-3). Chapter 2 introduces the underlying theory to readers who are unfamiliar with hydrodynamics and Ivantsov theory. In chapter 3, I present the materials and methods I used for this thesis. Chapter 4 contains the conclusions of each article. Since not all the data is yet published, additional findings are presented and discussed in Chapter 5. Chapter 6 summarizes the achievements of the whole thesis. Chapters 7-9 comprises the bibliography, a symbol directory and a summary of the introduced abbreviations. In chapters 10 and 11, I list the author contributions and my scientific achievements. Copies of the published articles can be found in chapter 12. Chapter 13 and 14 contain the "Eigenständigkeitserklärung" and my curriculum vitae. Finally, I conclude my thesis with an acknowledgement to all the people who contributed to this work.

1.1. Transport of reactive oxygen species from the subphase towards a lipid monolayer

In article 1, vertical diffusion of reactive oxygen species[24, 25] (ROS) in the subphase towards a phospholipid monolayer and its consequences on molecular structure was studied. This is of high biological relevance, since lipid oxidation[26] alters physical properties of the membrane,[27] like fluidity[28] or permeability[29, 30] and ultimately may lead to cell death.[31] Especially interesting is the question whether the ROS attack the lipid molecules at the head group or at the acyl chains, both of which can be the case.[32-35] If the latter was the case, a subsequent question arises: what is the influence of the position and the number of the double bonds? To address this issue, I compared different phospholipids with a different number of double bonds at different positions at its acyl chains.

In order to create the reactive hydroxyl ($\cdot$OH) ions via the Fenton reaction,[36, 37] iron had to be added to the subphase in earlier studies.[38, 39] Unfortunately, the iron itself influences the lipids during peroxidation.[40] Further, it is known that free iron ions are harmful for the cell.[41-43] Therefore, I have chosen another approach: I used a highly hydrogen peroxide (H_2O_2) enriched phosphate buffered saline (PBS) solution as a precursor for more reactive oxygen species.

To facilitate the thus produced ROS to reach the lipid acyl chains, the lipid monolayer was expanded during H_2O_2 treatment time.[44] Then, the lipids were compressed after a defined waiting time. This allowed me to study the pressure dependence of the lipid peroxidation in terms of the measured isotherms.

Increased ROS concentrations disrupt cell signaling and may lead to cell- and DNA damage.[45] It was therefore important to make a prediction of the $\cdot$OH concentration in the system. Since it was difficult to calculate the concentration of hydroxyl radicals present in the subphase directly, I found a way to estimate it indirectly: the relative molecular area increase observed in the isotherm[46, 47] proved to be a suitable measure for oxidation.

I was also interested in the reaction kinetics. Is there a limiting factor, leading to a slowdown of the reaction? I addressed this question by varying the ROS treatment times of the lipids. From this, I was able to estimate time scales of diffusion. Inspired by a ROS study with lipid vesicles,[48-50] I finally propose a model of how the lipid structure in monolayers alters after such a ROS attack.

1.2. Transport of surfactant material in the LE-phase towards domain boundaries

Article 2 and article 3 deal with lateral transport of surfactant material in the LE-phase towards the domain boundaries. Two-dimensional domain growth differs from three-dimensional crystal growth in many respects. The main difference is that in two-dimensional monolayers at the air-water interface, the latent heat can diffuse away vertically from the growing boundaries, since the Langmuir trough acts as a thermal reservoir.[19] Consequently, the diffusion of heat and molecules, respectively, in Langmuir monolayers are completely decoupled.[51] Hence, other transport mechanisms than the diffusion of the latent heat away from the domain boundary are responsible for fractal growth. Many important contributions to fractal and dendritic domain growth in Langmuir monolayers have been made in the last decades. The following sections give an overview of the discoveries and explanations of non-equilibrium growth of such two-dimensional structures, on which this work is based:

1.2.1. Non-equilibrium growth of two-dimensional lipid monolayer domains – a chronological overview of the findings from the past

Pioneering work has been done by Miller, Knoll and Möhwald (1986):[52] They observed fractal growth for a phospholipid monolayer (DMPE) with fluorescence microscopy, when the monolayers were exposed to non-equilibrium conditions. Jumps in lateral pressure ($\Delta\pi \sim 0.5\, mN/m$) led to a sudden increase in supersaturation. In their experiment, the dye (fluorescent marker) served as surface-active impurity. Miller, Knoll and Möhwald showed that the phase transition pressure increased with the amount of dye. They concluded that domain growth is limited by diffusion of the dye away from the interface in the LE-phase: During growth, the dye squeezes out of the domain and accumulates at the phase boundary. This prevents further growth and eventually leads to a directional solidification.

Miller and Möhwald (1987)[51] later introduced the line tension γ[18] at the boundary of domains as a crucial element for domain shaping. Line tension is reduced with increasing impurity (dye) concentration. Consequently, considerably more critical nuclei were formed at higher dye content. The reason for this is the lowering of the free energy necessary for the formation of a critical nucleus when line tension is reduced. Concluding, since impurities cause a melting temperature reduction (or lateral pressure increase), their enrichment at the interface inhibits further crystal growth. The authors pointed out the completely decoupled diffusion of heat and molecules in Langmuir monolayers: Heat diffuses into the subphase, whereas molecular diffusion is strictly confined to two dimensions. Therefore, they assumed that structures as well as the determining transport process are two-dimensional.

Suresh, Nittmann and Rondelez (1988)[53] confirmed the diffusive solidification process with experiments on myristic acid monolayers: They distinguished between two possible diffusion processes: Either thermal diffusion of the latent heat away from the phase boundary or mass transport in the presence of concentration gradients towards the phase boundary. The authors introduced the temperature dependence of the line tension, which is decreasing with increasing temperature.[54] By varying the temperature, they could generate different domain patterns. Furthermore, in their experiments, they observed fractal structures even at very low dye concentrations (~ 0.05 %). Thus, they concluded that not the dye but the pure species itself undergoes Brownian diffusion within the monolayer.

From three-dimensional growing alloys it is known, that the product of tip radius R and growth velocity v_{growth} is a constant ($R^2 \cdot v_{growth} = const.$, or $R \cdot v_{growth} = const.$, respectively).[55] Akamatsu, Bouloussa, To and Rondelez (1992)[56] proved that this is true also for two-dimensional monolayers. They introduced the subphase viscosity η, which scales as the inverse of the diffusion coefficient of the surfactant molecules in the LE-phase D_{LE}. Using water-glycerol mixtures (30-70 vol %) for the monolayer subphase, they were able to increase η by a factor of 2-100. They observed that all qualitative geometrical features of the LE/LC phase transition stayed the same as on pure water, but the tip velocity v_{growth} and tip radius R decreased by increasing η at a fixed compression speed v_C. To my knowledge, these authors were the first who pointed out the importance of hydrodynamic coupling between the amphiphilic motions within the monolayer and the bulk flow in the subphase: lateral diffusion therefore cannot be regarded as the only process enabling domain growth.

Israelachvili (1994)[16] mentioned that many $\pi - A$ isotherms reproducibly show non-horizontal lines of the coexistence regime. These are inconsistent with a first-order phase transition or with the coexistence of two thermodynamic phases. The author of this story explained this behavior with the existence of small surface micelles or "hemimicelles" in the monolayers.

Gehlert and Vollhardt (1997)[57] generated a high supersaturation with a fast compression of the monolayer in 1-monopalmitoylrac-glycerol monolayers. Consequently, the degree of branching of the domains correlated with the supersaturation and compression speed, respectively. They also assigned the dendritic shaped domains to a growth anisotropy, which is due to the favored incorporation of molecules in the condensed phase in defined directions. When they stopped their compression, the domain shapes relaxed into circular equilibrium shape. This is indicative for the high line tension of their substance. A comparison of grazing incidence X-ray diffraction study (Weidemann, Gehlert and Vollhardt (1995))[58] with their BAM pictures revealed that the arms of a dendrite are oriented parallel to the azimuthal chain tilt direction. They therefore concluded that the growth direction of dendrites is along the densest lattice rows.

Iimura, Yamauchi, Tsuchiya, Kato and Suzuki (2001)[59] observed a six-fold shape of the emerging domains of erucic acid monolayers (a fatty unsaturated acid with one double bond, adjacent to the 13th carbon atom of its acyl chain) which showed dendritic behavior for high supersaturations. Like Gehlert and Vollhardt (1997)[57], they emphasized packing limitations due to the cis-double bond in the hydrocarbon chain: It prevents rotation of the two parts of the molecule, leading to a constrained packing into the two-dimensional crystal with a kink.

This kink in turn weakens the attractive interaction among the chains. Therefore, the incorporation rate is not only reduced, moreover the bent shape of the cis unsaturated chain restricts the movement and reorientation of already incorporated molecules to the boundary of the condensed phase to achieve minimum line tension.[59] In their explanation, dendritic growth is therefore favored due to the low mobility of already incorporated molecules.

Flores, Poiré, Garza and Castillo (2006)[60] investigated monolayers of saturated lipids, namely dioctadecylamine, ethyl palmitate, and ethyl stearate. Their experiments started with round domains, followed by an abrupt lateral pressure jump caused by fast compression up to $\Delta\pi \sim 5\, mN/m$. They observed a morphology transition from tip splitting to side branching with increasing height of the pressure jumps. In addition, they could see doublons, which were theoretically predicted by Ihle and Müller Krumb-Haar (1994).[55, 61] They also mentioned the anisotropy as a requirement in the interfacial dynamics for dendritic growth. Bruinsma et al.[19] developed a theory, based on hydrodynamics, in order to describe growth instabilities, introducing the Marangoni flow. Flores, Poiré, Garza and Castillo referred to this theory and provided first experimental evidence.

Gutierrez-Campos, Diaz-Leines and Castillo (2010)[20] later stated that there is indeed hydrodynamic transport of amphiphiles, superimposing diffusion. By means of particle tracking of hydrophobized silica microspheres, they supplied evidence of the existence of Marangoni flow towards the domain boundaries, theoretically explained by Bruinsma et al.[19]: Differences in line tension γ, driven by concentration gradients within the monolayer and close to domains, generated a hydrodynamic flow. According to the theory of Bruinsma et al., the dominant growth regime is determined by surface or viscous dissipations. This classification is done by means of the Boussinesq number $Bq = q\zeta$, whereby q is a typical wavenumber of the system and $\zeta = \eta_S/\eta$ is the ratio of surface viscosity to bulk viscosity. They achieved values of the order of $Bq \sim 0.1 - 0.5$ which means that bulk viscous dissipation was the dominating effect in their experiments ($Bq < 1$). Adding glycerol to the subphase increased the bulk viscosity, such that the measured flow was reduced.

1.2.2. Non-equilibrium growth of two-dimensional lipid monolayer domains – what remains to be investigated

In this work, I chose erucic acid monolayers as a representative system of lipids. It is well characterized both in the LE- and in the LC-phase[62, 63] and its low line tension favors fractal growth. Even though this specific acid is not a constituent of the human cell membrane, the feature of low line tension turns it into a suitable model system. Thus, highly dynamic biological processes such as breathing[64-66] and the formation of teardrops[67] can be investigated in terms of domain shaping. I emulated these dynamic processes by a high, continuous compression speed v_C of the monolayer. The consequence of such a non-equilibrium process are different kinds of flows in and under the monolayer respectively, caused by hydrodynamic coupling of the monolayer to the subphase. I was interested in how these flows affect domain shape and whether there exist morphology transitions at a certain strength of flow. Recording BAM videos allowed me the time-resolved analysis of the evolution of domains.

It is known from earlier experiments of slowly compressed lipid monolayers that the growth of the domains starts, when nucleation is completed. However, at fast compression speeds, I

noticed an unexpected continuous nucleation in the LE/LC coexistence regime for erucic acid monolayers. This feature would contribute to the anisotropy in the fluid phase. It was of particular interest to me to investigate the consequences of such an anisotropy, like the creation of superimposed surface flows and locally differing supersaturations. I am therefore emphasizing the importance of a clear definition of supersaturation, locally or macroscopically, since it can vary within the monolayer. In order to describe the evolving supersaturation in front of the tip of an growing domain, I applied Ivantsov[68, 69] theory. The Ivantsov solution describes purely diffusive processes in either two or three dimensions. For a more realistic approach, I modified the Ivantsov parabola according to Cantor et al.[70-72] in order to allow superimposed convective transport.

Adding up these features of erucic acid monolayers, this work aims to clarify the impact of flows with respect to domain shaping and the classification in growth regimes, described by Bruinsma et al.[19] The results may be precursors in the experimental study of non-equilibrium processes in Langmuir monolayers, including convective transport phenomena.

2. Theoretical background

2.1. Monolayers at the air-water interface

A profound theory of lipid bi- and monolayers was given by Cevc and Marsh (1987).[73] For the underlying work, I will limit myself to explain the meaning of surface pressure and surface pressure-area isotherms. I therefore refer to chapter 12.[73]

An air-water interface in the absence of a film possesses the surface free energy F_0^σ. When a lipid monolayer is spread at this interface, the free energy of the film results as:

$$F^{film} = F^\sigma - F_0^\sigma, \tag{1}$$

with F^σ, the surface free energy in the presence of the film.

By differentiating with respect to the surface area at constant temperature T and pressure π, we obtain:

$$\frac{\partial F^{film}}{\partial A} = \sigma - \sigma_0. \tag{2}$$

Here, $\sigma = (\partial F^\sigma / \partial A)_{T,V}$ and $\sigma_0 = (\partial F_0^\sigma / \partial A)_{T,V}$ are the surface tension in the presence of the film and the surface tension of pure water, respectively. From (2), the surface tension can be understood either in terms of energy or in terms of force. It is the ratio of the change in surface free energy of a liquid to the change in surface area of the liquid. It is also a force per unit length, acting within the surface. Its cause are imbalanced cohesive forces: in the liquid bulk, molecules are pulled together equally, due to cohesive forces arising from uniformly distributed neighboring molecules. However, a molecule, placed at the vicinity of the interface is surrounded by less neighboring molecules from the interfacial plane compared to the bulk side, which eventually leads to a net force, pulling the molecules inwards in the direction of the liquid bulk.

Such a difference in surface tensions σ and σ_0 cause a lateral, repulsive pressure π, acting within the surface of the monolayer. It can be defined as:

$$\pi = \sigma_0 - \sigma = -\left(\frac{\partial F^{film}}{\partial A}\right)_{T,V}. \tag{3}$$

Given the area per molecule A, the monolayer surface pressure π is usually measured with a film balance (Wilhelmy plate) on a monolayer trough. Kinetic components, like the momentum transfer during collisions between the lipid molecules, as well as repulsive interactions, like steric, electrostatic and hydration forces between the lipid molecules contribute to π.

In a Langmuir Blodgett trough, the surface pressure can be measured as a function of the monolayer area using the film balance. Being able to relate the surface pressure π to the area per molecule A, gives rise to an equation of state for the monolayer. Such a surface pressure-area isotherm ($\pi - A$-isotherm) is the equivalent of a three-dimensional van der Waals gas, adapted to two-dimensional monolayers:

$$\left(\pi + \frac{a}{A^2}\right)(A - A_e) = kT, \tag{4}$$

with A_e the excluded area per molecule ($A_e \sim 40$ Å^2), a/A^2 a correction term containing the repulsive interactions between the molecules and k the Boltzmann constant.

Neglecting the attractive cohesion forces of the hydrophobic chain-chain interactions, the measured surface pressure corresponds essentially to the repulsive interactions between the lipid molecules, caused by steric, electrostatic or hydration forces. This makes the Langmuir Blodgett trough a powerful tool, since it allows the investigation of interactions between lipid molecules over a wide range of molecular areas without condensation of the film.

2.2. Hydrodynamic classification of the erucic acid monolayers

Bruinsma, Rondelez and Levine (2001)[19] developed a theory, which explains the emergence of Marangoni flows in Langmuir monolayers. Simply put, differences in the line tension γ, driven by concentration gradients along the monolayer close to domains, generate flows.[20] Their theory is based on the idea, that hydrodynamic coupling of the monolayer with the subphase can lead to growth instabilities: Viscous stress exerted by the subphase on the monolayer, acts as an externally applied stress and must therefore be balanced by a combination of a line tension gradient and surface viscous stress.[19] Dependent on the individual contributions, they predict two growth regimes, which are characterized either by surface viscous losses or by bulk viscous losses. They showed that in both regimes Marangoni flow is possible. This chapter intends to classify my experiments according to this theory. Dependent on the compression speed v_C, I observed two different types of domain shapes: seaweed-like and dendritic shapes.[62] I was interested whether they correlate with the regimes proposed by Bruinsma et al. Therefore, I calculated scaling lengths for exemplary domains of my experiments. The next section is an overview of the underlying theory, which is important to interpret the results of chapter 5.1.

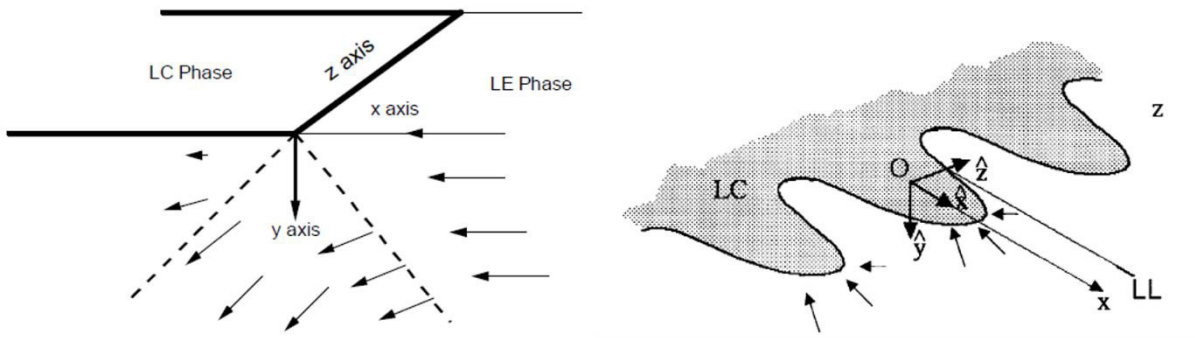

Scheme 1. Left: Marangoni flow at the LE/LC boundary. The fluid velocity is indicated by the arrows, coming from positive x-direction towards the interface at position $x = 0$. Right: A modulated LE/LC interface leads to instabilities. Reprinted from Bruinsma et al.,[19] Copyright (2001), with permission from Springer Nature.

2.2.1. The Navier-Stokes equations - a brief overview

Transport of surfactant material towards the domain boundaries can be described by applying the Navier-Stokes equations, on the assumption that subphase flow in the lipid monolayer behaves as a continuum at the scale of interest. The equations are based on the conservation of mass and momentum:

Considering a fluid element with a density ρ, moving with velocity $\vec{v}$, the conservation of mass can be described by the continuity equation:

$$\frac{d\rho}{dt} + \vec{\nabla} \cdot (\rho\vec{v}) = 0. \tag{5}$$

The conservation of momentum can be understood as Newton's second law, in terms of body forces instead of point forces:

$$\rho \frac{D\vec{v}}{Dt} = \vec{\nabla} \cdot \overleftrightarrow{\sigma} + \vec{f}. \tag{6}$$

Herby, $\frac{D\vec{v}}{Dt} = \frac{d\vec{v}}{dt} + \vec{v} \cdot \vec{\nabla}\vec{v}$ is the convective derivative, D is the diffusion coefficient of the fluid phase (LE-phase), $\overleftrightarrow{\sigma}$ the stress tensor and $\vec{f}$ comprises additional body forces. The stress tensor $\overleftrightarrow{\sigma}$ is of rank 2. Its covariant components σ_{ij} can be further decomposed as follows:

$$\sigma_{ij} = \begin{pmatrix} \sigma_{xx} & \tau_{xy} & \tau_{xz} \\ \tau_{yx} & \sigma_{yy} & \tau_{yz} \\ \tau_{zx} & \tau_{zy} & \sigma_{zz} \end{pmatrix} = -\begin{pmatrix} p_h & 0 & 0 \\ 0 & p_h & 0 \\ 0 & 0 & p_h \end{pmatrix} + \begin{pmatrix} \sigma_{xx} + p_h & \tau_{xy} & \tau_{xz} \\ \tau_{yx} & \sigma_{yy} + p_h & \tau_{yz} \\ \tau_{zx} & \tau_{zy} & \sigma_{zz} + p_h \end{pmatrix} = -p_h I + \overleftrightarrow{\tau},$$

such that $\sigma_{i=j}$ are the normal stress components, τ_{ij} the shear stress components, $p_h = 1/3 \cdot (\sigma_{xx} + \sigma_{yy} + \sigma_{zz})$ is the (negative) mean normal stress, I is the 3x3 identity matrix and $\overleftrightarrow{\tau}$ is the deviatoric stress tensor. In the case of lipid monolayers, p_h represents the hydrodynamic pressure.

This leads to the most general formulation of the Navier-Stokes equations, which read:

$$\frac{d\rho}{dt} + \vec{\nabla} \cdot (\rho\vec{v}) = 0, \tag{7a}$$

$$\rho \frac{D\vec{v}}{Dt} = -\vec{\nabla} p_h + \vec{\nabla} \cdot \overleftrightarrow{\tau} + \vec{f}. \tag{7b}$$

In order to adopt these equations to lipid monolayers, some further assumption have to be made:

I. First approximation: the subphase flow behaves like a Newtonian fluid.

This is valid, when the following applies:

1. The stress tensor is a linear function of the strain rates: $\tau_{xy} = \eta_S \frac{dv_x}{dy}$, whereby the viscosity η_S acts as a constant of proportionality between the viscous stress tensor $\overleftrightarrow{\tau}$ and the velocity gradient $\frac{dv_i}{dx_j}$.
2. The fluid is isotropic.
3. For a fluid at rest, $\vec{\nabla} \cdot \overleftrightarrow{\tau}$ must be zero, such that hydrostatic pressure results.

This allows the formulation of $\overleftrightarrow{\tau}$ in terms of surface viscosity η_S, the Kronecker delta δ_{ij} and the bulk viscosity η:

$$\tau_{ij} = \eta_S \left(\frac{\partial v_i}{\partial x_j} + \frac{\partial v_j}{\partial x_i} \right) + \delta_{ij} \eta \, \vec{\nabla} \cdot \vec{v}, \tag{8}$$

which leads to the Navier-Stokes equation in the Newtonian-form:

$$\rho \frac{D\vec{v}}{Dt} = -\vec{\nabla} p_h + \vec{\nabla} \cdot (\eta_S \cdot \left(\vec{\nabla}\vec{v} + \left(\vec{\nabla}\vec{v}\right)^{\boldsymbol{T}} \right)) + \vec{\nabla} (\eta \, \vec{\nabla} \cdot \vec{v}) + \vec{f} \tag{9}$$

II. Second approximation: the fluid is incompressible.

This requires:

1. The viscosity η_S is set a constant.
2. Second viscosity effects (bulk effects) will be ignored: η=0.
3. The mass continuity equation simplifies, since in the case of an incompressible fluid, $\rho = const$.

Then, (5) reduces to:

$$\vec{\nabla} \cdot (\vec{v}) = 0 \tag{10}$$

and

$$\vec{\nabla} \cdot \overleftrightarrow{\tau} = \vec{\nabla} \cdot (\eta_S \cdot \left(\vec{\nabla}\vec{v} + \left(\vec{\nabla}\vec{v}\right)^{\boldsymbol{T}} \right)) + \vec{\nabla} (\eta \, \vec{\nabla} \cdot \vec{v}) \tag{11}$$

simplifies to:

$$\vec{\nabla} \cdot \overleftrightarrow{\tau} = \eta_S \, \vec{\nabla}^2 \vec{v} = \eta_S \, \Delta\vec{v}. \tag{12}$$

Inserting this in the general Navier-Stokes equation, yields the formalism of an incompressible Newtonian fluid:

$$\rho \frac{D\vec{v}}{Dt} = -\vec{\nabla} p_h + \eta_S \, \Delta\vec{v} + \vec{f}. \tag{13}$$

III. Third approximation: the flows are slow.

A last simplification of (13) can be made, assuming that the timescales of flows are slow. This implies, that viscous transport dominates convective transport, such that $\vec{v} \cdot \nabla\vec{v} \approx 0$.

The Navier-Stokes equation reads now:

$$\rho \frac{D\vec{v}}{Dt} = \rho \left(\frac{d\vec{v}}{dt} + \underbrace{\vec{v} \cdot \vec{\nabla}\vec{v}}_{0} \right) = -\vec{\nabla} p_h + \eta_S \, \Delta\vec{v} + \vec{f}. \tag{14}$$

If one is only interested in the stationary solution $\left(\frac{d\vec{v}}{dt} = 0\right)$ and no externally applied forces $\vec{f}$ are considered, (14) reduces finally to the stationary Navier-Stokes equations for incompressible fluids:

$$\vec{\nabla} \cdot (\vec{v}) = 0, \tag{15a}$$

$$\eta_S \Delta\vec{v} = \vec{\nabla} p_h. \tag{15b}$$

These are the fundamental equations, which Bruinsma et al. used to explain the formation of Marangoni flows.

2.2.2. Preconditions for Marangoni flow

During domain formation, liquid condensed domains (LC-phase) grow into the liquid expanded phase (LE-phase). Characteristics are the large difference in area density between LE- and LC-phase (> 50 %, denoted in Bruinsma et al. [19], ~ 30 % measured from our erucic acid isotherms) and the low line tension at the LE/LC boundary of the domains ($\gamma \sim 0.89\ pN$). The line tension γ can be estimated by a rough calculation, using equation (26b) of Bruinsma et al.[19]:

$$\gamma = \xi_C \Delta c (c_s - c_0) \frac{d\mu}{dc}, \tag{16}$$

with:

- $c = \frac{1}{A}$ [Å^{-2}], the surface concentration in inverse units of the molecular area.
- ξ_C, a capillary length, defined by a typical mode q of the investigated monolayers: $q = \frac{2\pi}{\lambda} = \frac{1}{2\xi_C}$, and $\lambda \sim 10\ \mu m$, a characteristic length of the system, calculated from reference (62).[62]
- $c_0 = 1/27$ Å^{-2}, a reduced concentration of the LE-phase, close to the domain boundary, in accordance with $c_0 = c_\infty + \Delta c$.

- $c_\infty \sim 1/27.5\ \text{Å}^{-2}$, the concentration of the LE-phase, far away from the domain boundary, calculated from the isotherms of reference (62).[62]
- $\Delta c \sim 3 \cdot 10^{-3}\ \text{Å}^{-2}$, the supersaturation, calculated from reference (62).[62]
- $c_s \sim 1/20\ \text{Å}^{-2}$, the concentration of the LC-phase, calculated at high pressure area from the isotherms of reference (62).[62]
- $\frac{d\mu}{dc}$, the chemical potential gradient with respect to concentration. It can be estimated by using the isotherms of reference (62)[62] again:

$$\frac{d\mu}{dc} = \frac{d}{dc}\mu(\pi(A), T) = \frac{d\mu}{d\pi}\frac{d\pi}{dA}\frac{dA}{dc} = A_\infty \frac{d\pi}{dA}\frac{-1}{c^2} = \frac{-1}{c^3}\frac{d\pi}{dA}, \tag{17a}$$

$$A_\infty \frac{d\pi}{dA} = 27{,}5 \cdot \frac{2}{29{,}2-27{,}8}\frac{\text{mN}}{\text{m}} = 39.3\ \text{mN/m}, \tag{17b}$$

$$\rightarrow\ \gamma = \xi_C \Delta c (c_s - c_0)\frac{d\mu}{dc} = \frac{\lambda}{4\pi} \cdot \frac{\Delta c}{c_0} \cdot \frac{(c_s - c_0)}{c_0} \cdot A_\infty \frac{d\pi}{dA} \sim 0.89\ pN. \tag{18}$$

Another indication of the low line tension γ can be seen from Figure 1: When the monolayer compression has stopped, the domain shapes do not take on a circular shape. Instead, they dissolve and decay over time.

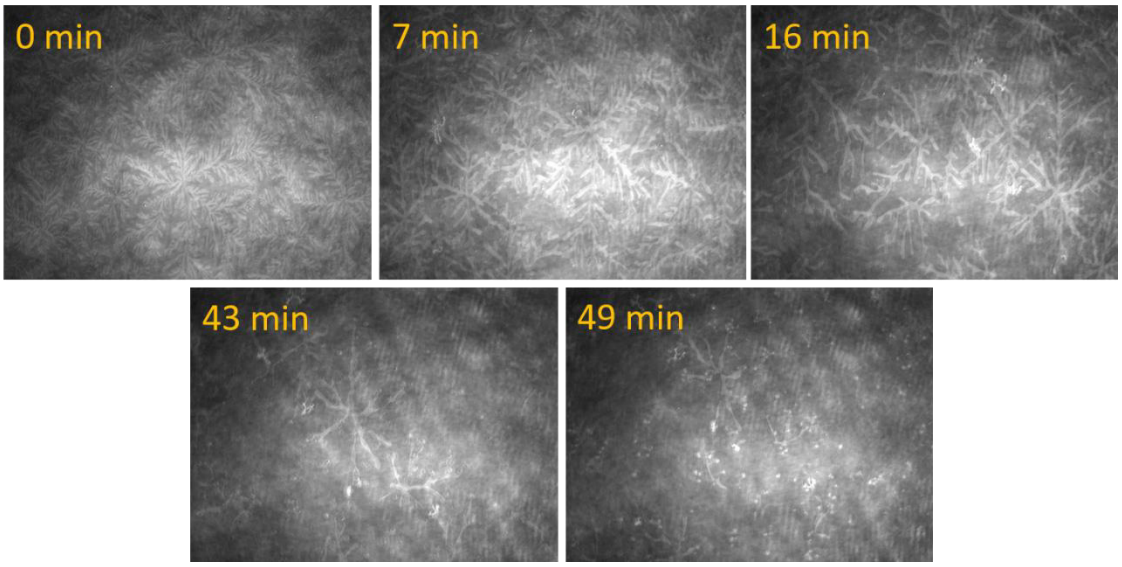

Figure 1. Time series of pictures, showing the decay of erucic acid domains, when the compression of the monolayer is stopped at low molecular area.

Since the LC-phase is rigid such that no diffusion within the monolayer takes place ($D_{LC} \sim 0$), the flows close to the domain boundaries are three-dimensional and extend into the trough (y-direction, see Scheme 1). These subphase flows exert a bulk viscous stress $\vec{\nabla} \cdot \overleftrightarrow{\tau} \sim \eta \partial_y \vec{v}(x, y = 0, z)$ on the monolayer, which has to be balanced by a combination of a line tension gradient

$$\vec{\nabla}_\perp \gamma = \left(\frac{d\gamma}{dc}\right)\vec{\nabla}_\perp c \tag{19}$$

and surface viscous stress of the form

$$\vec{\nabla}_{\perp} \cdot \overleftrightarrow{\sigma}, \tag{20}$$

with $\sigma_{ij} = \eta_s\big(\partial_i v_j(x, y = 0, z) + (i \leftrightarrow j)\big)$, the surface viscous stress tensor.

Adding the two contributions, we obtain:

$$\eta_s \left(\underbrace{{\partial_x}^2 + {\partial_z}^2}_{\Delta} \right) \vec{v}(x, y = 0, z) = \underbrace{\left|\frac{d\gamma}{dc}\right| \vec{\nabla}_{\perp} c - \eta \partial_y \vec{v}(x, y = 0, z)}_{\vec{\nabla} p_h}. \tag{21}$$

From this, two growth regimes can be deduced. The distinction can be made by introducing the Boussinesq number Bq:

$$Bq = q \cdot \zeta, \tag{22}$$

with:

- $q = 1/\lambda$, a typical Wavenumber of the investigated monolayers and λ, a mean distance between two side branches.
- $\zeta = \eta_s/\eta$, the ratio of surface to bulk viscosity.

In the first case, $\boldsymbol{Bq = q \cdot \zeta < 1}$. This implies bulk viscous losses dominate over surface viscous losses:

$$\eta \partial_y \vec{v}(x, y = 0, z) \cong \left|\frac{d\gamma}{dc}\right| \vec{\nabla}_{\perp} c \tag{23}$$

In the second case, $\boldsymbol{Bq = q \cdot \zeta > 1}$. This implies surface viscous losses dominate over bulk viscous losses:

$$\eta_s \left(\underbrace{{\partial_x}^2 + {\partial_z}^2}_{\Delta} \right) \vec{v}(x, y = 0, z) \cong \left|\frac{d\gamma}{dc}\right| \vec{\nabla}_{\perp} c \tag{24}$$

Further, Bruinsma et al.[19] introduced a cross-over length ξ to distinguish between diffusive and advective transport, defined as:

$$\xi = \frac{D\eta}{\left|\frac{d\gamma}{dc}\right| c_{\infty}}, \tag{25}$$

with D, the diffusion coefficient of the fluid phase (LE-phase) and $\left|\frac{d\gamma}{dc}\right| c_{\infty}$, the compressional modulus of the LE-phase. ξ is a cross-over length, in the sense that the flow is advective, when the flow velocity varies over length scales large compared to ξ and it is diffusive vice versa. This will be important also in chapter 5.2.2., because this length can be understood as the size of the purely diffusive layer in front of the tip of the Ivantsov parabola: Assuming that $D/v_{growth} \gg \xi$, advective transport dominates over diffusion.

2.3. The (modified) Ivantsov solution

In the second publication (article 2)[62], I introduced a supersaturation Δc in dependence of the excess lateral pressure above the LE/LC phase transition at equilibrium conditions, $\Delta\pi = \pi - \pi_\infty$, in inverse units of the molecular area, $Å^{-2}$. I showed a linear behavior between Δc and $\Delta\pi$. Since $\Delta\pi$ is obtained applying the compression modulus κ, deduced from isotherms, it is therefore averaged over the whole monolayer area. Hence, Δc is a macroscopic quantity. However, because of the continuous nucleation, anisotropy occurs within the monolayer such that, locally, the supersaturation varies. In order to specify a local supersaturation, the Ivantsov theory has been applied, which enables to calculate a normalized supersaturation Δ in front of a dendritic tip of parabolic shape. The next section is a short derivation of the Ivantsov solution, intended for readers, who are unfamiliar with the Ivantsov theory, followed by a comparison of theory with my experimental results, presented and discussed in chapter 5.2. My derivation of the Ivantsov solution refers to Langer (1980)[69] and Ihle (1996).[55] Since the Ivantsov solution is valid only for purely diffusive processes, I applied the proposed modifications of the Ivantsov parabola according to Cantor et al. (1977),[70] Gandin et al. (2003)[71] and McFadden et al. (2012)[72] in order to consider flows.

2.3.1. Derivation of the local normalized supersaturation Δ according to Ivantsov

Given an isothermal system, we can assume the temperature is constant in the whole subphase (solvent temperature $T = T_0$). Let $c_{LE,eq}$ and $c_{LC,eq}$ be the solute concentrations in the fluid (LE-phase) and the condensed phase (LC-phase), respectively, at two-phase equilibrium (standstill). At this state, $c_{LE,eq}$ exceeds $c_{LC,eq}$. In order to derive a diffusion equation for the chemical case, the chemical potentials μ and $\tilde{\mu}$ are introduced, whereby μ is the chemical potential of the solute molecules relative to that of solvent and $\tilde{\mu} = \mu - \mu_{LE,eq}(T_0)$ the difference between μ and its equilibrium value for two-phase coexistence at $T = T_0$. Assuming only small deviations from equilibrium $\mu_{LE,eq}(T_0)$, which can be therefore neglected, changes of $\tilde{\mu}$ are of the form:

$$\tilde{\mu}_{LE} = \left(\frac{\partial\mu}{\partial c}\right)\Big|_{C=C_{eq}} \partial c. \tag{26}$$

∂c are local concentration deviations. A diffusion equation in terms of the chemical potential reads now:

$$\frac{\partial\tilde{\mu}}{\partial t} = D_C \nabla^2 \tilde{\mu}, \tag{27}$$

with $D_C = M(\partial\mu/\partial c)$ the chemical diffusivity and M, the mobility of the molecules in the LE-phase. This representation of the diffusion equation has the advantage, that the only condition for local equilibrium at the interface is, that $\tilde{\mu}$ must be continuous there together with the boundary condition:

$$\tilde{\mu} = -(\gamma/\Delta c)\kappa_C, \tag{28}$$

which is the Gibbs-Thomson relation,[60, 74] suited to the domain interface, with the line tension γ, the curvature κ_C and the equilibrium density difference between LE- and LC-phase Δc. At this point, it makes sense to proceed with an universally applicable, dimensionless diffusion field u, defined as:

$$u = \frac{\tilde{\mu}}{\Delta c \cdot \left(\frac{\partial \mu}{\partial c}\right)} \tag{29a}$$

$$= \frac{T - T_0}{L/C_p}. \tag{29b}$$

It serves as a placeholder for the chemical (29a), as well as the thermal diffusion model (29b),[69] respectively, in order to treat diffusion independently of its physical origin. In the thermal case, T_0 is the temperature of the solute, L the latent heat and C_p the heat capacity. Suppose a planar interface growths with constant velocity, exactly the same amount of gained crystallization energy is either released as latent heat or rejected as excess solute molecules. Nevertheless, in both treatments it is diffusive. Then a dimensionless undercooling/ supersaturation can be defined in the form:

$$u \overset{!}{=} \Delta = 1. \tag{30}$$

In this case, Δ is exactly unity. However, at a plane domain interface the excess solute molecules (latent heat) accumulate in front of the interface, since they are not conducted away efficiently. Consequently, the interface will stop growing at a certain point. Instead, it becomes unstable against perturbations at certain wavelengths (Mullins-Sekerka Instability).[55, 75] In order to circumvent this problem, the solidification front is bent back, allowing the chemical flux (thermal flux) to diverge from the leading edge of the tip, where the excess solute concentration (the latent heat) is being generated.[69] At dendritic growth, the generated excess solute concentration (latent heat) is bigger than the crystallization energy. Therefore, locally the excess concentration is increased ($\partial c > \Delta c$) and from (29) follows $\Delta < 1$ (In the thermal case: $T > T_0$). u is introduced, such that $u = \Delta$ at a plane interface. Mathematically, the growth of the domain branches into the LE-phase can be described as a two-dimensional diffusion equation of the fluid phase (in the x/y plane), whose coordinate system moves at the interface velocity in one direction (Here: $v_{interface} = v_{y,growth}$). The diffusion of the condensed phase can be neglected, since the diffusion coefficient of the LC phase is approximately zero ($D_{C,LC} \sim 0$). A diffusion equation can be set up in the form (with $D_{C,LE} \overset{!}{=} D$):

$$\frac{\partial u}{\partial t} = D \nabla^2 u + v_{growth} \frac{\partial u}{\partial y}. \tag{31}$$

Thus, we are facing a moving boundary problem. Neglecting the time dependence, we can write (31) in the form:

$$0 = D \nabla^2 u + \frac{2}{l} \frac{\partial u}{\partial y}. \tag{32}$$

Here, we introduced l, the diffusion length, defined as:

$$l = \frac{2D}{v_{growth}}, \tag{33}$$

where $D \sim 10^{-8}$ cm²/s is the diffusion coefficient of the fluid phase[76-78] and v_{growth} the growth velocity of a main branch of the domain. For a plane interface and $\Delta = 1$, the solution of (32) is:[55, 69]

$$u(y) = \begin{cases} e^{-\frac{2y}{l}}, & y \geq 0 \; (LE - Phase) \\ 1, & y \leq 0 \; (LC - Phase) \end{cases}, \tag{34}$$

with the phase boundary at $y = 0$. For a supersaturation $\Delta < 1$, the plane interface has no stationary solution. However, an analytic steady-state solution for paraboloids exists, namely the Invantsov-solution,[68] provided line tension is ignored.[55, 69] Therefore, we transform (32) into parabolic coordinates α and β, (see Scheme 2) with:

$$\begin{aligned} \alpha &= \frac{\sqrt{x^2+y^2}+y}{R} \\ \beta &= \frac{\sqrt{x^2+y^2}-y}{R} \end{aligned} \tag{35}$$

such that it reads:

$$2\alpha \frac{\partial^2 u}{\partial \alpha^2} + (1 + 2p \cdot \alpha)\frac{\partial u}{\partial \alpha} + 2\beta \frac{\partial^2 u}{\partial \beta^2} + (1 - 2p \cdot \beta)\frac{\partial u}{\partial \beta} = 0, \tag{36}$$

with R, the tip radius of the main branches. p is the Péclet number, defined as

$$p = \frac{R}{l} = \frac{R \cdot v_{growth}}{2D}. \tag{37}$$

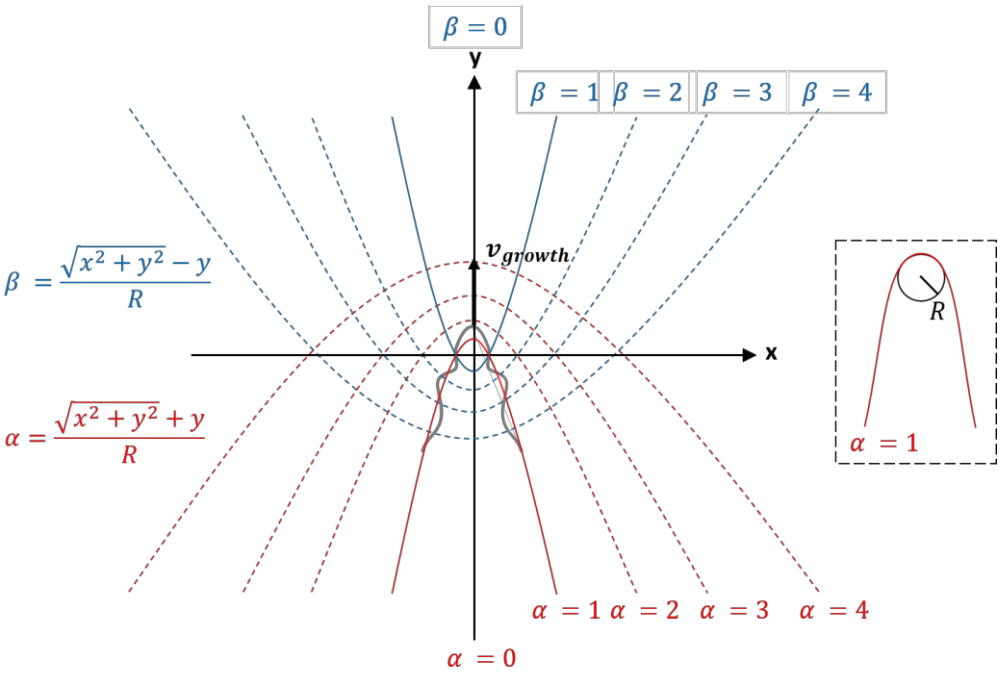

Scheme 2. Parabolic coordinates α and β, used for stability analysis (two-dimensional). For the Ivantsov solution, only the α - coordinate is used, since branch growth is considered only in positive y - direction. The definition of a tip radius is visualized in the dashed box at the right side. Adopted and modified from Langer et al.[69]

It scales with the product of tip radius R and growth velocity v_{growth}. The tip radius R of the interface parabola corresponds to the position $\alpha = 1$. u is independent of β, since locally, $u = \Delta$. A solution of (36) can be expressed in the form:

$$u(\alpha) = 2e^{p}\sqrt{p}\int_{\sqrt{p\,\alpha}}^{\infty} e^{-y^2}\,dy = e^{p}\sqrt{p\pi}\cdot erfc(\sqrt{p\alpha}). \tag{38}$$

At $\alpha = 1$, we find:

$$\Delta = e^{p}\sqrt{p\pi}\cdot erfc(\sqrt{p}), \tag{39}$$

which is known as the Ivantsov solution,[68] containing the complementary error function $erfc(x) = 1 - \mathrm{erf}(x)$. A detailed derivation of the Ivantsov solution can be found in: Ivantsov (1985),[68] Langer (1980)[69] or Ihle (1996).[55]

2.3.2. The modified Ivantsov solution (diffusion plus convection)

The results shown above are valid for purely diffusive transport. Since we assume volume flow as a requirement for dendritic growth, the Ivantsov parabola has to be adjusted. Cantor et al. (1977)[70] proposed the introduction of a stagnant parabolic boundary layer δ, which forms ahead of the dendritic tip. (See Scheme 3). Within this layer, the transport of surfactants takes place only by diffusion. Outside, there is convective transport due to flow.[70, 71] The thickness of δ depends strongly on the intensity of the fluid flow: For purely diffusive transport, δ is set to infinity ($v_{Flow} = 0$). It decreases with increasing flow. Later, Gandin et al. (2003)[71] correlated the size of δ to Sherwood number and Schmidt number by introducing correlation coefficients. They also improved the theory considering flows, which are not directed frontally towards the tip of the dendrite. McFadden et al.(2012)[72] picked up the idea and proposed a model, showing that once having measured the important parameters in front of the tip, will determine the operating conditions at the tip. They demonstrated the successful application for a binary (Al-Ge) alloy.

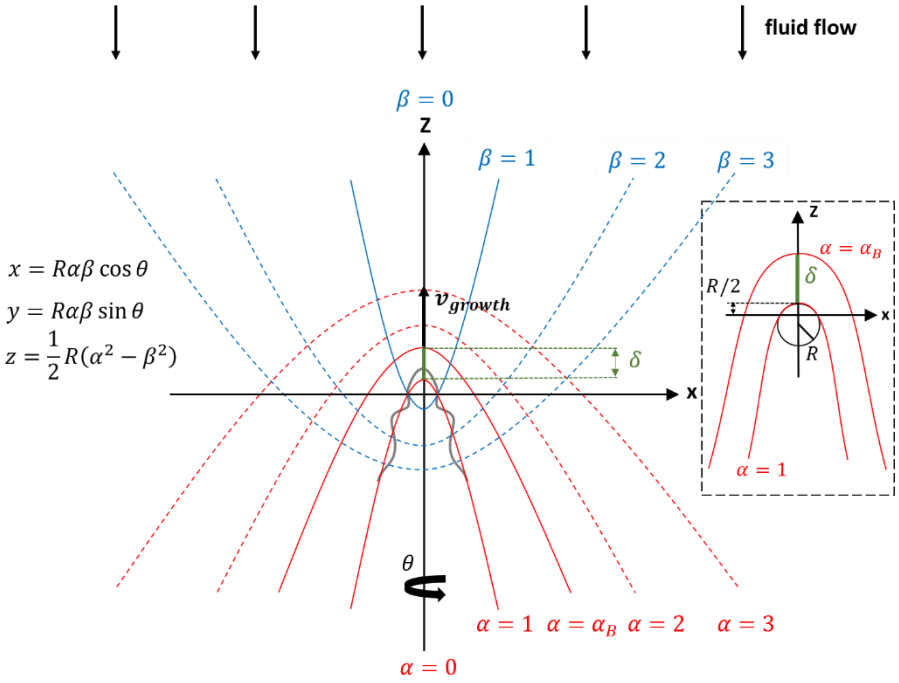

Scheme 3. Schematic diagram of the solidifying paraboloidal dendrite with paraboloidal boundary layer (three-dimensional). The flow is directed frontally towards the tip in negative z-direction. The determination of the boundary layer δ (green) is shown in the dashed box at the right side. Adopted and modified from Cantor et al.[70]

In order to calculate such a modified supersaturation Δ_{mod}, the corresponding Ivantsov parabola (or paraboloid in three dimensions) has to be found. From Scheme 3, it can be seen that this is simply a parabola, which is shifted from $\alpha = 1$ to $\alpha = \alpha_B$ (Please note the change in growth direction from y-direction shown in Scheme 2 to z-direction in Scheme 3). To calculate α_B, paraboloidal coordinates are introduced. (They correspond to $\theta \cong 0$ in the two-dimensional case):

$$x = R\alpha\beta\cos\theta \tag{40a}$$

$$y = R\alpha\beta\sin\theta \tag{40b}$$

$$z = \frac{1}{2}R(\alpha^2 - \beta^2) \tag{40c}$$

On the dendrite axis (growth in z-direction), $\beta = \theta = 0$, $\alpha = 1$, such that $z = R\alpha^2/2$. Then, the parameter α_B can be related to the boundary layer thickness δ by:

$$R/2 + \delta = R{\alpha_B}^2/2, \tag{41a}$$

or

$${\alpha_B}^2 = 1 + \frac{2\delta}{R}. \tag{41b}$$

With this geometrical construction and using the analytical solution of the diffusion field within the stagnant film, one can describe a modified, dimensionless supersaturation Δ_{mod}:

$$\Delta_{mod} = p \cdot \exp(p)\left(E_1(p) - E_1\left(p\left(1 + \frac{2\delta}{R}\right)\right)\right), \tag{42a}$$

$$\text{with } E_1(p) = \int_p^{\infty} \frac{\exp(-\tau)}{\tau}\, d\tau\,, \tag{42b}$$

the exponential integral function used in the original Ivantsov theory.

This can be expressed in terms of the error function, similarly shown in the derivation of the Ivantsov solution, shown above:

$$\Delta_{mod} = \sqrt{p} \cdot e^{p} \sqrt{\pi} \cdot \left(\underbrace{erfc\left(\sqrt{p}\right)}_{diffusive\ part} - \underbrace{erfc\left(\sqrt{p\left(1+\frac{2\delta}{R}\right)}\right)}_{convective\ correction} \right). \tag{43}$$

From (43) it can be seen, that Δ_{mod} at the outer boundary of δ is slightly weakened compared to Δ directly calculated at the tip. That means, when Δ_{mod} is translated either to a temperature field ΔT, the temperature T is lower at the tip than at the outer boundary δ and in the case of a chemical field Δc, the concentration c is higher at the tip than at the position δ, as shown in Scheme 4.

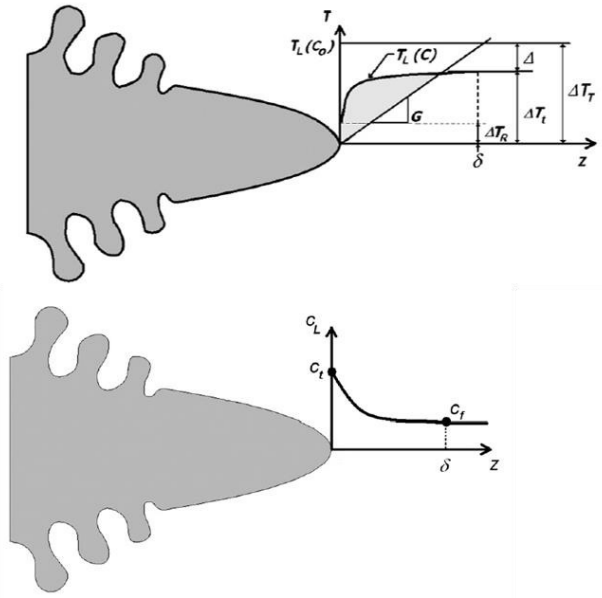

Scheme 4. Composition (top) and temperature (bottom) ahead of a three-dimensional dendrite tip. Reprinted from McFadden and Browne,[72] Copyright (2012), with permission from Elsevier.

3. Materials and Methods

3.1. Lipids and fatty acids

Phospholipids are the major structural components of biological membranes.[73] They are called amphiphilic,[3, 4] because they consist of a hydrophilic as well as a hydrophobic part: firstly, a hydrophilic head group, which is a negatively charged phosphate group connected to an additional small group, which may also be charged or polar. Secondly, a hydrophobic part, usually consisting of two nonpolar hydrocarbon chains. These lipid acyl chains vary in length and number of double bonds.

Table 1. List of the lipids used to study the oxidation of phospholipid monolayers. In each case, the position of the double bonds is marked in red.

Abbreviation	Name	Structural formula *
DMPC	1,2-dimyristoyl-sn-glycero-3-phosphocholine	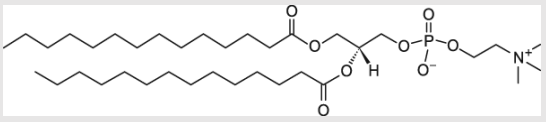
POPC	1-palmitoyl-2-oleoyl-glycero-3-phosphocholine	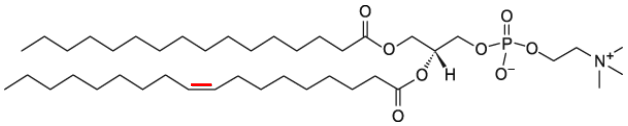
DOPC	1,2-dioleoyl-sn-glycero-3-phosphocholine	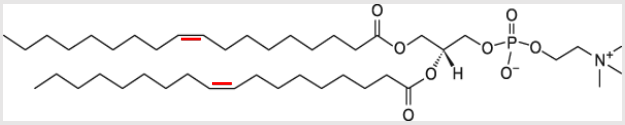
PLPC	1-palmitoyl-2-linoleoyl-sn-glycero-3-phosphocholine	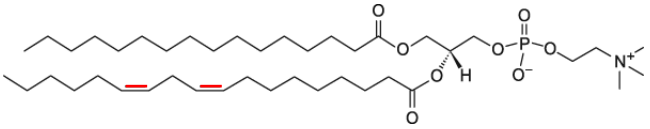
-	Erucic acid	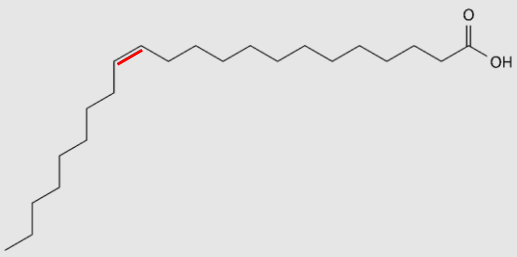

* The structural formulas are taken from: https://avantilipids.com

The latter is described as the degree of unsaturation. A fat molecule is called monounsaturated if it contains one double bond and polyunsaturated if it contains more than one double bond. The cis-double bonds cause a "kink" in the acyl chain. Due to the kink, the contact area between

the molecules is decreased. This has an impact on the melting temperature, which is lowered, compared to saturated phospolipids.[79] Further, a tight packing of the lipid molecules is hindered, allowing the membrane to maintain their fluid phase (LE-phase).[13]

Where double bonds are formed, hydrogen atoms are eliminated. Therefore, lipids consisting of unsaturated acyl chains are more prone to a ROS attack (oxidation processes). In order to study the effect of position and number of double bonds on a radical attack, phospholipids with the same head group but differing acyl chains and number of double bonds have been selected. They are listed in Table 1.

Further, we used erucic acid due to its property of forming fractal domains. It belongs to the fatty acids. Fatty acids consist of a carboxyl group, attached to one hydrocarbon chain, which is either saturated or unsaturated. In the case of erucic acid, it is monounsaturated, with the double bond adjacent to the 13th carbon atom of its acyl chain. The structural formula is shown in Table 1. Erucic acid can be gained from rapeseed.[80]

3.2. Langmuir Blodgett trough and isotherms

A suitable technique to study monolayers at the air-water interface is the Langmuir Blodgett trough.[11] A Lipid film is spread on an aqueous salt solution (subphase) in a Teflon trough. Since small contaminations, like dust particles, accumulate at the water surface, the measurement would be distorted. Therefore, the trough is shielded by a Plexiglas hood. By compressing the film, enabled by two movable barriers, the surface pressure (lateral pressure) π can be adjusted. The surface pressure π is measured by a Wilhelmy plate. A water bath, surrounding the Teflon trough, stabilizes the temperature. The subphase can be adapted to the experimental requirements by varying the pH-value, salt concentration or type of ions.

During compression, an area A vs. surface pressure π plot is recorded, which is called an isotherm. Depending on the provided molecular area, lipids exist in different phases, and may undergo a phase transition from one phase to the next. Scheme 5 illustrates a typical monolayer compression in a Langmuir Blodgett trough at three different states. Added is the corresponding isotherm.

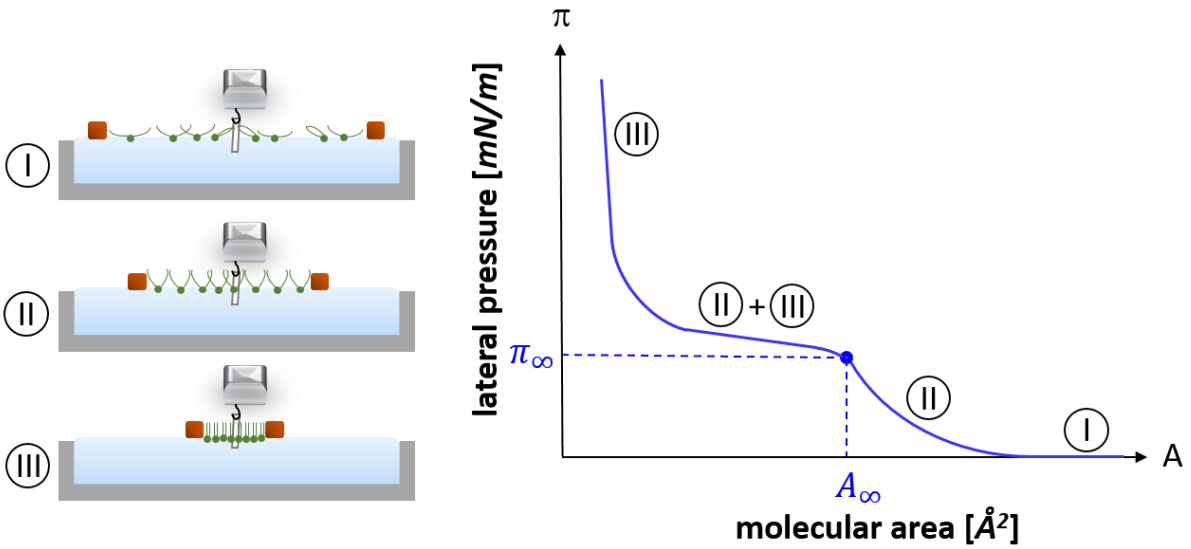

Scheme 5: Left: Depicted is a typical monolayer compression in a Langmuir Blodgett trough at three different states I-III. The surface pressure is sensed by a Wilhelmy plate (placed in the middle of the trough). Two mechanical barriers (dark red) enable the monolayer compression. Right: The corresponding isotherm is shown. Indicated is the onset of the LE/LC- phase transition pressure π_∞ at molecular area A_∞. I: Usually, the lipids (green) are spread at maximum trough area. The monolayer is in the gaseous phase, which is characterized by only weak interactions between the lipid molecules. II: For further compression of the monolayer, the barriers push the molecules closer together towards the liquid expanded phase (LE-phase) and the interactions between the molecules increase. II+III: Continuing the compression may lead to a phase transition from the LE-phase to the liquid condensed phase (LC-phase). This is the LE/LC coexistence region, where LC domains nucleate and grow. Here, the pressure increases only weakly at further decreasing monolayer area. III: Eventually, the ordering of the lipid molecules is completed and the LC-phase is reached. The surface pressure increases now steeply due to the low compressibility of the ordered LC-phase.

3.3. Brewster angle microscopy

Brewster angle microscopy (BAM) is a microscopy technique, enabling the observation of ultrathin films (~ 1.5 nm) at the air-water interface. The BAM was introduced at the beginning of the 1990s (Hénon and Meunier (1991),[21, 81] Hönig and Möbius (1991)[23]) and was principally developed to study Langmuir films. The mechanism is shown in Scheme 6. Hereby, two mediums or two phases of the same medium, respectively are in contact.[22] They differ in the dielectric constants n_1 and n_2. When light is emitted towards such a surface, it will be partly transmitted and partly reflected. With regard to the reflectivity of light from a surface, its angle of incidence and its polarization are of crucial importance:[21] using light, which is polarized in the plane of incidence (p-polarized), one can find an angle of incidence, for which the reflectivity vanishes for a Fresnel interface (an ideal interface between medium 1 and medium 2, at which the refractive indices $n_1$and n_2 abruptly change). This is called the Brewster angle θ_B. The phenomenon of blocking light propagation is a consequence of light-matter interaction: The electric field of the incident light wave induce dipole moments in the second medium n_2. At the Brewster angle θ_B, those dipole moments point exactly in the direction of the reflection. Since the dipoles cannot radiate in the direction of propagation of the reflected wave, the reflectivity vanishes.[21] θ_B can be calculated using the Snell's Law, on the condition that the angle of reflection θ_1 (or incidence) and the angle of refraction θ_2 sum up to 90°:

$$\tan \theta_B = \frac{n_2}{n_1}. \tag{44}$$

An air-water interface ($n_1 = 1$, $n_2 = 1.33$) results in a Brewster angle of $\theta_B \approx 53°$.

Since real interfaces have continuous transitions, the refractive index will not change abruptly from one medium to the next. Therefore, a perfect extinction of the p-polarized light is practically not possible. However, at a clean water surface, the reflectivity is still very low (1.2×10^{-8})[21]. Spreading a thin lipid film at the water surface will now change reflectivity strongly, since its refractive index differs from water or air. This is what the technique takes advantage of: the lateral morphology of the monolayer can be mapped at high contrast by the use of the reflected light. The method is especially powerful, when combined with a Langmuir trough. If the properties of the interface change, which happens while compressing the monolayer, the intensity of the reflection increases. Then, it can be used to relate the BAM images with characteristic phase transition points in a Langmuir isotherm. A *nanofilm_ultrabam Brewster Angle Microscope* (Accurion, Göttingen, Germany) was used to record real-time grayscale movies of the dendrite growth at 20 frames per second. Due to the implemented Scheimpflug optics, it is possible to generate an overall focused image. Each frame corresponds to an overall focused image of a surface area of about $0.24\ mm^2$ (1360 pixels × 1024 pixels, spatial resolution of $2\ \mu m$).

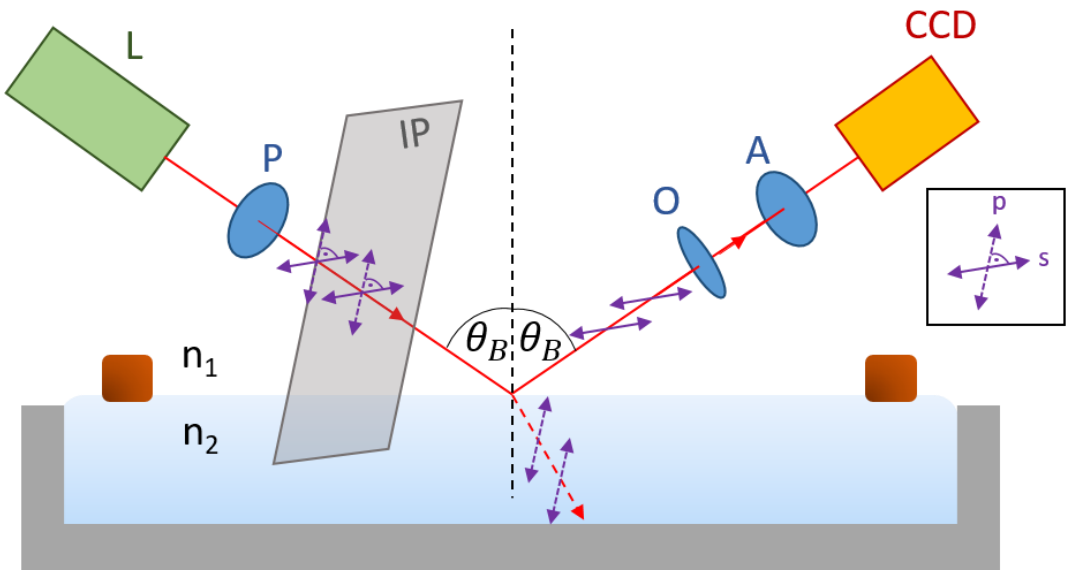

Scheme 6. Shown is the beam path of a Brewster angle microscope, which is positioned above the center of a Langmuir Blodgett trough. Monochromatic (red) light ($P = 50\ mW, \lambda_L = 658\ nm$) from a laser source (L) passes through a polarizer (P), enabling to adjust the polarization plane. The polarized light (p: parallel to the incident plane (IP), s: perpendicular to the incident plane (IP)) is then directed towards the air-water interface. Here, it will be partially refracted and partially reflected. According to Brewster's law, the p-polarized fraction of the light beam is suppressed in the reflected beam. Only the s-polarized fraction passes through an objective (O), which creates a real, enlarged image of the water surface on the CCD detector (CCD). An analyzer (A) allows to increase the contrast by tuning the polarization plane. The CCD detector serves as an input for recording videos.

There are two key benefits of the BAM technology compared to a fluorescence microscope: In fluorescence microscopy experiments, the contrast in the pictures results from different densities of the fluorescent molecules in the different phases. In dense and well-ordered phases (LC-phase) the fluorescent molecules are almost squeezed out and hence poorly visible. Secondly, the dye acts as a surface-active impurity which itself will modify the systems behavior.

4. Conclusions

4.1. Article 1: Oxidation of Unsaturated Phospholipids: A Monolayer Study

The oxidation of phospholipid monolayers was studied at the air-water interface. Due to its high biological relevance, phosphatidylcholines with identical head groups but different saturated and unsaturated acyl chains were investigated. One aim of this work was to investigate how the number of double bonds and their location on one or two acyl chains influences lipid peroxidation.

Riske et al.[48] proposed a model of the structural changes on the molecular level by oxidation for vesicles. They observed that mainly the acyl chains are affected by ROS. In a first step, hydrogen is abstracted from a carbon atom adjacent to a double bond in the unsaturated acyl chain from a lipid. This is the preferred position for a radical attack, because the carbon–hydrogen bond is weakened by the neighboring, electron-rich double bond. The eventually added, more hydrophilic –OOH group is drawn to the hydrophilic head group of the lipid. This leads to a kink in the acyl chain, which increases the molecular area A by δA. The model of the area increase in vesicles could be adopted to monolayers: The relative molecular area increase $\delta A/A$ between oxidized and non-oxidized monolayer along the isotherm served as a measure for oxidation.

A highly concentrated hydrogen peroxide-enriched PBS buffer solution (~1 M H_2O_2) was used as a precursor for higher reactive radicals, namely the hydroxyl radical ·OH, leading to concentrations of $c_{\cdot OH}$ ~ 50 nM. The lipids were in the gaseous phase (~200 Å²/ molecule) at their first contact with the reactive oxygen species (ROS). Once generated, the hydroxyl radicals in the subphase of the trough were found to reach the lipid monolayer by diffusion from the subphase. Provided there is enough space between the lipid molecules of the monolayer, the ROS have easy access not only to the head group but also to the acyl chains. This is a monolayer advantage, compared to vesicles, were the lateral pressure is high ($30\ mN/m < \pi < 35\ mN/m$).[82] After a defined waiting time (5-45 Min), the monolayer was compressed and the isotherm was recorded.

4 different phospholipids were investigated: DMPC with no double bonds showed the weakest relative area increase, and PLPC with two double bonds on one acyl chain showed the strongest. Between those, lied DOPC, with one double bond at each acyl chain and POPC, with one saturated acyl chain and one monounsaturated acyl chain, respectively ($\delta A/A$ is 4% for DMPC, 11% for DOPC, 12% for POPC, and 14% for PLPC). The similar relative area increase of DOPC and POPC indicated that the second double bond on the other acyl tail of DOPC was not accessible for the ROS attack in the monolayer. These results suggest that the area increase grows with the number of double bonds in one acyl chain.

Further, as a measure of the lateral interaction between the lipid molecules, not only the isotherm but also the bulk modulus κ was considered, which is the inverse of the area compressibility modulus.[9] κ was calculated from isotherm data of POPC. It increased linearly on decrease of the molecular area. I conclude that POPC was in the LE phase before and after exposure to ROS; the lateral interaction between the lipid molecules remained basically unchanged.

The calculated area increase $\delta A/A$ was slightly lower than found for oxidized lipids in vesicles (~15 – 20%), since the reaction kinetic was slow and saturation was not yet reached. The reaction kinetic could be estimated by a $\sqrt{t}$ dependence of the number surface density $N_{surface}$, which is a measure of the number of ROS sticking on the monolayer. From this, the initial ROS concentration c_0 could be extrapolated (c_0 ~ 50 nM).
The temperature behavior of the relative area increase should be in agreement with the Stokes−Einstein diffusion coefficient. Therefore, a normalized diffusion coefficient according to the Stokes−Einstein equation has been calculated and applied to the temperature dependence of the relative area increase. The result was consistent.
I concluded that a pronounced area increase was only observed when the acyl chains were unsaturated. The largest effect was observed with two double bonds in one acyl chain. The relative area increase then was larger, which was attributed to a faster reaction rate. The results showed that lipid monolayers are suitable model systems for the study of the interaction between reactive oxygen species and membranes, because they provide insights into the molecular mechanisms and the time scale of lipid interaction with ROS.

4.2. Article 2: Seaweed and Dendritic Growth in Unsaturated Fatty Acid Monolayers

The lateral movement in lipid membranes depends on the diffusion constant of the membrane constituents within the membrane. However, when the flux of the subphase is high, the convective flow beneath the membrane also influences lipid movement and therefore has impact on domain growth. Supersaturation induces domain growth, which, depending on the experimental conditions, forms fractals, which are either seaweed-like or dendritic. I used uncharged monolayers of erucic acid to describe the different growth instability classes. Compared to other (phospho-)lipids, their line tension is lower and their nucleation phase is continuous. This led to domain shapes deviating from bean-/circular shaped boundaries. In the LE/LC coexistence region, the lateral pressure and, thus, the supersaturation increased. For these reasons, the selected system was especially suitable to investigate transport mechanisms influencing the domain formation. Theoretically, seaweed growth is predicted when lipid diffusion dominates, whereas dendritic growth is expected when adjunctive diffusion contributes to the lipid movement.[19]

Lipid monolayers of an unsaturated fatty acid at the water–air interface were investigated with isotherms and Brewster angle microscopy (BAM). In our approach, the high supersaturation needed for dendritic growth was induced by a fast, constant compression speed of the monolayer. Compared to pressure jumps, often used in the past, our approach had the advantage of having well-defined hydrodynamic conditions. I studied the influence of the compression speeds v_C on the isotherms and the formation of domains in the LE/LC coexistence region. Dependent on the compression speed of the monolayer, I observed two growth regimes: At low compression speed, seaweed-like domains, at high compression speeds, the domains exhibited dendritic shape.

For low compression speed, an equilibrium isotherm was recorded. The phase transition pressure was found to be $\pi_\infty = 12.4\, mN/m$. With the increase in the compression speed, the LE/LC phase transition occured later, i.e., the lateral pressure π_t is increased while the

molecular area A_t is decreased. The coexistence region was not flat, indicating a decreasing molecular area of the LE phase during compression. I observed that domain nucleation occurred at lateral pressures slightly above LE/LC phase transition π_∞ and continued within the coexistence region. The excess lateral pressure $\Delta\pi = \pi - \pi_\infty$ was found to be a convenient parameter since it is proportional to the supersaturation Δc at low values of $\Delta\pi$. This macroscopic supersaturation concentration Δc in units of $\mathring{A}^{-2}$ was calculated from the area compressibility κ of the LE phase.

The dimension of the domains was fractal, and they grew with a constant growth velocity. Increasing the compression speed of the monolayer induced a transition from seaweed growth to dendritic growth.

For a more quantitatively characterization of the two growth regimes, I introduced parameters such as tip radius, branch length, side branch separation and fractal dimension: Seaweed domains had broad tips and wide and variable side branch spacing. Only few domains nucleated. The diameter of the domain reached a few 100 μm. In contrast, dendritic domains had a higher fractal dimension, narrower tips, and small, well-defined side branch spacing. They grew faster and the number of nuclides was higher. On further monolayer compression, the domains started to interact with each other, limiting their final size. The domains' growth velocity increased and the tip radius decreased with increasing supersaturation Δc in the LE/LC coexistence region. The fractal dimension D_F of the domains had been calculated for complete domain formation after nucleation. Therefore, a Matlab boxcount algorithm was adopted to calculate D_F for complete BAM movies. A considerably smaller fractal dimension of $D_F \sim 1.6$ has been calculated for seaweed-like domains than for dendrites, where I found values of around $D_F \sim 1.8 - 1.9$. The fractal dimension stayed constant after around 20 seconds within an error.

I further compared the domains of monolayers compressed with the same compression velocity, but which nucleated at different degrees of supersaturation within the LE/LC coexistence regime. With increasing supersaturation (excess lateral pressure), the radii of the tips of the main branches decreased while their growth speed increased. The former feature has been predicted theoretically, the latter is new (to the best of our knowledge). In addition, the main branches of dendrites had a growth speed of about a factor of two greater than the main branches of seaweed domains. The faster growth speed is seen as evidence of adjunctive flow.

4.3. Article 3: Influence of Surface Flows on the Shape of Fractal Domains

The established system, I presented in article 2 showed a continuous nucleation in the LE/LC coexistence regime. It led to an anisotropy in the fluid phase, characterized by the occurrence of surface flows. Article 3 comprises my observations of the consequences of this anisotropy in terms of domain shaping. Furthermore, the arising surface flows allowed me to draw conclusions regarding dynamic processes within the lung:

The lung is a living system in contact with its surroundings. Air is inhaled and exhaled. Thus, the air-alveolus interface is subject to air flows during breathing. The alveolus surface is covered with a surfactant monolayer. Erucic acid monolayers at the air-water interface were compressed fast to model this highly dynamic exhalation process. The selected system exhibited fractal liquid-condensed (LC) domains due to its low line tension. Deformations could easily be resolved. Thereby, surface flows were induced, whose impact on domain shape was optically observed with Brewster angle microscopy (BAM). The influence of these drifts on the domain shape was investigated in terms of the magnitude, direction, and duration of the surface flow. Contrast-enhanced BAM pictures at different recording times were analyzed with 2-dimensional Fast Fourier transform spectra (FFT) and directionality histograms. The direction of this surface flow was arbitrary and changed from monolayer to monolayer. Only a weak correlation between compression speed and drift velocity was found.

The domains grew and additionally moved within the field of view. The drift velocities v_D of the domains were calculated by dividing the displacement of the domain center by the time increment. Then, the 2-dimensional Fourier transform (FFT) spectrum was calculated. The FFTs showed point symmetry. Low flows led to a six-fold symmetry. At higher drift velocity v_D, the FFT exhibited incisions. With increasing drift velocity v_D, the calculated FFT spectra showed a two-fold symmetry and the incisions along the symmetry axis got deeper and wider, leading to a dumbbell shaped FFT spectrum. I concluded that the domains grew preferentially in the direction parallel to the incision.

Directionality histograms were used to investigate the correlation between the direction of the symmetry axis and the flow direction; their minima correlated with the flow direction, provided the drift velocity was large (above 10 $\mu m/s$). The depth and width of the minima was a measure of the reduced domain growth parallel to the drift direction. They depended on the absolute value of the drift velocity.

Perpendicular to the drift direction, domain growth was preferred as the FFT showed. Furthermore, downstream growth was preferred for short drift times. However, downstream and upstream growth were similar for long drift times (40 s to 80 s).

Dendrites were formed when the compression speed v_C was high, while seaweed domains were formed when v_C was small. Since the monolayer compression took longer with low compression speeds, most dendrites were subject to short drift durations, however there were some exceptions. This led to the conclusion, that the domain distortion occurred the same way, independent if a dendrite or a seaweed domain was considered.

I conclude further, that the hydrodynamic flows in the subphase and surface flows are superimposed. Both act on lipids in the LE phase. Hydrodynamic flows act on μm scale and influence the domain morphology (distance between side branches and tip radius) and the growth speed of the main branches. Hydrodynamic flows are independent of surface flows. Surface flows act on the mm to cm scale, cause an anisotropic flow in the LE phase surrounding the domain, and thus affect the overall domain shape. At the air-alveolus interface, fast compression occurs during exhaling or coughing. The presented experiments suggest that the domains shapes are affected by the exhalation speed, but the processes at the μm-level and below (lipid aggregation at the domain edge, local multilayer formation) are not affected.

5. Further investigations and outlook

5.1. Comparison of hydrodynamic theory with results

5.1.1. Boussinesq numbers

Applying equation (22), I calculated Bq, listed in Table 2 below:

Table 2. Intermediate values and values of Bq, calculated from exemplary seaweed and dendritic domains.

Quantity	Seaweed	Dendritic
η_s [N·s/m] *	$2.0 \cdot 10^{-10}$	$2.0 \cdot 10^{-10}$
η [N·s/m²] (H_20 at 10 °C) **	$1305.9 \cdot 10^{-6}$	$1305.9 \cdot 10^{-6}$
$\zeta = \eta_s/\eta$	$1.53 \cdot 10^{-7}$	$1.53 \cdot 10^{-7}$
λ [m]	$12.5 \cdot 10^{-6}$	$5.2 \cdot 10^{-6}$
$q = 2\pi/\lambda$ [m^{-1}]	$0.5 \cdot 10^{6}$	$1.2 \cdot 10^{6}$
$\boldsymbol{Bq = q \cdot \zeta}$	$\mathbf{0.08}$	$\mathbf{0.19}$

* Wilke et al.[83]

** Handbook of Chemistry and Physics, 95th edition, chapter 6, page 2[84]

Since the values of Bq are smaller than one, bulk viscous dissipation is the dominating effect in the seaweed, as well as the dendritic regime. Dendritic domains showed a doubling of Bq, compared to seaweed domains. A comparison with Gutierrez, Diaz-Leines and Castillo (2010),[20] who obtained values of Bq*~0.1-0.5*, showed that our results are of the same order, reinforcing our estimate.

5.1.2. Cross-over length between diffusive and advective transport

I calculated the cross-over length ξ as follows:

$$\xi = \frac{D\eta}{\left|\frac{d\gamma}{dc}\right|c_\infty} = \frac{D\eta}{\left|\frac{d\pi}{dc}\right|c_\infty} = \frac{D\eta}{\left|\frac{d\pi}{dA}\right|A_\infty}, \tag{45}$$

whereby $\kappa = \left|\frac{d\pi}{dA}\right| A_\infty$ is the compressibility modulus, deduced from isotherms of reference (62):[62]

$$\kappa = A_\infty \frac{d\pi}{dA} = 27{,}5 \cdot \frac{2}{29{,}2-27{,}8} \frac{mN}{m} = 39.3 \frac{mN}{m}. \tag{46}$$

$D \approx 1 \cdot 10^{-12} \frac{\mathrm{m}^2}{\mathrm{s}}$ is the diffusion coefficient[76-78] of lipids in the fluid phase and η again the bulk viscosity of water.[84] With that, I found $\xi \sim 3.3 \cdot 10^{-14}\, m = 3.3 \cdot 10^{-8}\, \mu m$, which is indeed a little bit low: Bruinsma et al. proposed ξ to be a molecular length scale in the order of ~ 10 Å. A reason for the discrepancy in theoretically predicted ξ and calculated ones from experimental data could be the uncertainty of the diffusion coefficient D. I was not able to find

accurate lateral diffusion coefficients for erucic acid molecules in the fluid phase at 10 °C. Therefore, the real D could be slightly higher, resulting in a larger cross-over length ξ.

5.2. Comparison of Ivantsov theory with results

5.2.1. Classification of experimental results according to the Péclet numbers

I calculated the normalized supersaturation Δ from experimentally obtained values, applying equation (39). Considered for the calculation were only main branches of the growing domains. The measuring procedure of the individual quantities is described in the second publication (article 2)[62] in detail. Table 3 is a compilation of the results for three different compression speeds.

Table 3: Measured paramaters and the resulting values of the Péclet number p according to equation (37) and the local, normalized supersaturation Δ according to equation (39), deduced from exemplary seaweed (s) and dendritic (d) domains at different compression speeds v_C.

v_C [Å²/(molecule · min)]	v_{growth} [µm/s]	R [µm]	$l = 2D/v_{growth}$ [µm]	$p = R/l$	Δ
1.2 (s)	3.05	2.46	0.66	3.59	**0.90**
1.2 (s)	2.98	2.35	0.67	3.66	**0.90**
1.2 (s)	2.09	2.72	0.96	2.85	**0.88**
1.2 (s)	2.29	2.64	0.87	3.03	**0.88**
2.3 (d)	10.18	1.23	0.20	6.23	**0.93**
2.3 (d)	13.85	0.96	0.14	6.67	**0.94**
2.3 (d)	13.13	1.16	0.15	7.60	**0.94**
2.3 (d)	14.79	1.08	0.14	7.95	**0.95**
2.3 (d)	24.75	0.91	0.08	11.28	**0.96**
2.5 (d)	14.34	1.36	0.14	9.74	**0.96**
2.5 (d)	11.28	1.12	0.18	6.31	**0.93**
2.5 (d)	15.75	0.96	0.13	7.60	**0.94**
2.5 (d)	16.86	0.96	0.12	8.12	**0.95**

I obtained values of $0.88 \leq \Delta \leq 0.90$ for the seaweed regime and $0.93 \leq \Delta \leq 0.96$ for the dendritic regime. Figure 2 shows the dependency of the Ivantsov solution Δ on the Péclet number. Indeed, the seaweed domains belong to lower Péclet numbers ($p < 5$) than the dendrites ($p > 6$).

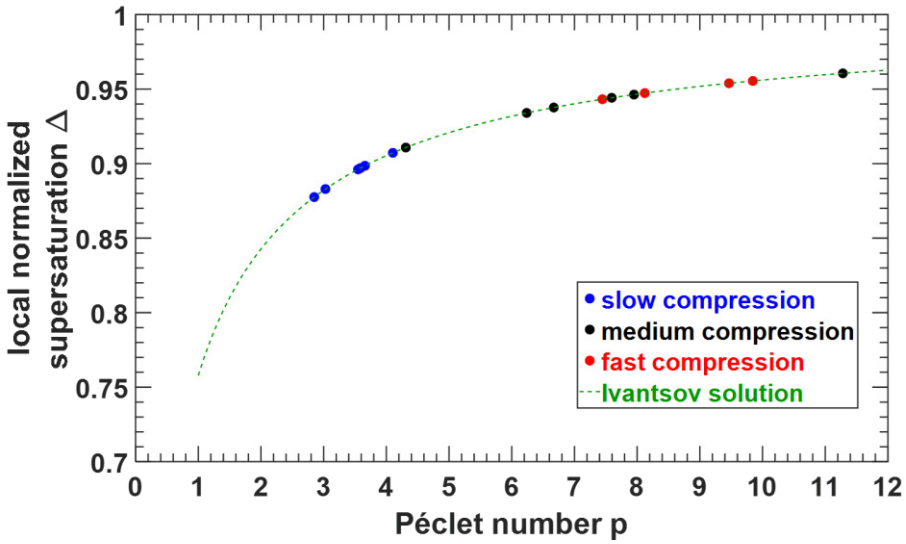

Figure 2. The local, normalized supersaturation Δ, in dependence on the Péclet number p. The dashed green line shows the general Ivantsov solution Δ, calculated using equation (39). The points indicate the experimental results listed in Table 3 for the compression speeds, specified in the Table.

5.2.2. Determination of the diffusion zone

The determination of δ is difficult, since neither it can be measured directly nor calculated from measured quantities of the system. A first ansatz, proposed by Bruinsma et al.,[19] was shown in chapter 2.2., equation (25): Assuming that $\xi \overset{!}{=} \delta \ll D/v_{growth}$, advective transport dominates over diffusion. Using their approach, I found a thickness of $\delta = \xi \sim 3.3 \cdot 10^{-14}\, m = 3.3 \cdot 10^{-8}\, \mu m$. This value is orders of magnitudes lower than the calculated diffusion lengths ($l \sim 0.1\, \mu m - 1\, \mu m$, see Table 3) for both, seaweed and dendritic growth and an underestimation of a real boundary layer. Further, it does not consider flow, since ξ is a fixed value. The boundary layer however, should be flexible, dependent on the intensity of the flow.

Cantor et al.[70] proposed such a variable diffusion zone δ, dependent on the Reynolds number $Re = p/Sc$, which reads:

$$\delta = R \cdot Re^{-1/2}. \tag{47}$$

It is composed of $Sc = \nu/D$, the Schmidt number, containing ν, the kinematic viscosity of the flowing medium ($\nu_{H_2O}[10°C]$: $1.3063 \cdot 10^{-6}\, m^2/s$).[84]

Figure 3 graphically illustrates the calculated values of δ (dots in the plot), when equation (47) is applied to the Péclet numbers listed in Table 3. The curve progression is a best fit to the calculated values. It decays with $\sim p^{-1.4}$. Data from slow compressed monolayers (seaweed domains) correspond to small Péclet numbers and lead to a thicker diffusion layer, whereas the fast compressed monolayer (dendritic domains) shows bigger Péclet numbers, which reduced δ, as predicted from theory. Therefore, the curve progression shows exactly the behavior desired by the theory. Regarding the absolute values of δ, the scope lies between

300 μm – 1800 μm. Comparing this with the size of a fully-grown domain, δ would be of the same order, which is therefore a bit overestimated for a diffusion zone.

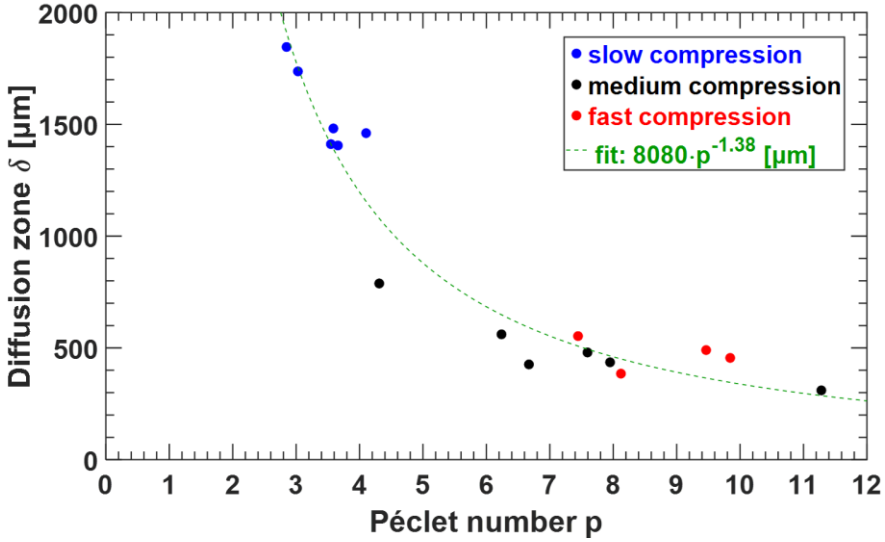

Figure 3. The dependence of the thickness of the diffusion zone δ on the Péclet number p. The points are calculations of the values, shown in Table 3 by applying equation (47). The green dashed line shows the best fit to the experimental data.

The progression of δ in dependence of p can be further improved, when equation (47) is modified to satisfy chemical diffusion:[70] In this specific case, δ is multiplied by the Schmidt number as follows:

$$\delta_C = \delta \cdot 2 \cdot Sc^{-1/3} = 2R \cdot Sc^{-1/3} \cdot Re^{-1/2}. \tag{48}$$

δ_C corresponds now to a boundary layer, applied to chemical diffusion. Figure 4 shows the dependence of the diffusion zone δ_C on the Péclet number p. Again, δ_C decreases with increasing amount of flow with $\sim p^{-1.4}$, but the absolute values are around two orders of magnitudes lower now: For seaweed domains between $25\,\mu m \leq \delta_C \leq 34\,\mu m$ and for dendritic domains $6\,\mu m \leq \delta_C \leq 14\,\mu m$.

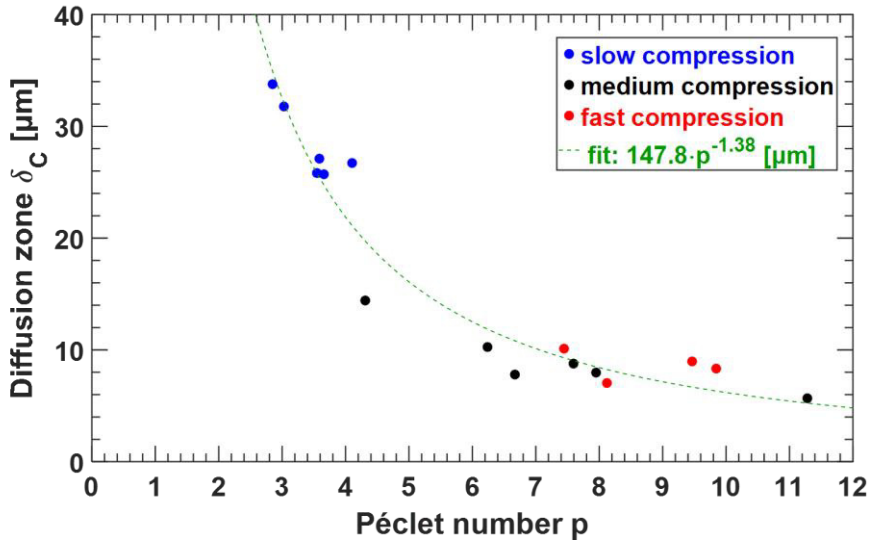

Figure 4. The dependence of the diffusion zone δ_C on the Péclet number p. The dots are calculations of the values, shown in Table 3 by applying equation (48). The green dashed line shows the best fit to the experimental data.

The corrective term, $\Delta_{convective} = erfc\left(\sqrt{p\left(1+\frac{2\delta}{R}\right)}\right)$, or $\Delta_{convective} = erfc\left(\sqrt{p\left(1+\frac{2\delta_C}{R}\right)}\right)$, respectively, could now be calculated by inserting the corresponding numbers of p, δ (or δ_C) and R in the complementary error function. However, for all numbers, the corrective term is almost zero, because the complementary error function $erfc(\varphi)$ converges to zero very quickly (rounded to two decimal places):

- $erfc(0.1) = 0.89$
- $erfc(0.5) = 0.48$
- $erfc(1) = 0.16$
- $erfc(5) = 1.54 \cdot 10^{-12}$
- $erfc(10) = 2.09 \cdot 10^{-45}$

From all the values shown in Figure 3 and Figure 4, the smallest argument $\varphi = \sqrt{p\left(1+\frac{2\delta_C}{R}\right)} \sim 8.57$, corresponding to $erfc(\varphi) = 8.35 \cdot 10^{-34}$, which is close to zero and therefore negligible in equation (43). A correction in this sense makes therefore only sense for diffusion layers in the range of Å. Based on the present theory, I was not able to give a more accurate estimation of δ. Therefore, Δ, depicted in Figure 1 is the most accurate result of a local, normalized supersaturation I was able to give. Nevertheless, the progression of the diffusion zone, shown in Figure 3 and Figure 4 is plausible.

5.3. The big picture

A key question this thesis aimed to answer was how the two growth regimes, namely the seaweed regime and the dendritic regime differ. I reported distinctive features of the two observed growth morphologies, depending on the compression speed v_C of the monolayer: For slow compression speeds, I observed seaweed-like domains, whereas at fast compression speed I saw dendritic domains. Compared to seaweed domains, dendritic domains exhibit a higher fractal dimension D_F, higher growth velocities of the main branches v_{growth}, smaller tip radii R, a more pronounced side branch-separation λ. Both showed a continuous domain nucleation during monolayer compression. These are all descriptive features. At this point it would be interesting to know, whether there exists a decisive criterion for the formation of either seaweed or dendritic domains. It is evident, that the supersaturation, induced by high compression speeds plays an important in that respect. I could distinguish between two differently defined supersaturations:

Firstly the macroscopic, mean supersaturation Δc, which is assumed to be constant over the whole surface of the Langmuir Blodgett trough and expressed in units of the inverse of the molecular area $Å^{-2}$. It has its origin in the high compression speed v_C of the monolayer, which leads to an increased molecular concentration $c_\infty + \Delta c$ in the LE-phase. It is calculated from isotherm data.[62] The averaged supersaturation increases linearly with increasing lateral excess pressure $\Delta c = \alpha \Delta \pi$ with α derived from the compressibility at the onset of the phase transition $\alpha = \frac{dc}{d\pi} = \frac{1}{A_\infty^2}\frac{dA}{d\pi}$ and $\Delta \pi = \pi - \pi_\infty$, where π is the actual lateral pressure and π_∞ is the equilibrium phase transition pressure.

Secondly, I defined a local normalized supersaturation Δ, in the vicinity of the diffusion zone of the growing domains. It could be determined by measuring growth velocities v_{growth}, tip radii R, and diffusion lengths l of the analyzed domains, which are derived from microscopic observations.

Since both supersaturations are available now, it is obvious to connect the two approaches. In order to get some insight in the growth behavior, the link was the lateral excess pressure $\Delta\pi$. This is shown in Figure 5 below.

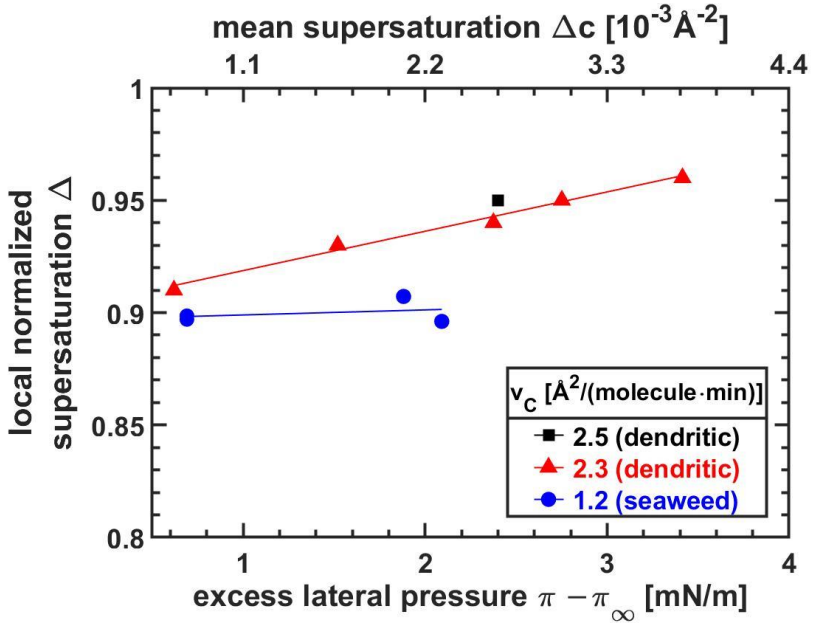

Figure 5. The dependency of the local supersaturation Δ on the lateral excess pressure and mean supersaturation of seaweed domains (blue) and dendritic domains (red and black). Circles, triangles and squares are calculated values, applying equation (39). The lines are linear fits with slope 0.0022 m/mN (blue) and 0.0175 m/mN (red), respectively.

Figure 5 clearly shows a differing behavior between the two growth morphologies. The local normalized supersaturation Δ of seaweed growth seems to be quite stable for a further increase of the lateral excess pressure $\Delta\pi$. Here, the compression speed of the monolayer is simply too slow in order to induce a locally increased supersaturation on further compression. Thermodynamically speaking, the LE-phase and the LC-phase stay in equilibrium. The situation is different for the dendritic morphology. Now, the local normalized supersaturation reacts quite sensitively on further compression: An increase of $\Delta\pi = 2.8\ mN/m$ leads to a rise in Δ of roughly 5.5 %. This is clearly an indication that we are in a non-equilibrium regime, which is caused by a strong coupling to the subphase. It therefore reinforces the thesis of Marangoni flows,[19, 62] leading to a dendritic shape of the domains.

To my knowledge, my colleagues and me were one of the first who did such a profound analysis of non-equilibrium Langmuir monolayers. One key finding is therefore, that a qualitative characterization of such a system is possible, however when it comes to quantification, existing theory fails. A reason is the lack of reliable quantities, such as diffusion coefficients of very specific lipids at specific temperatures. The same is true for surface viscosities. Therefore, there was always an uncertainty in our calculations. Another reason is that such two-dimensional systems differ in many ways from their three-dimensional counterparts, which are relatively well explored - theoretically, as well as experimentally. (For example, dendritic growth in alloys).

In this sense, I hope to have contributed to the pioneering work of understanding non-linear growth phenomena in Langmuir monolayers with the present thesis.

6. Summary

Langmuir Blodgett troughs have been used for thirteen decades.[9, 11, 85, 86] It is probably the most known and proven method to investigate lipid monolayers, based on a very simple technique: lipid monolayers are laterally compressed with mechanical barriers. Especially, when combined with a microscope, it makes it a powerful tool. It is therefore always fascinating to see even today the abundance of topics which are investigated and the associated fruitful results, simply by compressing (or expanding) such a lipid film. In this work, I could contribute a little to this successful life story of Langmuir Blodgett troughs. I hope that my results are a further proof that this method should not be written off just yet.

In this thesis, I was able to provide answers to transport processes in lipid monolayers, which are ultimately, all of biological relevance. In particular, I was interested in lipid oxidation and dynamic compression/expansion processes of surfactant monolayers at the air-water interface:

Lipid oxidation was shown to be a consequence of the formation of a high concentration of reactive oxygen species (ROS) during cell respiration, which finally can lead to severe cell damage. It is not yet understood clearly, which part of the lipid molecules is especially prone to a ROS attack. I was particularly interested in the role of the double bonds of the acyl chains of the lipid molecules during oxidation. Further, I wanted to know the time scales of lipid interaction with the ROS.

Compared to lipid vesicles, lipid monolayers have the advantage that many parameters of the system can be adjusted easily. In our system, I made use of this by setting the lateral pressure to low values during H_2O_2 treatment, which facilitated the ROS to reach the double bonds in the acyl chains.

A prime example of biological systems out of thermal equilibrium was given in the alveolus surface, which is covered with a surfactant monolayer. During breathing, these monolayers undergo such a highly dynamic compression and expansion. Arising flows from breathing could disrupt a film and consequently, it would lose its protective role. One of my goals was to understand flows and their influence on domain shape. Dependent on the strength of the flows, I expected different growth regimes, with differing prevailing transport processes. Once understanding the underlying mechanisms in domain shaping would allow me to draw conclusions on biological systems.

In order to address these questions, I established two systems, both based on the compression of lipid monolayers. I used isotherms to study the phase behavior of the lipids:[9] During compression, the lipids can undergo phase transitions from the gaseous phase to the liquid expanded phase (LE-phase) and further from the LE-phase to the liquid condensed phase (LC-phase). A coexistence regime is observed in between the LE-phase and the LC-phase, characterized by a flat increase of lateral pressure with decreasing molecular area. Some lipids exhibited LC-phase domains. These were further investigated with Brewster angle microscopy

(BAM). The used BAM was equipped with an integrated Scheimpflug optics, enabling an overall focused image plane. Furthermore, time-resolved observation of the growth of the domains was possible by recording videos (20 frames per seconds).

The first system enabled the investigation of lipid peroxidation, when the lipids were exposed to ROS. I chose DMPC, POPC, DOPC and PLPC, since these are phospholipids differing in the number and position of double bonds in acyl chains, but not in the head group. I used a H_2O_2 enriched phosphate buffered saline (PBS) solution, which served as a precursor for more reactive ROS, like hydroxyls (·OH). PBS was chosen, since it resembles the cell environment best. During defined waiting times of H_2O_2 treatment, the ROS diffused vertically from the subphase towards the monolayer. The lipid molecules were in the LE-phase, which facilitated the ROS molecules to reach also the double bonds of the acyl chains. The oxidized monolayers were then compressed at constant compression speed. Since the corresponding isotherms could be measured with high precision, the relative area increase $\delta A/A$ between oxidized and non-oxidized monolayer along the isotherm proved to be a good measure for lipid peroxidation. The area increase δA in the molecular area of the oxidized molecules was explained by the eventually added, more hydrophilic −OOH group at the position of a carbon atom adjacent to a double bond in the unsaturated acyl chain. The −OOH group is drawn to the hydrophilic head group of the lipid. This leads to a kink in the acyl chain, which increases the molecular area A by δA. A model, which explained this peroxidation process in lipid vesicles,[48] could be adopted to monolayers.

I compared the oxidation of phospholipids, differing in the number and position of the double bonds of their acyl chains. I found that $\delta A/A$ increased with the growing number of double bonds in one acyl chain. However, a comparison of DOPC with POPC also showed the importance of the position of the acyl chain. I determined a slow reaction kinetic. It could be estimated by a $\sqrt{t}$ dependence of the number density $N_{surface}$, which denominates the ROS sticking on the monolayer. The transport of ROS towards the monolayer was found to be diffusive, because it was the slowest process in the reaction. This interpretation was reinforced by a comparison of the temperature dependence of the relative area increase $\delta A/A$ with the Stokes-Einstein diffusion coefficient of water molecules. The initial ROS concentration c_0 in the trough could be traced back ($c_0 \sim 50\ nM$), which is indeed a realistic value found in human cells.

Concluding, our results can be understood as a feasibility study. The complexity of the monolayer can be arbitrarily increased, for example by the addition of proteins, allowing the investigation of other oxidative processes occurring in the cell membrane.

The second system allowed the investigation of growth of LC domains during fast compression processes of monolayers. I chose erucic acid monolayers, due to its low line tension and a continuous nucleation phase, enabling the formation of fractal domains. The monolayers were investigated with isotherms and BAM videos. Since v_C (compression speed of the monolayer) was continuous over the whole compression time, I had a system with well-defined hydrodynamic conditions. This allowed me a complete analysis of the system, starting with descriptive features of the observed domains to a classification of the observed growth

regimes by means of hydrodynamic theory, through to the distinction and quantification of different kind of flows and supersaturations, involving Ivantsov theory:[55, 68, 69]

Dependent on the compression speed v_C, I observed seaweed or dendritic domains. The LE/LC phase transition pressure π_t was slightly increased compared to π_∞ of the equilibrium isotherm. A high compression speed v_C induced a supersaturation Δc. I introduced the excess lateral pressure $\Delta\pi = \pi - \pi_\infty$ as an appropriate quantity to describe the supersaturation Δc. I showed a linear behavior of Δc on $\Delta\pi$. Δc is a macroscopic quantity since it is averaged over the whole monolayer area. I characterized the domains of the seaweed and dendritic regime with respect to tip radii, branch lengths, side branch separations and fractal dimensions. I calculated the growth speed of the main branches. A roughly doubling of the growth speed of dendritic domains, compared to seaweed domains was observed. This was an evidence of adjunctive (Marangoni) flow in the subphase.

For each monolayer, I observed drifts during domain growth, which I explained by an anisotropy in the LE-phase, caused by the continuous nucleation of the domains. These kind of surface flows were superimposed to bulk flows in the subphase. Since I had a well established system, I could analyze the influence of these surface flows on domain shape, in terms of magnitude, direction and duration of the surface flows. I therefore used FFT spectra and directionality histograms. At low flows, the FFT showed six-fold symmetry. Higher drifts exhibited incisions in the FFT, eventually leading to dumbbell shaped FFTs at very high drifts. The domains grew preferentially in the direction parallel to the incision.

I used directionality histograms to analyze the angular distribution of the growing domains. They showed that the drift direction always correlated with a minimum in the histogram. In order to analyze drift duration, I split the domain in downstream and upstream side. I could show that for small drift durations, downstream growth was preferred. However, for longer drift durations, the flows got more isotropic and consequently growth was more balanced then.

I could observe only a weak correlation between drift velocity v_D and compression speed v_C. However, dendrites were formed when the compression speed v_C was high, while seaweed domains were formed when v_C was small. Domain distortion occurred in the same way, independent if seaweed or dendritic domains were considered. I further showed that hydrodynamic flows in the subphase and surface flows are superimposed and scale differently. Consequently, they have different impact on domain shape: hydrodynamic flows act on μm scale and influence the domain morphology (distance between side branches, and tip radius) and the growth speed of the main branches. Surface flows act on the mm to cm scale, cause an anisotropic flow in the LE phase surrounding the domain, and thus affect the overall domain shape.

The anisotropy in the LE-phase led to a locally different degree of supersaturation. To take this into account, I introduced a local normalized supersaturation Δ, based on the Ivantsov solution.[55, 68] Therefore, I calculated Péclet numbers p of measured quantities of the system. I obtained values of $0.88 \leq \Delta \leq 0.90$ for the seaweed regime ($p < 5$) and $0.93 \leq \Delta \leq 0.96$ for the dendritic regime ($p > 6$). Since the Ivantsov solution can only be applied for purely diffusive

processes, I applied a modified Ivantsov solution Δ_{mod},[70, 72] which calculates Δ at a distance δ ahead of the dendrite tip. I was able to determine the progression of the diffusive layer δ, however a quantitative determination failed.

Applying hydrodynamic theory allowed me to classify the two growth regimes with respect to the Boussinesq number Bq. Since for both growth regimes, I achieved values of $Bq < 1$, bulk viscous losses dominated over surface viscous losses. Further, a cross-over length ξ was calculated, from which one can distinguish, whether advective transport dominates over diffusion.

I further connected the two defined supersaturations Δ and Δc via the excess lateral pressure $\Delta\pi$. From this, I saw differences in the seaweed and dendritic growth regimes: The local normalized supersaturation Δ of seaweed growth seemed to be quite stable for a further increase of the lateral excess pressure $\Delta\pi$, whereas it reacted quite sensitive in the dendritic regime. This was found to be an indication of a non-equilibrium regime, caused by the strong coupling of the monolayer to the subphase. It reinforces therefore the theory of Marangoni-flow.[19]

The findings of this thesis emphasize the importance of understanding highly dynamic compression/expansion processes arising in surfactant monolayers. Using the example of the compression of the alveolus surface, it can be seen that a more realistic model of the pulmonary alveolus is not only enabled by increasing the complexity of the surfactant monolayer (e.g. by adding specific proteins or lipid mixtures to the monolayer). Equally important is the understanding in transport processes and the consequences for the monolayer structure. By the analysis of domain shapes, I presented a method, which is suitable for such a study.

7. Bibliography

1. Ulman, A., Formation and structure of self-assembled monolayers. *Chemical reviews* **1996,** *96* (4), 1533-1554.
2. Halley, J. D.; Winkler, D. A., Consistent concepts of self-organization and self-assembly. *Complexity* **2008,** *14* (2), 10-17.
3. Yamamoto, S.; Maruyama, Y.; Hyodo, S.-a., Dissipative particle dynamics study of spontaneous vesicle formation of amphiphilic molecules. *The Journal of chemical physics* **2002,** *116* (13), 5842-5849.
4. Mondal, J.; Yethiraj, A., Driving force for the association of amphiphilic molecules. *The Journal of Physical Chemistry Letters* **2011,** *2* (19), 2391-2395.
5. Jadhav, S. M.; Morey, P.; Karpe, M. M.; Kadam, V., Novel vesicular system: an overview. *Journal of applied pharmaceutical science* **2012,** (Issue), 193-202.
6. Rasaiah, J. C.; Garde, S.; Hummer, G., Water in nonpolar confinement: from nanotubes to proteins and beyond. *Annu Rev Phys Chem* **2008,** *59*, 713-40.
7. Southall, N. T.; Dill, K. A.; Haymet, A., A view of the hydrophobic effect. ACS Publications: 2002; Vol. 106, pp 521-533.
8. Gokel, G. W.; Negin, S., Synthetic membrane active amphiphiles. *Advanced drug delivery reviews* **2012,** *64* (9), 784-796.
9. Kaganer, V. M.; Möhwald, H.; Dutta, P., Structure and phase transitions in Langmuir monolayers. *Reviews of Modern Physics* **1999,** *71* (3), 779.
10. Albrecht, O.; Gruler, H.; Sackmann, E., Polymorphism of phospholipid monolayers. *Journal de Physique* **1978,** *39* (3), 301-313.
11. Blume, A., Lipids at the air–water interface. *ChemTexts* **2018,** *4* (1), 3.
12. Marsh, D., Lateral pressure in membranes. *Biochimica et Biophysica Acta (BBA)-Reviews on Biomembranes* **1996,** *1286* (3), 183-223.
13. Cevc, G., How membrane chain-melting phase-transition temperature is affected by the lipid chain asymmetry and degree of unsaturation: an effective chain-length model. *Biochemistry* **1991,** *30* (29), 7186-7193.
14. Lipowsky, R.; Sackmann, E., *Structure and dynamics of membranes: I. from cells to vesicles/II. generic and specific interactions*. Elsevier: 1995.
15. Möhwald, H.; Dietrich, A.; Bohm, C.; Brezesinski, G.; Thoma, M., Domain formation in monolayers. *Mol Membr Biol* **1995,** *12* (1), 29-38.
16. Israelachvili, J., Self-assembly in two dimensions: surface micelles and domain formation in monolayers. *Langmuir* **1994,** *10* (10), 3774-3781.
17. Kuzmin, P. I.; Akimov, S. A.; Chizmadzhev, Y. A.; Zimmerberg, J.; Cohen, F. S., Line tension and interaction energies of membrane rafts calculated from lipid splay and tilt. *Biophysical journal* **2005,** *88* (2), 1120-1133.
18. Sriram, I.; Schwartz, D. K., Line tension between coexisting phases in monolayers and bilayers of amphiphilic molecules. *Surface Science Reports* **2012,** *67* (6), 143-159.
19. Bruinsma, R.; Rondelez, F.; Levine, A., Flow-controlled growth in Langmuir monolayers. *The European Physical Journal E* **2001,** *6* (3), 191-200.

20. Gutierrez-Campos, A.; Diaz-Leines, G.; Castillo, R., Domain growth, pattern formation, and morphology transitions in Langmuir monolayers. A new growth instability. *The Journal of Physical Chemistry B* **2010,** *114* (15), 5034-5046.
21. Meunier, J., Why a Brewster angle microscope? *Colloids and Surfaces A: Physicochemical and Engineering Aspects* **2000,** *171* (1-3), 33-40.
22. Vollhardt, D., Brewster angle microscopy: A preferential method for mesoscopic characterization of monolayers at the air/water interface. *Current opinion in colloid & interface science* **2014,** *19* (3), 183-197.
23. Hoenig, D.; Moebius, D., Direct visualization of monolayers at the air-water interface by Brewster angle microscopy. *The Journal of Physical Chemistry* **1991,** *95* (12), 4590-4592.
24. Dickinson, B. C.; Chang, C. J., Chemistry and biology of reactive oxygen species in signaling or stress responses. *Nat Chem Biol* **2011,** *7* (8), 504-11.
25. Winterbourn, C. C., Reconciling the chemistry and biology of reactive oxygen species. *Nat Chem Biol* **2008,** *4* (5), 278-86.
26. Johnson, D. R.; Decker, E. A., The role of oxygen in lipid oxidation reactions: a review. *Annual review of food science and technology* **2015,** *6*, 171-190.
27. Kumar, S.; Yadav, D. K.; Choi, E. H.; Kim, M. H., Insight from Molecular dynamic simulation of reactive oxygen species in oxidized skin membrane. *Sci Rep* **2018,** *8* (1), 13271.
28. Borst, J. W.; Visser, N. V.; Kouptsova, O.; Visser, A. J., Oxidation of unsaturated phospholipids in membrane bilayer mixtures is accompanied by membrane fluidity changes. *Biochimica et Biophysica Acta (BBA)-Molecular and Cell Biology of Lipids* **2000,** *1487* (1), 61-73.
29. Runas, K. A.; Malmstadt, N., Low levels of lipid oxidation radically increase the passive permeability of lipid bilayers. *Soft Matter* **2015,** *11* (3), 499-505.
30. Beranova, L.; Cwiklik, L.; Jurkiewicz, P.; Hof, M.; Jungwirth, P., Oxidation changes physical properties of phospholipid bilayers: fluorescence spectroscopy and molecular simulations. *Langmuir* **2010,** *26* (9), 6140-4.
31. Cadet, J.; Delatour, T.; Douki, T.; Gasparutto, D.; Pouget, J.-P.; Ravanat, J.-L.; Sauvaigo, S., Hydroxyl radicals and DNA base damage. *Mutation Research/Fundamental and Molecular Mechanisms of Mutagenesis* **1999,** *424* (1-2), 9-21.
32. Yurkova, I. L., Free-radical reactions of glycerolipids and sphingolipids. *Russian Chemical Reviews* **2012,** *81* (2), 175.
33. De Rosa, R.; Spinozzi, F.; Itri, R., Hydroperoxide and carboxyl groups preferential location in oxidized biomembranes experimentally determined by small angle X-ray scattering: Implications in membrane structure. *Biochimica et Biophysica Acta (BBA)-Biomembranes* **2018,** *1860* (11), 2299-2307.
34. Pratt, D. A.; Mills, J. H.; Porter, N. A., Theoretical calculations of carbon− oxygen bond dissociation enthalpies of peroxyl radicals formed in the autoxidation of lipids. *Journal of the American Chemical Society* **2003,** *125* (19), 5801-5810.
35. Yusupov, M.; Wende, K.; Kupsch, S.; Neyts, E. C.; Reuter, S.; Bogaerts, A., Effect of head group and lipid tail oxidation in the cell membrane revealed through integrated simulations and experiments. *Sci Rep* **2017,** *7* (1), 5761.
36. Walling, C., Fenton's reagent revisited. *Accounts of chemical research* **1975,** *8* (4), 125-131.
37. Fenton, H., LXXIII.—Oxidation of tartaric acid in presence of iron. *Journal of the Chemical Society, Transactions* **1894,** *65*, 899-910.

38. Li, Q.-T.; Yeo, M. H.; Tan, B. K., Lipid peroxidation in small and large phospholipid unilamellar vesicles induced by water-soluble free radical sources. *Biochemical and Biophysical Research Communications* **2000,** *273* (1), 72-76.
39. Albertini, R.; Rindi, S.; Passi, A.; Pallavicini, G.; De Luca, G., Heparin protection against Fe2+-and Cu2+-mediated oxidation of liposomes. *FEBS letters* **1996,** *383* (3), 155-158.
40. Gröning, A.; Ahrens, H.; Ortmann, T.; Lawrenz, F.; Brezesinski, G.; Scholz, F.; Helm, C. A., Molecular mechanisms of phosphatidylcholine monolayer solidification due to hydroxyl radicals. *Soft matter* **2011,** *7* (14), 6467-6476.
41. Hörl, W. H., Iron therapy for renal anemia: how much needed, how much harmful? *Pediatric nephrology* **2007,** *22* (4), 480-489.
42. Lim, P.-S.; Wei, Y.-H.; Yu, Y. L.; Kho, B., Enhanced oxidative stress in haemodialysis patients receiving intravenous iron therapy. *Nephrology Dialysis Transplantation* **1999,** *14* (11), 2680-2687.
43. Roob, J. M.; Khoschsorur, G.; Tiran, A.; HORINA, J. H.; Holzer, H.; Winklhofer-Roob, B. M., Vitamin E attenuates oxidative stress induced by intravenous iron in patients on hemodialysis. *Journal of the American Society of Nephrology* **2000,** *11* (3), 539-549.
44. Cordeiro, R. M., Reactive oxygen species at phospholipid bilayers: distribution, mobility and permeation. *Biochim Biophys Acta* **2014,** *1838* (1 Pt B), 438-44.
45. Tauffenberger, A.; Magistretti, P. J., Reactive oxygen species: beyond their reactive behavior. *Neurochemical Research* **2021,** *46*, 77-87.
46. Gellert, F.; Ahrens, H.; Helm, C. A., Oxidation of Unsaturated Phospholipids: A Monolayer Study. *Langmuir* **2020,** *36* (41), 12213-12220.
47. Wong-Ekkabut, J.; Xu, Z.; Triampo, W.; Tang, I.-M.; Tieleman, D. P.; Monticelli, L., Effect of lipid peroxidation on the properties of lipid bilayers: a molecular dynamics study. *Biophysical journal* **2007,** *93* (12), 4225-4236.
48. Riske, K. A.; Sudbrack, T. P.; Archilha, N. L.; Uchoa, A. F.; Schroder, A. P.; Marques, C. M.; Baptista, M. S.; Itri, R., Giant vesicles under oxidative stress induced by a membrane-anchored photosensitizer. *Biophysical journal* **2009,** *97* (5), 1362-1370.
49. Itri, R.; Junqueira, H. C.; Mertins, O.; Baptista, M. S., Membrane changes under oxidative stress: the impact of oxidized lipids. *Biophys Rev* **2014,** *6* (1), 47-61.
50. Haluska, C. K.; Baptista, M. S.; Fernandes, A. U.; Schroder, A. P.; Marques, C. M.; Itri, R., Photo-activated phase separation in giant vesicles made from different lipid mixtures. *Biochimica et Biophysica Acta (BBA)-Biomembranes* **2012,** *1818* (3), 666-672.
51. Miller, A.; Möhwald, H., Diffusion limited growth of crystalline domains in phospholipid monolayers. *The Journal of chemical physics* **1987,** *86* (7), 4258-4265.
52. Miller, A.; Knoll, W.; Möhwald, H., Fractal growth of crystalline phospholipid domains in monomolecular layers. *Physical review letters* **1986,** *56* (24), 2633.
53. Suresh, K.; Nittmann, J.; Rondelez, F., Pattern formation during phase transition in Langmuir monolayers near critical temperature. *Europhysics Letters* **1988,** *6* (5), 437.
54. Helm, C. A.; Moehwald, H., Equilibrium and nonequilibrium features determining superlattices in phospholipid monolayers. *The Journal of Physical Chemistry* **1988,** *92* (5), 1262-1266.
55. Ihle, T. Wachstumsmuster unter diffusivem Transport. PhD, RWTH Aachen, 1996.
56. Akamatsu, S.; Bouloussa, O.; To, K.; Rondelez, F., Two-dimensional dendritic growth in Langmuir monolayers of D-myristoyl alanine. *Physical Review A* **1992,** *46* (8), R4504.

57. Gehlert, U.; Vollhardt, D., Nonequilibrium structures in 1-monopalmitoyl-rac-glycerol monolayers. *Langmuir* **1997,** *13* (2), 277-282.
58. Weidemann, G.; Gehlert, U.; Vollhardt, D., Inner structure of condensed phase domains in monolayers at the air-water interface. *Langmuir* **1995,** *11* (3), 864-871.
59. Iimura, K.-i.; Yamauchi, Y.; Tsuchiya, Y.; Kato, T.; Suzuki, M., Two-dimensional dendritic growth of condensed phase domains in spread monolayers of cis-unsaturated fatty acids. *Langmuir* **2001,** *17* (15), 4602-4609.
60. Flores, A.; Corvera-Poiré, E.; Garza, C.; Castillo, R., Growth and morphology in Langmuir monolayers. *Europhysics Letters (EPL)* **2006,** *74* (5), 799-805.
61. Ihle, T.; Müller-Krumbhaar, H., Fractal and compact growth morphologies in phase transitions with diffusion transport. *Physical Review E* **1994,** *49* (4), 2972.
62. Gellert, F.; Ahrens, H.; Wulff, H.; Helm, C. A., Seaweed and Dendritic Growth in Unsaturated Fatty Acid Monolayers. *Membranes* **2022,** *12* (7), 698.
63. Vollhardt, D., Effect of unsaturation in fatty acids on the main characteristics of Langmuir monolayers. *The Journal of Physical Chemistry C* **2007,** *111* (18), 6805-6812.
64. Grotberg, J. B., Pulmonary flow and transport phenomena. *Annual review of fluid mechanics* **1994,** *26* (1), 529-571.
65. Zhang, Z.; Kleinstreuer, C., Transient airflow structures and particle transport in a sequentially branching lung airway model. *Physics of Fluids* **2002,** *14* (2), 862-880.
66. Chourpiliadis, C.; Bhardwaj, A., *Physiology, Respiratory Rate*. StatPearls Publishing, Treasure Island (FL): 2022.
67. Braun, R. J., Dynamics of the tear film. *Annual Review of Fluid Mechanics* **2012,** *44*, 267-297.
68. Ivantsov, G., Temperature field around a spherical, cylindrical, and needle-shaped crystal, growing in a pre-cooled melt. *Dokl. Akad. Nauk. SSSR* **1985,** *58*, 567-569.
69. Langer, J. S., Instabilities and pattern formation in crystal growth. *Reviews of Modern Physics* **1980,** *52* (1), 1-28.
70. Cantor, B.; Vogel, A., Dendritic solidification and fluid flow. *Journal of Crystal Growth* **1977,** *41* (1), 109-123.
71. Gandin, C.-A.; Guillemot, G.; Appolaire, B.; Niane, N. T., Boundary layer correlation for dendrite tip growth with fluid flow. *Materials Science and Engineering: A* **2003,** *342* (1-2), 44-50.
72. McFadden, S.; Browne, D. J., A generalised version of an Ivantsov-based dendrite growth model incorporating a facility for solute measurement ahead of the tip. *Computational Materials Science* **2012,** *55*, 245-254.
73. Cevc, G.; Marsh, D., *Phospholipid bilayers*. John Wiley & Sons, Inc.: New York, 1987.
74. Johnson, C. A., Generalization of the Gibbs-Thomson equation. *Surface Science* **1965,** *3* (5), 429-444.
75. Mullins, W. W.; Sekerka, R., Stability of a planar interface during solidification of a dilute binary alloy. *Journal of applied physics* **1964,** *35* (2), 444-451.
76. Peters, R.; Beck, K., Translational diffusion in phospholipid monolayers measured by fluorescence microphotolysis. *Proceedings of the National Academy of Sciences* **1983,** *80* (23), 7183-7187.
77. Tocanne, J.-F.; Dupou-Cézanne, L.; Lopez, A., Lateral diffusion of lipids in model and natural membranes. *Progress in lipid research* **1994,** *33* (3), 203-237.
78. Lindblom, G.; Orädd, G., Lipid lateral diffusion and membrane heterogeneity. *Biochimica et Biophysica Acta (BBA)-Biomembranes* **2009,** *1788* (1), 234-244.

79. Marsh, D., Thermodynamic analysis of chain-melting transition temperatures for monounsaturated phospholipid membranes: dependence on cis-monoenoic double bond position. *Biophysical journal* **1999,** *77* (2), 953-963.
80. Harvey, B. L.; Downey, R., The inheritance of erucic acid content in rapeseed (Brassica napus). *Canadian Journal of Plant Science* **1964,** *44* (1), 104-111.
81. Hénon, S.; Meunier, J., Microscope at the Brewster angle: Direct observation of first-order phase transitions in monolayers. *Review of Scientific Instruments* **1991,** *62* (4), 936-939.
82. Marsh, D., Comment on Interpretation of Mechanochemical Properties of Lipid Bilayer Vesicles from the Equation of State or Pressure− Area Measurement of the Monolayer at the Air− Water or Oil− Water Interface. *Langmuir* **2006,** *22* (6), 2916-2919.
83. Wilke, N.; Vega Mercado, F.; Maggio, B., Rheological properties of a two phase lipid monolayer at the air/water interface: effect of the composition of the mixture. *Langmuir* **2010,** *26* (13), 11050-11059.
84. David; Lide, R., CRC Handbook of Chemistry and Physics, Internet Version 2005. 95 ed.; CRC Press: Boca Raton, FL, 2005; p. 985. <http://www.hbcpnetbase.com> (accessed November 2022).
85. Pockels, A., On the relative contamination of the water-surface by equal quantities of different substances. *Nature* **1892,** *46* (1192), 418-419.
86. Möhwald, H., Phospholipid and phospholipid-protein monolayers at the air/water interface. *Annual Review of Physical Chemistry* **1990,** *41* (1), 441-476.

8. Symbol directory

A	(molecular) area
A_∞	molecular area at the phase transition pressure
Bq	Boussinesq number
c	surface concentration in inverse units of the molecular area
$c_{LC,eq}$	surface solute concentrations the condensed phase (LC-phase)
$c_{LE,eq}$	surface solute concentrations in the fluid phase (LE-phase)
c_∞	surface concentration of amphiphiles in the LE-phase, in the phase transition region, far away from a domain boundary, calculated from the equilibrium isotherms
c_s	surface concentration of amphiphiles in the LC-phase, calculated at high pressure area from the isotherms
c_0	increased surface concentration of the LE-phase, close to the domain boundary, in accordance with $c_0 = c_\infty + \Delta c$
C_p	heat capacity
D	diffusion coefficient: if not further specified, of the LE-phase
D_C	chemical diffusity
D_F	fractal dimension
$\vec{f}$	body forces
F	Surface free energy
I	unit matrix: if not further specified, three-dimensional
k	Boltzmann constant
L	latent heat
l	diffusion length
M	mobility
p	Péclet number
p_h	hydrodynamic pressure
q	wavenumber

R	tip radius
Re	Reynolds number
Sc	Schmidt number
t	time
T	temperature
T_0	constant temperature at isothermal conditions
u	dimensionless diffusion field
$\vec{v}$	velocity
v_C	compression speed
v_{growth}	growth speed (of the main domain branches)
x	cartesian coordinate
y	cartesian coordinate
z	cartesian coordinate

– –

α	parabolic/ paraboloidal coordinate
α_B	parabola/ paraboloid at the diffusion zone δ
β	parabolic/ paraboloidal coordinate
γ	line tension
δ	diffusion layer
δ_C	diffusion layer, applied to chemical diffusion
δ_{ij}	Kronecker delta
Δ	dimensionless supersaturation, corresponding to the Ivantsov solution
Δc	supersaturation
$\Delta_{convective}$	convective correction term of Δ
Δ_{mod}	modified dimensionless supersaturation ahead of the dendrite tip, corresponding to the Ivantsov solution at the outer boundary of the diffusion layer δ
$\Delta\pi$	excess lateral pressure above the LE/LC phase transition at equilibrium conditions
ζ	ratio of surface viscosity to bulk viscosity

η	bulk viscosity
η_S	surface viscosity
θ	paraboloidal coordinate
κ	compressibility modulus
κ_C	radius of curvature
λ	mean distance between two side branches of a fractal domain
μ	chemical potential
$\mu_{LE,eq}(T_0)$	equilibrium chemical potential in the LE-phase
$\tilde{\mu}$	difference between μ and its equilibrium value $\mu_{LE,eq}(T_0)$ for two-phase coexistence at $T = T_0$
ν	kinematic viscosity
ξ	cross-over length between diffusive and advective transport
ξ_C	capillary length
π	lateral pressure
π_0	surface tension of pure water
π_∞	phase transition pressure at equilibrium conditions
ρ	mass density
σ	surface tension
σ_0	surface tension of pure water
$\overleftrightarrow{\sigma}$	stress tensor
$\overleftrightarrow{\tau}$	shear stress tensor
φ	argument of the complementary error function errfc(φ)

9. Abbreviations

BAM	Brewster angle microscope
DMPC	1,2-dimyristoyl-sn-glycero-3-phosphocholine
DOPC	1,2-dioleoyl-sn-glycero-3-phosphocholine
errf	error function
errfc	complementary error function
FFT	Fast Fourier Transformation
LC-phase	liquid condensed phase
LE-phase	liquid expanded phase
·OH	hydroxyl radical
PLPC	1-palmitoyl-2-linoleoyl-sn-glycero-3-phosphocholine
POPC	1-palmitoyl-2-oleoyl-glycero-3-phosphocholine
ROS	reactive oxygen species

10. Author contributions

Article 1: **Gellert, F.**, Ahrens, H. and Helm, C.A. (2020). Oxidation of Unsaturated Phospholipids: A Monolayer Study. *Langmuir*, 36(41), 12213–12220. (DOI: 10.1021/acs.langmuir.0c01950)

F.G., H.A. and C.A.H. conceived and designed the experiments. F.G. performed the experiments and H.A. supervised the experiments. F.G. did the numerical data validation with Matlab. F.G., H.A. and C.A.H. analyzed and discussed the results. F.G., H.A. and C.A.H. developed a model of lipid peroxidation of Langmuir monolayers in terms of molecular area increase. F.G. and C.A.H. wrote the manuscript. All authors have read and agreed to the published version of the manuscript.

Article 2: **Gellert, F.**, Ahrens, H., Wulff, H. and Helm, C.A. (2022). Seaweed and Dendritic Growth in Unsaturated Fatty Acid Monolayers. *Membranes*, *12*(7), 698. (DOI: 10.3390/membranes12070698)

F.G., H.A. and C.A.H. conceived and designed the experiments. F.G. performed the experiments. F.G. did the numerical data analysis with Matlab. F.G. applied ImageJ and self-written Matlab scripts for image processing of the BAM images and implemented a Matlab routine to determine the fractal dimension of processed BAM movies. F.G., H.A., H.W. and C.A.H. analyzed and discussed the results. F.G. and C.A.H. wrote the manuscript. All authors have read and agreed to the published version of the manuscript.

Article 3: **Gellert, F.**, Ahrens, H. and Helm, C.A. (2023). Influence of Surface Flows on the Shape of Fractal Domains. *Langmuir*, 39(26), 9078–9084. (DOI: 10.1021/acs.langmuir.3c00815)

F.G., H.A. and C.A.H. conceived and designed the experiments. F.G. performed the experiments. F.G. did the numerical data analysis: self-written Matlab scripts for processing of the BAM images, determination of their FFTs and directionality histograms with ImageJ. F.G., H.A. and C.A.H. analyzed and discussed the results. F.G. and C.A.H. wrote the manuscript. C.A.H. put the results in a biological context. All authors have read and agreed to the published version of the manuscript.

Greifswald, 09.08.2023

Prof. Dr. Christiane A. Helm Florian Gellert

11. Scientific achievements (Publications & Conferences)

11.1. Publications

I. Moseev, D., Laqua, H. P., Marsen, S., Stange, T., Braune, H., Erckmann, V., **Gellert, F.** and Oosterbeek, J. W. (2016) Absolute calibration of sniffer probes on Wendelstein 7-X. Review of Scientific Instruments, Vol. 87. (DOI: 10.1063/1.4960349)

II. Moseev, D., Laqua, H. P., Marsen, S., Marushchenko, N., Stange, T. , Braune, H., **Gellert**, **F.**, Hirsch, M., Hoefel, U., Knauer, J., Oosterbeek, J. W. , Turkin Y. and The Wendelstein 7-X Team. (2016). Inference of the microwave absorption coefficient from stray radiation measurements in Wendelstein 7-X. Nuclear Fusion, Vol. 57. (DOI: 10.1088/1741-4326/aa4f13)

III. **Gellert, F.**, Ahrens, H. and Helm, C.A. (2020). Oxidation of Unsaturated Phospholipids: A Monolayer Study. Langmuir, 36(41), 12213–12220. (DOI: 10.1021/acs.langmuir.0c01950)

IV. **Gellert, F.**, Ahrens, Wulff, H., H. and Helm, C.A. (2022). Seaweed and Dendritic Growth in Unsaturated Fatty Acid Monolayers. Membranes, *12*(7), 698. (DOI: 10.3390/membranes12070698)

V. **Gellert, F.**, Ahrens, H. and Helm, C.A. (2023). Influence of Surface Flows on the Shape of Fractal Domains. Langmuir, 39(26), 9078–9084. (DOI: 10.1021/acs.langmuir.3c00815)

11.2. Conference Contributions

11.2.1. Conference talks

VI. 22.06.2018 **Gellert, F.** and Helm, C.A., Tag der Wissenschaft, University of Greifswald, Greifswald, Germany: Untersuchung dünner Lipid-Filme an Luft/Wasser-Grenzflächen.

VII. 22.09. – 25.09.2018 **Gellert, F.**, Ahrens, H. and Helm, C.A., 7th Workshop on Frontiers in Redox Biochemistry and Medicine, Rostock, Germany: Effect of ROS on supramolecular structure of model membranes.

VIII. 13.09. – 15.09.2020 **Gellert, F.**, Ahrens, H. and Helm, Baltic Redox Workshop Greifswald, Germany: Effect of ROS on supramolecular structure of model membranes.

IX. 04.09. – 04.09.2022 **Gellert, F.**, Ahrens, H., Wulff, H. and Helm DPG Spring Meeting Condensed Matter Section Regensburg, Germany: Seaweed and dendritic domains of erucic acid monolayers.

11.2.2. Poster presentations

X. 10.03. – 15.03.2018 **Gellert, F.**, Ahrens, H. and Helm, C.A., DPG Spring Meeting Condensed Matter Section Berlin Germany: Surface micelles in lipid monolayers in the LE-phase.

XI. 30.03. – 04.04.2019 **Gellert, F.**, Ahrens, H. and Helm, C.A., DPG Spring Meeting Condensed Matter Section Regensburg, Germany: Effect of reactive oxygen and nitrogen species on lipid monolayers.

12. Publications

12.1. Article 1

Article 1

Oxidation of Unsaturated Phospholipids: A Monolayer Study

Florian Gellert, Heiko Ahrens and Christiane A. Helm

Langmuir

2020, Volume 36, 12213−12220

Published: September 28th, 2020

Supplementary information can be found in: DOI: 10.1021/acs.langmuir.0c01950

This research was originally published in Langmuir, **Gellert, F.**; Ahrens, H.; Helm, C. A., Oxidation of Unsaturated Phospholipids: A Monolayer Study. *Langmuir* **2020,** *36* (41), 12213-12220.

LANGMUIR

pubs.acs.org/Langmuir Article

Oxidation of Unsaturated Phospholipids: A Monolayer Study

Florian Gellert, Heiko Ahrens, and Christiane A. Helm*

Cite This: *Langmuir* 2020, 36, 12213–12220 Read Online

ACCESS | Metrics & More | Article Recommendations | Supporting Information

ABSTRACT: Lipid oxidation does strongly influence the self-organization of plasma membranes; the detailed influence is not yet clear. In this work, phospholipid monolayers at the air/water interface were used as model membranes. Oxidation was induced by the reactive oxygen species formed in a H_2O_2-enriched solution. The reaction was found to be diffusion-limited; the concentration of the reactive oxygen species was about 50 nM. Isotherms were recorded for different phosphatidylcholines with saturated and unsaturated acyl chains. For unsaturated lipids, the isotherms showed a constant relative molecular area increase after oxidization, independent of the molecular area and dependent on the degree of peroxidation. Similarly, the compressibility modulus was unchanged, but shifted to larger molecular areas. The correlation between peroxidation and changes of the interaction forces between the lipid molecules is discussed.

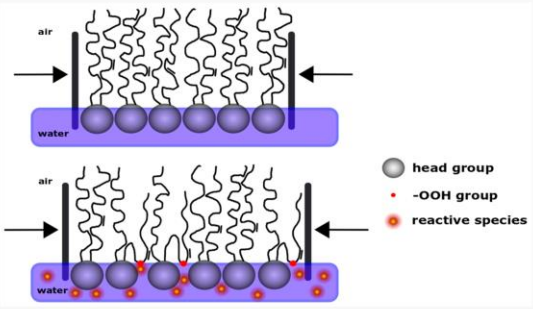

INTRODUCTION

Lipid molecules in the plasma or mitochondrial membrane are prone to damage from reactive oxygen species (ROS).[1] Lipid peroxidation disrupts the cell membrane, leading to derangement of structure and function of the membrane.[2] A prolonged oxidative damage is toxic and contributes significantly to the aging process of the cell.[3]

Therefore, lipid exposure to oxidative stress has been extensively investigated on small, large, and giant unilamellar vesicles.[4−6] In most in vitro studies, the process of oxidation was catalyzed either by a Fenton reaction[7,8] or by irradiation of an incorporated photosensitive molecule into the membrane.[9,10] In this way, highly reactive oxygen species (ROS) are generated, which immediately react with the lipid bilayer. On the molecular level, an oxidation alters the chemical structure of the lipid molecules. It was found that oxidative stability decreases with increasing degree of unsaturated double bonds.[11] In terms of the complete bilayer structure, the treated vesicle alters its size and possibly its shape,[9] due to a (locally) increased molecular area of the oxidized lipid (cf., Scheme 1). Therefore, physical properties of the membrane, like fluidity[12] or permeability,[13,14] are also affected.

We want to find out if lipid monolayers can be used as model membranes to study the effects of ROS. Monolayers at the air/water interface[15] are interesting from a physical point of view, because external parameters are easily adjustable, for example, salt concentration, temperature, or pH-value.[16,17] In contrast to vesicles, the molecular area in a Langmuir monolayer can be varied. Isotherms are measured, which determine the lateral pressure in dependence of molecular area.

Scheme 1. Suggested Molecular Mechanism of Area Increase at the Monolayer Level for POPC Molecules[a]

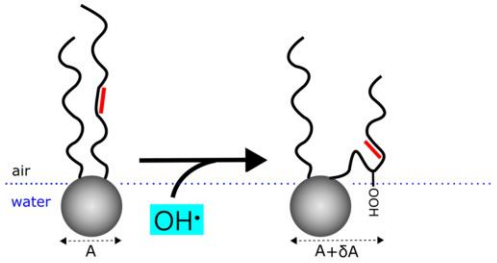

[a]Initiated by a hydroxyl radical ·OH; the group −OOH is eventually attached at either the 9′ or the 10′ position. Because of its more hydrophilic character, it is drawn toward the headgroup at the water interface, leading to a molecular area increase δA. Adapted from Riske et al.[9]

Here we present a feasibility study where lipids are treated with ROS in the gaseous phase, which is less densely packed than the lipids in vesicles (lateral pressure of vesicles ∼32 mN/m).[18] This facilitates the ROS reaching the hydrophobic

Received: July 2, 2020
Revised: September 11, 2020
Published: September 28, 2020

https://dx.doi.org/10.1021/acs.langmuir.0c01950
Langmuir 2020, 36, 12213−12220

moiety of the lipid monolayer. In addition, knowing the isotherms allows one to determine the derived physical parameters, like the compressibility modulus κ.

One aim of this work was to investigate how the number of double bonds and their location on one or two acyl chains influences lipid peroxidation. Phosphatidylcholines with identical headgroups but different saturated and unsaturated acyl chains were investigated. Phosphatidylcholine was chosen for analyzing lipid oxidation, because of its high biological relevance. It is the most abundant phospholipid in mammalian cell membranes.[19] The relative molecular area increase between oxidized and nonoxidized monolayer along the isotherm was used as a measure for oxidation. This has been done for the following four lipids: 1,2-dimyristoyl-*sn*-glycero-3-phosphocholine (DMPC), 1,2-dioleoyl-*sn*-glycero-3-phosphocholine (DOPC), 1-palmitoyl-2-oleoyl-glycero-3-phosphocholine (POPC), and 1-palmitoyl-2-linoleoyl-*sn*-glycero-3-phosphocholine (PLPC).

From the literature, it is known that mainly the short living and highly reactive hydroxyl radical is responsible for membrane damage in the cells.[20] Moreover, ozone in the ppm concentration range ($c(O_3)$ = 0.5−30 ppm) well above ambient conditions induces lipid oxidation.[21−23] In laboratory conditions, hydroxyl radicals are often generated via the well-known Fenton reaction.[24,25] Thereby, iron Fe^{2+} is oxidized to Fe^{3+} by hydrogen peroxide, H_2O_2, to catalyze the disproportionation of hydrogen peroxide into a hydroxyl radical ·OH and a hydroxide ion OH^-. Because free iron ions are harmful for the cell,[26−28] in this work it has been decided to forego on the addition of iron. Free Fe^{2+} ions bind to the headgroups of lipid monolayers and strongly alter the isotherm.[29] Instead, a highly concentrated hydrogen peroxide-enriched solution (~1 M H_2O_2) was used as a precursor for higher reactive radicals, keeping in mind that the expected radical concentrations from self-dissociation of H_2O_2 are very low (some nM). The use of such high H_2O_2 concentrations was suggested by recent results of Dana Thal,[30] who proved that nonphoto activated H_2O_2 itself has no effect on self-assembled monolayer degradation in concentrations around 0.01 M. Only at higher H_2O_2 concentration ROS are produced. Once generated, the hydroxyl radicals in the subphase of the trough reach the lipid monolayer by diffusion from below. Provided there is enough space between the lipid molecules of the monolayer, the ROS have easy access not only to the headgroup but also to the acyl chains. Riske et al.[9] proposed an explanation of the structural changes on the molecular level by oxidation for vesicles. They observed that mainly the acyl chains are affected. Initiated by a free radical (e.g., superoxide O_2^- or hydroxyl radical ·OH), hydrogen is abstracted from a carbon atom adjacent to a double bond in the unsaturated acyl chain from lipid L. This is the preferred position for a radical attack, because the carbon−hydrogen bond is weakend by the neighbored, electron-rich double bond. The so formed lipid radical L· can react covalently with available singlet oxygen $^1O_2$, but also with the more stable triplet oxygen $^3O_2$ to form a peroxyl radical LOO·. Like the initiating reactive oxygen radical, also the peroxyl radical is able to remove a hydrogen atom from the surrounding lipid molecules, resulting in hydroperoxides LOOH. The eventually added, more hydrophilic −OOH group is drawn to the hydrophilic headgroup of the lipid, leading to a kink in the acyl chain, which increases the molecular area A by δA. Scheme 1 shows this reaction applied to monolayers.

This article is organized as follows: (i) The isotherms of the different lipids are shown and compared. (ii) The lipid monolayers in the gaseous phase are subjected to ROS for different times; the changes to the isotherms are determined, and the relative area increase is established. (iii) The bulk modulus of the lipid monolayer, which is the inverse of the compressibility modulus, was compared before and after oxidation for POPC. (iv) From the exposure time, the concentration of ROS in the aqueous solution was estimated, and the reaction rates were compared.

MATERIALS AND METHODS

Materials. 1,2-Dimyristoyl-*sn*-glycero-3-phosphocholine (DMPC), 1,2-dioleoyl-*sn*-glycero-3-phosphocholine (DOPC), 1-palmitoyl-2-oleoyl-glycero-3-phosphocholine (POPC), and 1-palmitoyl-2-linoleoyl-*sn*-glycero-3-phosphocholine (PLPC) were purchased from Avanti, Alabaster, AL. Chloroform, phosphate buffered saline (Roti Cell PBS), and stabilized hydrogen peroxide (30%) are from Carl Roth, Karlsruhe, Germany. The pure water is provided from a Milli-Q Synthesis system with a nominal conductance of 0.054 μS.

Pockels−Langmuir Trough and Isotherms. Compression surface pressure isotherms (Π−A isotherms) are recorded on a Teflon trough (Riegler & Kirstein, Potsdam, Germany). A Wilhelmy plate surface pressure sensor with a filter paper as a plate (accuracy of 0.1 mN/m) was used. The trough area is 3.5 × 30 cm^2. The compression speed is 0.07 ± 0.03 nm^2/(molecule·min). The experiments were performed in ambient air. Ozone concentration was not controlled but estimated from environmental data to be lower than 0.09 ppm. The phospholipids were dissolved in chloroform solution (c = 0.1 mM). The solution was spread with a 100 μL syringe (model 1710, Hamilton, Bonaduz, Switzerland), and the chloroform was allowed to dissipate for a few minutes. The trough temperature is kept constant ±0.1 °C with a thermostat (DC-30 Thermo-Haake, Haake Technik, Karlsruhe, Germany). Hydrogen peroxide-enriched PBS buffer solution was freshly prepared for each measurement and pipetted into the Langmuir trough. The composition of the pure buffer solution is 154.004 mM NaCl, 5.599 mM Na_2HPO_4, and 1.058 mM KH_2PO_4. For all lipid monolayers, the same subphase was used. The subphase pH was 7.4 ± 0.1 as was verified with a pH-meter.

A small amount of lipids was spread onto H_2O_2-enriched PBS buffer solution ($c(H_2O_2)$ = 1.06 M) to ensure that the lipids were in the gaseous phase (~200 $Å^2$/ molecule) at their first contact with reactive oxygen species. After a defined waiting time, the monolayer was compressed and the isotherm was recorded. Each isotherm was measured after temperature equilibration was achieved. Shown is the mean compression isotherm (N = 2), which was obtained by determining the arithmetic mean at each molecular area.

RESULTS AND DISCUSSION

We investigated monolayers of four different phosphocholine molecules with a different number of double bonds in the acyl chain. First, DMPC (14:0 PC) monolayers with two saturated acyl chains were investigated, and the isotherm was recorded (cf., Figure 1a). At large molecular areas, the surface pressure is almost zero, as expected for the gaseous phase.[31] At 90 $Å^2$/ molecule, the lateral pressure increases slowly. This is typical for the liquid expanded (LE) phase. At a surface pressure of 14 mN/m, the isotherm shows a kink. On further compression, the increase in surface pressure is very low. This is the liquid expanded/liquid condensed (LE/LC) phase transition as described in the literature.[15,32] On further compression, at 50 $Å^2$/molecule, the LE/LC phase transition is almost completed, and in the LC phase the surface pressure increases steeply.

Oxidation was induced by the exposure of the lipid monolayers to a H_2O_2-enriched PBS buffer solution (1.06 M H_2O_2). The lipids were in the gaseous phase (~200 $Å^2$/

https://dx.doi.org/10.1021/acs.langmuir.0c01950
Langmuir 2020, 36, 12213−12220

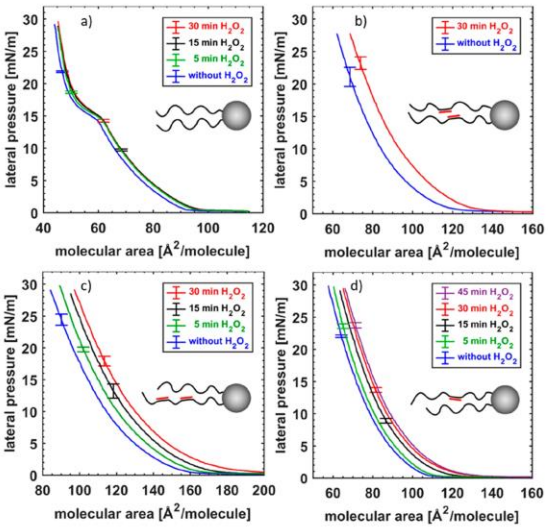

Figure 1. Isotherms of (a) DMPC, (b) DOPC, (c) PLPC, and (d) POPC monolayers, for different exposure times to the H_2O_2-enriched subphase. Mean isotherms were obtained by taking the arithmetic average of isotherms obtained from two different monolayers. Trough temperature was 8 °C, subphase PBS buffer and 1.06 M H_2O_2, as indicated. For each isotherm, an exemplary error bar is included.

molecule). This large molecular area was selected to minimize interaction between the molecules. Therefore, the reactive oxygen species (ROS) from the subphase can easily access both the headgroups and the acyl chains. Compression of the DMPC monolayer started after a defined exposure time to the subphase. An exposure time of 5 min led to a shift of the isotherm to a slightly larger molecular area. Longer exposure times had no significant additional effect.

POPC (16:0−18:1 PC) has the same headgroup as DMPC, but one double bond at the longer acyl chain. Its isotherms are shown in Figure 1 d. As compared to DMPC, the onset of the LE phase occurs at larger molecular areas (~110 Å²/molecule). On compression, the POPC monolayer remains in the more disordered LE phase over the whole pressure range. This is expected because the unsaturated bond in one acyl chain introduces a kink in the otherwise all-trans conformation for this acyl chain. This kink makes the parallel arrangement of the acyl chains of the ordered LC phase impossible. Therefore, the molecule requires a larger area of ~60 Å²/molecule even at high pressure.

After 5 min of exposure to H_2O_2-enriched PBS solution, the isotherm is shifted to larger molecular areas. Longer exposure times increase this shift (cf., Figure 1d).

Because one double bond in one acyl chain had such a pronounced effect, the next lipid investigated was DOPC (18:1 PC (Δ9 cis)) with two double bonds, that is, one double bond at each acyl chain (cf., Figure 1b). The isotherms on PBS solution were very similar to that of POPC: a gaseous phase is followed by a LE phase; the transition from the gaseous to LE phase occurs at the same molecular area (~120 Å²/molecule). Even the molecular area at 30 mN/m is about the same (~58 Å²/molecule). Exposure to ROS led to a shift of the isotherm to larger molecular areas. Qualitatively, it appears that the effect of ROS on DOPC and POPC monolayers is about the same.

To find out more about the change in conformation of phosphatidylcholines on addition of ROS, PLPC (16:0−18:2 PC), a lipid with two unsaturated bonds in one acyl chain, was investigated. Shown is the isotherm of a PLPC monolayer on a PBS subphase (cf., Figure 1c). The LE phase begins at even larger molecular areas than were observed for POPC (at ~160 Å²/molecule). This observation suggests additional increased disorder of the acyl chains. On exposure of the lipid monolayer to ROS in the subphase for 5 min, an even more pronounced shift of the isotherm to larger molecular areas is observed. Longer exposure times (15, 30 min) increase the shift.

To summarize the observations from the isotherms, on exposure of the lipid monolayer in the gaseous phase to a H_2O_2-enriched PBS subphase, a shift of the isotherm to larger molecular areas is observed. The isotherms show that this effect is less pronounced for DMPC with saturated acyl chains (cf., Figure 1a) than for POPC, DOPC, and PLPC, the lipid monolayers with unsaturated acyl chains (cf., Figure 1b−d).

On the basis of the isotherms shown in Figure 1, the relative increase of the molecular area has been determined. It is defined as the ratio of area increase δA to the molecular area of the untreated monolayer, A. δA depends on the ROS exposure time. As a typical example, Figure 2 shows the relative

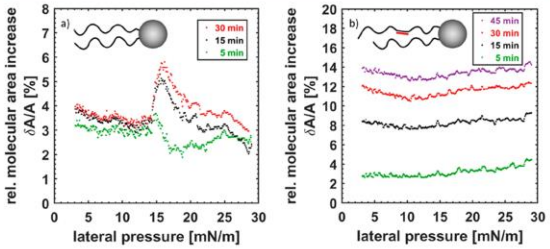

Figure 2. Relative molecular area increase of (a) DMPC and (b) POPC monolayers after different exposure times to the H_2O_2-enriched subphase as deduced from isotherms shown in Figure 1a and d, respectively.

molecular area increase $\delta A/A$ along the isotherm for DMPC and POPC monolayers. DMPC shows a rather small area increase (~4%) within the first 5 min. For longer exposure times, the isotherm does not change. Oxidation seems to be nearly completed. The relative area increase shows a peak between ~15 and 18 mN/m. This peak is derived from changes in the coexistence region of the LE/LC phase transition. On longer exposure time (cf., Figure 1), the slope in the transition region increases. Such an increased slope has been observed in the coexistence region of monolayers consisting of less than pure lipids.[33] Beside the effect of the increased slope in the coexistence region, the relative area increase $\delta A/A$ is constant and independent of exposure time.

Like DMPC monolayers, POPC monolayers (cf., Figure 2b) show for 5 min of exposure time a constant relative area increase along the whole pressure range of the isotherm. However, on increase of the exposure time from 5 to 45 min, the relative area increase grows from 3% to 15%. A constant relative pressure increase was found for all investigated lipids with an unsaturated bond in the acyl chain(s). Therefore, we conclude that a fraction of lipid molecules is affected by the

https://dx.doi.org/10.1021/acs.langmuir.0c01950
Langmuir 2020, 36, 12213−12220

exposure to H_2O_2. These affected molecules require a larger area and thus shift the isotherm to larger molecular areas. With increasing exposure time, the number of affected molecules increases and thus the average area per molecule.

To probe the lateral interaction between the lipid molecules, not only the isotherm but also the bulk modulus κ is considered, which is the inverse of the area compressibility modulus. It is defined as

$$\kappa(A) = -A\left(\frac{d\Pi}{dA}\right)_T \quad (1)$$

where Π, the lateral pressure, is the difference between the surface tension of the pure subphase and the surface tension of the subphase covered by a lipid monolayer.[16] Figure 3 shows κ

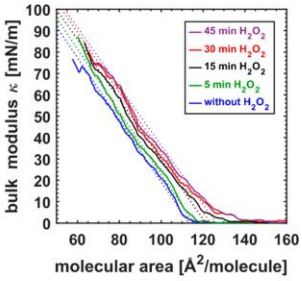

Figure 3. Bulk modulus κ of POPC (solid line) for different exposure times to a H_2O_2-enriched subphase. κ is obtained from the averaged isotherms shown in Figure 1d using eq 1. The dotted lines are linear fits to κ according to eq 2.

for POPC, deduced from the isotherms presented in Figure 1d. It increases linearly on decrease of the molecular area. The dotted lines are linear fits to the data, showing a linear increase of κ on film compression with slope α [mN/m·Å^2] and axis intercept β [mN/m] according to

$$\kappa = -\alpha A + \beta \quad (2)$$

Table 1 contains the coefficients as deduced from least-squares fits shown in Figure 3. Note that the slope α of κ stays

Table 1. Coefficients Obtained by Least Square Fits of Equation 2 to the Bulk Moduli κ Shown in Figure 3

exposure time t [min]	slope α [mN/m·Å^2]	axis intercept β [mN/m]
without H_2O_2	−1.45	164.3
5	−1.46	169.2
15	−1.40	170.0
30	−1.41	173.6
45	−1.38	174.2

unchanged (α = [−1.42 ± 0.034] mN/m·Å^2) after oxidation. However, the axis intercept β increases, quantifying the shift of the onset of $\kappa(A)$ at larger molecular areas. From the bulk modulus, we conclude that POPC remains in the LE phase after exposure to ROS; the lateral interaction between the lipid molecules remains basically unchanged.

As already the isotherms of the different lipids show (cf., Figure 1), the number and position of double bonds influence the changes the lipid monolayer experiences during oxidation. To compare the different lipids, the relative molecular area $\delta A/A$ increase is depicted in Figure 4 for all investigated lipid

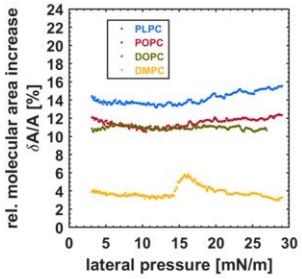

Figure 4. Relative molecular area increase of all investigated lipids, after 30 min of H_2O_2 exposure.

monolayers for an exposure time of 30 min. DMPC with no double bonds shows the weakest relative area increase, and PLPC with two double bonds on one acyl chain shows the strongest. Between those lie DOPC and POPC, with one double bond at each acyl chain and only one acyl chain with a double bond, respectively ($\delta A/A$ is 4% for DMPC, 11% for DOPC, 12% for POPC, and 14% for PLPC).

The similar relative area increase of DOPC and POPC indicates that the second double bond on the other acyl tail of DOPC was not accessible for the ROS attack in the monolayer. These results suggest that the area increase grows with the number of double bonds in one acyl chain.

To cross-check the results, the obtained relative molecular area increase in the monolayers was compared to results of earlier vesicle studies. Both experiments and molecular simulations showed a maximum area increase in the molecular area of oxidized lipids in vesicles of ∼15−20%,[4,34,35] measured when all lipids were oxidized. This is slightly more than observed in the experiments presented here, suggesting that not all lipid molecules are oxidized. This is consistent with the time dependence of the isotherms, which shift on increased oxidation time to a larger molecular area (cf., Figure 5). For

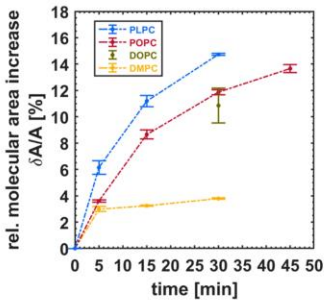

Figure 5. Relative area increase at 25 mN/m in dependence of the exposure time as deduced from the isotherm shown in Figure 1. The lines are guides to the eyes.

the lipid monolayers with at least one double bound in the acyl chain, saturation is not yet reached. Additionally, the oxidation of the monolayer, with the largest relative molecular area increase measured (PLPC at 8 °C, $\delta A/A$ = 15%, cf., Figure 5), did not reach saturation. Therefore, we conclude that the maximum molecular area increase possible is closer to 20% than to 15%.

https://dx.doi.org/10.1021/acs.langmuir.0c01950
Langmuir 2020, 36, 12213−12220

The observed effects are consistent with the concept of getting partially hydrophilic acyl chains by oxidation, presented in Scheme 1.

From the isotherms, the time dependence of the relative area increase can be quantified. An example at a selected surface pressure (25 mN/m) is shown in Figure 5, from all investigated lipid monolayers. As suggested earlier from the isotherms (cf., Figure 1a), DMPC shows a saturation after ∼5 min. The unsaturated lipids exhibit an ongoing area increase even after 30 min exposure time, even though the reaction slows down. From this slow reaction, it can be concluded that the highly concentrated H_2O_2 is not reacting directly with the molecules.[36] Instead, one possible explanation could be that H_2O_2 reacts as precursor for an unknown reactive oxygen species (ROS), possibly HO·, which diffuses toward the monolayer.

The slow reaction kinetic suggests a very small concentration of ROS. A possible way to determine the initial ROS concentration is to consider oxidation of the lipid molecules as molecular diffusion of ROS toward the monolayer,[37] that is, a diffusion limited reaction. We assume that each ROS, which reaches the monolayer, remains at the surface and reacts. It does not diffuse back into the aqueous solution. The number surface density $N_{surface}$, which is a measure of the number of ROS sticking on the monolayer, can be described by the diffusion equation:[38,39]

$$\frac{\delta N_{surface}}{\delta t} = c_0\sqrt{\frac{D_{bulk}}{\pi t}} \tag{3}$$

where c_0 is the ROS concentration and D_{bulk} is the diffusion constant of ROS. Solving this equation for $N_{surface}$ yields

$$N_{surface} = 2c_0\sqrt{D_{bulk}t/\pi} \tag{4}$$

$N_{surface}$ is proportional to the square root of time. Regarding oxidation of the investigated unsaturated lipid monolayers, this is indeed the case if one assumes a direct proportionality between the ROS number surface density and the molecular area increase, that is, if one assumes that for each kind of lipid a defined fraction of ROS reacts. Equation 4 then can be transcribed to

$$\delta A/A = m_T\cdot\sqrt{t} \tag{5}$$

where m_T is simply the slope for a specific temperature. This linear behavior of the relative area increase versus $\sqrt{t}$ is illustrated in Figure 6 for POPC monolayers. To further cross-check the model, measurements were performed at three different temperatures (8, 20, and 28 °C). One observes a steeper slope, that is, a more pronounced relative area increase at elevated temperature.

The area increase accompanied by a ROS attack can be described by adding a mean piece of area ΔA to the molecular area of the affected lipid molecules:

$$N_0\cdot A \xrightarrow{\text{ROS}} N_0\cdot A + N_{surface}\cdot\Delta A \tag{6}$$

Here, A and N_0 are the molecular area and number density of lipids before oxidation, respectively. N_0 can be expressed in terms of the lipid concentration c_{lipid}, the lipid spreading volume $V_{syringe}$, and the surface area of the Langmuir trough A_{trough}:

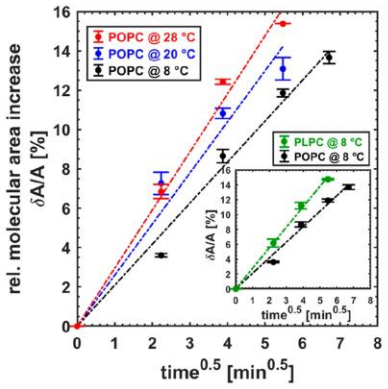

Figure 6. Relative molecular area increase in dependence of the square root of time. Data have been deduced from isotherms of POPC at a surface pressure of 25 mN/m for the temperatures indicated. A comparison of POPC with PLPC at 8 °C in the inset plot illustrates the faster oxidation for the double unsaturated lipid. The isotherms are shown in the Supporting Information. The lines are linear fits according to eq 5.

$$N_0 = \frac{c_{lipid}\cdot V_{syringe}\cdot N_{Avogadro}}{A_{trough}} \tag{7}$$

From experiments with lipid bilayers and our own results, the maximum relative area increase $\Delta A/A$ is about 20%.[4,34,35] The total area then is simply the sum of the film area before the ROS attack, $N_0\cdot A$, enhanced by the area increase of oxidation, $N_{surface}\cdot\Delta A$. The right-hand side of eq 6 can be expressed in terms of $\delta A/A$, which is known from Figure 6:

$$1 + \frac{N_{surface}}{N_0}\cdot\frac{\Delta A}{A} := 1 + \delta A/A, \text{ with}$$
$$\delta A/A = \frac{N_{surface}}{N_0}\cdot\frac{\Delta A}{A} := m_T\cdot\sqrt{t} \tag{8}$$

Hence, $N_{surface}$ can be found by rearranging eq 8:

$$N_{surface} = \delta A/A\cdot N_0\cdot\frac{A}{\Delta A} = m_T\cdot\sqrt{t}\cdot N_0\cdot\frac{A}{\Delta A} \tag{9}$$

To solve eq 4 for c_0, a few assumptions have been made. The ROS radius is in the order of the radius of water molecules (1.5 Å), such that the diffusion constant of water molecules can be assumed: $D(H_2O, 25\ °C) = 2.299\times10^{-9}$ m^2/s.[40,41] According to the Stokes−Einstein equation, the diffusion coefficient is

$$D_{bulk} := D = \frac{kT}{6\pi\eta r} \propto \frac{T}{\eta} \tag{10}$$

Here, k denotes the Boltzmann constant, T is the temperature, η is the viscosity of the aqueous solution, and r is the radius of the diffusing species. D scales with temperature and with the inverse of the viscosity.[42] The temperature increase of viscosity of liquids is described in detail in the literature,[43,44] enabling one to calculate the increase of D on temperature rise ($D(H_2O$, 8 °C) = 1.436×10^{-9} m^2/s, $D(H_2O$, 20 °C) = 2.023×10^{-9} m^2/s, and $D(H_2O$, 28 °C) = 2.476×10^{-9} m^2/s). Indeed, by increasing the temperature from 8 to 28 °C, the diffusion constant increases by 72%.

This is all one needs to finally solve eq 4 for c_0. For an exposure time of 30 min, one finally gets a concentration of

https://dx.doi.org/10.1021/acs.langmuir.0c01950
Langmuir 2020, 36, 12213−12220

reacting ROS, which increases slightly with temperature (c(8 °C) ≈ 48.2 nM, c(20 °C) ≈ 50.5 nM, and c(28 °C) ≈ 52.0 nM, respectively). These values are indeed low and in agreement with diffusion-limited aggregation, which led to the derivation of eq 4.

The oxidative stability of fatty acids and lipids is dependent on the number of double bonds at a carbon chain.[45] Oleic (18:1) acid and linoleic acid (18:2) differ in one double bond. An increase in the number of double bonds in a fatty acid by one increases the rate of oxidation at least by a factor of 2.[46,47] Thus, one would expect a higher reaction rate for PLPC than for POPC. Indeed, Figure 5 as well as the inset plot in Figure 6 show a faster relative area increase of PLPC as compared to POPC. The higher reaction rate must therefore manifest itself in the simple model used as increased concentration of reacting ROS on PLPC monolayers. To prove this, the concentration of ROS from PLPC monolayers at 8 °C was determined with a least-square fit to eq 4. This led to an apparent concentration c(PLPC, 8 °C) ≈ 63.6 nM, that is, 132% of the concentration observed for POPC. Because the subphase was the same, this result is not realistic. Hence, one may conclude that the second double bond leads to ∼32% more oxidation.

We conclude that the low concentration of the reactive oxygen species leads to a diffusion-limited reaction and explains the time dependence of lipid monolayer oxidation. A further indication of the important role of ROS diffusion can be gained by looking again at the Stokes−Einstein equation (cf., eq 10). On heating, D increases in the investigated temperature range by 72%. This large increase of D in temperature is due to its inverse proportionality with the viscosity, which in turn falls dramatically with temperature.[48] If the monolayer oxidation is diffusion limited, then the temperature behavior of the relative area increase should be in agreement with the Stokes−Einstein diffusion coefficient, provided eq 4 is valid and c_0 is constant. This assumption is justified from the determined ROS concentrations (50 ± 0.2 nM). Therefore, a normalized diffusion coefficient according to the Stokes−Einstein equation has been calculated and applied to the temperature dependence of the relative area increase. Figure 7 shows the comparison. The result is consistent with the hypothesis of a diffusion-limited reaction.

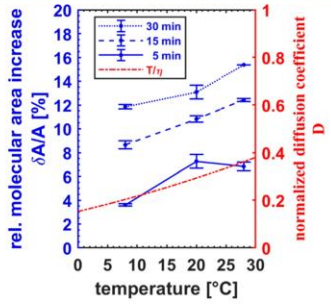

Figure 7. Temperature dependence of the relative area increase of POPC monolayers at 25 mN/m for different exposure times as indicated on an H_2O_2-enriched subphase (blue). Also shown is the normalized diffusion constant as described by eq 10 (red dashed line). Blue lines are guides to the eye.

CONCLUSIONS

The oxidation of monolayers of different phosphatidylcholines was studied at the air/water interface. To induce oxidation, a concentrated H_2O_2 solution was used; oxidation was initiated while the monolayer was in the gaseous phase. A measure for oxidation is the relative molecular area increase observed in the isotherm. Analysis of the isotherms showed that the relative area increase is independent of molecular area. Oxidation increases slowly with exposure time. Therefore, it was concluded that H_2O_2 was not reacting directly with the molecules but served as a precursor for another reactive oxidative species, probably hydroxyl radicals. Assuming diffusion limited oxidation, a ROS concentration of 50 ± 2 nM was calculated. A pronounced area increase was only observed when the acyl chains were unsaturated. The largest effect was observed with two double bonds in one acyl chain. The relative area increase then was larger, which was attributed to a faster reaction rate. These findings suggest that oxidation induces attachment of oxygen to the acyl chain, which increases the hydrophilic moiety of the molecule and thus the molecular area.

The results show that lipid monolayers are interesting model systems for the study of the interaction between reactive oxygen species and membranes.

ASSOCIATED CONTENT

Supporting Information

The Supporting Information is available free of charge at https://pubs.acs.org/doi/10.1021/acs.langmuir.0c01950.

Isotherms of all investigated lipids at different temperatures and for different exposure times, and the numerical values of the slopes indicated in Figure 6 (PDF)

AUTHOR INFORMATION

Corresponding Author

Christiane A. Helm − *Institute of Physics, University of Greifswald, Greifswald D-17489, Germany*; orcid.org/0000-0001-5181-1688; Phone: +49 3834 420 4710; Email: helm@uni-greifswald.de; Fax: +49 3834 420 4712

Authors

Florian Gellert − *Institute of Physics, University of Greifswald, Greifswald D-17489, Germany*

Heiko Ahrens − *Institute of Physics, University of Greifswald, Greifswald D-17489, Germany*

Complete contact information is available at: https://pubs.acs.org/10.1021/acs.langmuir.0c01950

Notes

The authors declare no competing financial interest.

ACKNOWLEDGMENTS

We thank Christopher H. Lillig and Harm Wulff for fruitful discussions on redox chemistry. This work is funded by the Deutsche Forschungsgemeinschaft (DFG, German Research Foundation) 231396381/RTG 1947.

REFERENCES

(1) Devasagayam, T. P. A.; Tilak, J. C.; Boloor, K. K.; Sane, K. S.; Ghaskadbi, S. S.; Lele, R. D. Free radicals and antioxidants in human

health: current status and future prospects. *J. Assoc. Phys. India* **2004**, *52*, 794−804.
(2) Devasagayam, T. P. A.; Boloor, K. K.; Ramasarma, T. Methods for estimating lipid peroxidation: An analysis of merits and demerits. *Indian J. Biochem. Biophys.* **2003**, *40*, 300−308.
(3) Cadenas, E.; Davies, K. J. A. Mitochondrial free radical generation, oxidative stress and aging. *Free Radical Biol. Med.* **2000**, *29*, 222−230.
(4) Weber, G.; Charitat, T.; Baptista, M. S.; Uchoa, A. F.; Pavani, C.; Junqueira, H. C.; Guo, Y.; Baulin, V. A.; Itri, R.; Marques, C. M.; Schroder, A. P. Lipid oxidation induces structural changes in biomimetic membranes. *Soft Matter* **2014**, *10*, 4241−4247.
(5) Breton, M.; Amirkavei, M.; Mir, L. M. Optimization of the Electroformation of Giant Unilamellar Vesicles (GUVs) with Unsaturated Phospholipids. *J. Membr. Biol.* **2015**, *248*, 827−835.
(6) Haluska, C. K.; Baptista, M. S.; Fernandes, A. U.; Schroder, A. P.; Marques, C. M.; Itri, R. Photo-activated phase separation in giant vesicles made from different lipid mixtures. *Biochim. Biophys. Acta, Biomembr.* **2012**, *1818*, 666−672.
(7) Li, Q.-T.; Yeo, M. H.; Tan, B. K. Lipid peroxidation in small and large phospholipid unilamellar vesicles induced by water-soluble free radical sources. *Biochem. Biophys. Res. Commun.* **2000**, *273*, 72−76.
(8) Albertini, R.; Rindi, S.; Passi, A.; Pallavicini, G.; De Luca, G. Heparin protection against Fe^{2+}- and Cu^{2+}-mediated oxidation of liposomes. *FEBS Lett.* **1996**, *383*, 155−158.
(9) Riske, K.; do, A.; Sudbrack, T.; de, P.; Archilha, N. L.; Uchoa, A. F.; Schroder, A. P.; Marques, C. M.; Baptista, M. S.; Itri, R. Giant Vesicles under Oxidative Stress Induced by a Membrane-Anchored Photosensitizer. *Biophys. J.* **2009**, *97* (5), 1362−1370.
(10) Zhou, Y.-M.; Liu, X.-C.; Li, Y.-Q.; Wang, P.; Han, R.-M.; Zhang, J.-P.; Skibsted, L. H. Synergy between plant phenols and carotenoids in stabilizing lipid-bilayer membranes of giant unilamellar vesicles against oxidative destruction. *Soft Matter* **2020**, *16*, 1792−1800.
(11) Johnson, D. R.; Decker, E. A. The role of oxygen in lipid oxidation reactions: A review. *Annu. Rev. Food Sci. Technol.* **2015**, *6*, 171−190.
(12) Borst, J. W.; Visser, N. V.; Kouptsova, O.; Visser, A. J. W. G. Oxidation of unsaturated phospholipids in membrane bilayer mixtures is accompanied by membrane fluidity changes. *Biochim. Biophys. Acta, Mol. Cell Biol. Lipids* **2000**, *1487*, 61−73.
(13) Runas, K. A.; Malmstadt, N. Low levels of lipid oxidation radically increase the passive permeability of lipid bilayers. *Soft Matter* **2015**, *11*, 499−505.
(14) Beranova, L.; Cwiklik, L.; Jurkiewicz, P.; Hof, M.; Jungwirth, P. Oxidation changes physical properties of phospholipid bilayers: fluorescence spectroscopy and molecular simulations. *Langmuir* **2010**, *26*, 6140−6144.
(15) Blume, A. Lipids at the air−water interface. *ChemTexts.* **2018**, *4*, 3.
(16) Kaganer, V. M.; Möhwald, H.; Dutta, P. Structure and phase transitions in Langmuir monolayers. *Rev. Mod. Phys.* **1999**, *71*, 779−819.
(17) Marsh, D. Lateral pressure in membranes. *Biochim. Biophys. Acta, Rev. Biomembr.* **1996**, *1286*, 183−223.
(18) Marsh, D. Comment on interpretation of mechanochemical properties of lipid bilayer vesicles from the equation of state or pressure-area measurement of the monolayer at the air-water or oil-water interface. *Langmuir* **2006**, *22*, 2916−2919.
(19) Koynova, R.; Caffrey, M. Phases and phase transitions of the phosphatidylcholines. *Biochim. Biophys. Acta, Rev. Biomembr.* **1998**, *1376*, 91−145.
(20) Cadet, J.; Delatour, T.; Douki, T.; Gasparutto, D.; Pouget, J.-P.; Ravanat, J.-L.; Sauvaigo, S. Hydroxyl radicals and DNA base damage. *Mutat. Res., Fundam. Mol. Mech. Mutagen.* **1999**, *424*, 9−21.
(21) Lai, C. C.; Yang, S. H.; Finlayson-Pitts, B. J. Interactions of monolayers of unsaturated phosphocholines with ozone at the air-water interface. *Langmuir* **1994**, *10*, 4637−4644.
(22) Wadia, Y.; Tobias, D. J.; Stafford, R.; Finlayson-Pitts, B. J. Real-time monitoring of the kinetics and gas-phase products of the reaction of ozone with an unsaturated phospholipid at the air-water interface. *Langmuir* **2000**, *16*, 9321−9330.
(23) Thompson, K. C.; Rennie, A. R.; King, M. D.; Hardman, S. J. O.; Lucas, C. O. M.; Pfrang, C.; Hughes, B. R.; Hughes, A. V. Reaction of a phospholipid monolayer with gas-phase ozone at the air-water interface: measurement of surface excess and surface pressure in real time. *Langmuir* **2010**, *26*, 17295−17303.
(24) Fenton, H. J. H. Oxidation of tartaric acid in presence of iron. *J. Chem. Soc., Trans.* **1894**, *65*, 899−910.
(25) Walling, C. Fenton's reagent revisited. *Acc. Chem. Res.* **1975**, *8*, 125−131.
(26) Hörl, W. H. Iron therapy for renal anemia: how much needed, how much harmful? *Pediatr. Nephrol.* **2007**, *22*, 480−489.
(27) Lim, P.-S.; Wie, Y.-H.; Yu, Y. L.; Kho, B. Enhanced oxidative stress in haemodialysis patients receiving intravenous iron therapy. *Nephrol., Dial., Transplant.* **1999**, *14*, 2680−2687.
(28) Roob, J. M.; Khoschsorur, G.; Tiran, A.; Horina, J. H.; Holzer, H.; Winklhofer-Roob, B. M. Vitamin E attenuates oxidative stress induced by intravenous iron in patients on hemodialysis. *J. Am. Soc. Nephrol.* **2000**, *11*, 539−549.
(29) Gröning, A.; Ahrens, H.; Ortmann, T.; Lawrenz, F.; Brezesinski, G.; Scholz, F.; Helm, C. A. Molecular mechanisms of phosphatidylcholine monolayer solidification due to hydroxyl radicals. *Soft Matter* **2011**, *7* (14), 6467−6476.
(30) Thal, D. A. Investigation of the antioxidative and radical scavenging impact of natural compounds in-vitro and on cell metabolism. Ph.D. Thesis; University of Greifswald, Germany, 2018.
(31) Albrecht, O.; Gruler, H.; Sackmann, E. Polymorphism of phospholipid monolayers. *J. Phys. (Paris)* **1978**, *39*, 301−313.
(32) Möhwald, H. Phospholipid and phospholipid-protein monolayers at the air/water interface. *Annu. Rev. Phys. Chem.* **1990**, *41*, 441−476.
(33) Miller, A.; Möhwald, H. Diffusion limited growth of crystalline domains in phospholipid monolayers. *J. Chem. Phys.* **1987**, *86* (7), 4258−4265.
(34) De Rosa, R.; Spinozzi, F.; Itri, R. Hydroperoxide and carboxyl groups preferential location in oxidized biomembranes experimentally determined by small angle X-ray scattering: Implications in membrane structure. *Biochim. Biophys. Acta, Biomembr.* **2018**, *1860*, 2299−2307.
(35) Wong-ekkabut, J.; Xu, Z.; Triampo, W.; Tang, I.-M.; Tieleman, D. P.; Monticelli, L. Effect of Lipid Peroxidation on the Properties of Lipid Bilayers: A Molecular Dynamics Study. *Biophys. J.* **2007**, *93*, 4225−4236.
(36) Chung, Y.-H.; Xia, J.; Margulis, C. J. Diffusion and Residence Time of Hydrogen Peroxide and Water in Crowded Protein Environments. *J. Phys. Chem. B* **2007**, *111*, 13336−13344.
(37) Schmitt, J.; Mächtle, P.; Eck, D.; Möhwald, H.; Helm, C. A. Preparation and Optical Properties of Colloidal Gold Monolayers. *Langmuir* **1999**, *15*, 3256−3266.
(38) Andrade, J. D. *Surface and Interfacial Aspects of Biomedical Polymers*; Plenum Press: New York, 1985.
(39) Crank, J. Infinite and semi-infinite media. *The Mathematics of Diffusion*; Oxford University Press: New York, 1995; pp 28−32.
(40) Mills, R. Self-Diffusion in Normal and Heavy Water in the Range 1−45°. *J. Phys. Chem.* **1973**, *77* (5), 685−688.
(41) Holz, M.; Heil, S. R.; Sacco, A. Temperature-dependent self-diffusion coefficients of water and six selected molecular liquids for calibration in accurate H NMR PFG measurements. *Phys. Chem. Chem. Phys.* **2000**, *2*, 4740−4742.
(42) Grigull, U.; Staub, J.; Schiebener, P. *Steam Table in SI-Unit, Concise Steam Properties of Ordinary Water Substance up to 1000°C and 100 MPa*; Springer: Berlin, 1984.
(43) Viswanath, D. S.; Gosh, T. K.; Prasad, D. H. L.; Dutt, N. V. K.; Rani, K. Y. *Viscosity of Liquids: Theory, Estimation, Experiment, and Data*; Springer Science & Business Media: Dordrecht, The Netherlands, 2007; pp 119−126.

https://dx.doi.org/10.1021/acs.langmuir.0c01950
Langmuir 2020, 36, 12213−12220

(44) Utracki, L. A. Temperature dependence of liquid viscosity. *J. Macromol. Sci., Part B: Phys.* **1974**, *10* (3), 477−505.
(45) Litwinienko, G.; Kasprzycka-Guttman, T. Study on the Autoxidation Kinetics of Fat Components by Differential Scanning Calorimetry. 2. Unsaturated Fatty Acids and Their Esters. *Ind. Eng. Chem. Res.* **2000**, *39*, 13−17.
(46) Richaud, E.; Audouin, L.; Fayolle, B.; Verdu, J.; Matisová-Rychlá, L.; Rychlý, J. Rate constants of oxidation of unsaturated fatty esters studied by chemiluminescence. *Chem. Phys. Lipids* **2012**, *165*, 753−759.
(47) Holman, R. T.; Elmer, O. C. The rates of oxidation of unsaturated fatty acids and esters. *J. Am. Oil Chem. Soc.* **1947**, *24*, 127−129.
(48) Lide, D. R., Ed. *CRC Handbook of Chemistry and Physics*, Internet Version 2005; http://www.hbcpnetbase.com; CRC Press: Boca Raton, FL, 2005; Vol. *85*, p 985.

https://dx.doi.org/10.1021/acs.langmuir.0c01950
Langmuir 2020, 36, 12213−12220

12.2. Article 2

Article 2

Seaweed and Dendritic Growth in Unsaturated Fatty Acid Monolayers

Florian Gellert, Heiko Ahrens, Harm Wulff and Christiane A. Helm

Membranes

2022, Volume 12, No 698

Published: July 8th, 2022

This research was originally published in Membranes, **Gellert, F.**; Ahrens, H.; Wulff, H.; Helm, C. A., Seaweed and Dendritic Growth in Unsaturated Fatty Acid Monolayers. *Membranes* **2022,** *12* (7), 698.

membranes

MDPI

Article

Seaweed and Dendritic Growth in Unsaturated Fatty Acid Monolayers

Florian Gellert, Heiko Ahrens, Harm Wulff and Christiane A. Helm *

Institute of Physics, University of Greifswald, Felix-Hausdorff-Straße 6, D-17489 Greifswald, Germany; gellertf@uni-greifswald.de (F.G.); heiko.ahrens.ellierode@web.de (H.A.); wulff@uni-greifswald.de (H.W.)
* Correspondence: helm@uni-greifswald.de

Abstract: The lateral movement in lipid membranes depends on their diffusion constant within the membrane. However, when the flux of the subphase is high, the convective flow beneath the membrane also influences lipid movement. Lipid monolayers of an unsaturated fatty acid at the water–air interface serve as model membranes. The formation of domains in the liquid/condensed coexistence region is investigated. The dimension of the domains is fractal, and they grow with a constant growth velocity. Increasing the compression speed of the monolayer induces a transition from seaweed growth to dendritic growth. Seaweed domains have broad tips and wide and variable side branch spacing. In contrast, dendritic domains have a higher fractal dimension, narrower tips, and small, well-defined side branch spacing. Additionally, the growth velocity is markedly larger for dendritic than seaweed growth. The domains' growth velocity increases and the tip radius decreases with increasing supersaturation in the liquid/condensed coexistence region. Implications for membranes are discussed.

Keywords: lipid monolayer; fractals; Marangoni flow

Citation: Gellert, F.; Ahrens, H.; Wulff, H.; Helm, C.A. Seaweed and Dendritic Growth in Unsaturated Fatty Acid Monolayers. *Membranes* **2022**, *12*, 698. https://doi.org/10.3390/membranes12070698

Academic Editor: Lucia Sessa

Received: 19 June 2022
Accepted: 5 July 2022
Published: 8 July 2022

1. Introduction

The phase diagrams of two-dimensional (2D) Langmuir monolayers of amphiphilic molecules show many states of matter that are the 2D analogs of the three-dimensional (3D) solid, liquid, and gaseous states of matter [1–4]. Therefore, one could assume that the characteristic nonequilibrium growth morphologies of 3D materials, such as dendrites and finger instabilities, have their counterparts in 2D. Indeed, "liquid-condensed" (LC) domains growing in a supercooled "liquid-expanded" (LE) monolayer exhibit fingering instabilities very similar to those found in bulk materials [5–10].

However, the growth mechanisms are different: fingering morphologies of 3D materials rely on generating latent heat at the moving liquid/solid interface. The diffusion of excess heat away from the interface proceeds more efficiently with a modulated interface (the "Mullins-Sekerka" instability [11,12]). In monolayers, heat generation at the LC/LE interface does not matter because the monolayer floats on a large volume of water that acts as an isothermal reservoir. Nevertheless, domains of fatty acid and lipid monolayers with growth instabilities leading to fractals have been observed with fluorescence [5,6] and Brewster-angle microscopy [7,8]. The latter has the advantage that no dye or additional marker molecules are required.

The LE/LC coexistence region of a monolayer differs from the liquid/solid coexistence region of 3D materials in two ways: (i) the dependence of surface tension on lipid concentration, and (ii) the unusually large difference in area density between the LE and LC phases (50 to 200%). Therefore, to sustain the growth of an LC domain, efficient transport of lipid molecules from the LE to the LC phase must occur. Two transport mechanisms in the LE phase are distinguished: surface diffusion within the lipid monolayer or hydrodynamic flow of the subphase (Marangoni effect).

Bruinsma and coworkers proposed this idea first [13]; their theoretical calculations were based on comparing surface and adjective flow. They predicted two distinctly different growth instability classes: (i) seaweed domains that grow by surface diffusion in the LE phase or (ii) dendritic domains whose growth is determined by the adjective flow beneath the lipid monolayer. The agreement was qualitative, but a quantitative comparison failed [7,14]. According to theory, seaweed growth should not occur because the surface viscosity (the viscosity in the lipid monolayer) is a few orders of magnitude too high [14,15]. We cannot resolve this issue, but to better understand the different growth instabilities, we quantify the shapes of seaweed and dendritic domains as a function of (i) the compression speed of the monolayer and (ii) the supersaturation in the LE phase.

The growth instabilities are determined by the drift velocity of the molecules in the LE phase towards the LE/LC domain boundary. Therefore, a meaningful parameter is the growth speed of the domains since it is proportional to the drift velocity of the molecules [13]. According to theory, the growth instabilities of the seaweed domains are less pronounced: their branches have tips with a larger radius. Furthermore, the separation between the branches is larger. This has consequences on the fractal dimension, which we determined.

In the past, dendritic growth and fingering instabilities were induced by pressure jumps, i.e., sudden increases in the supersaturation [6,7,9]. We decided to use a constant compression velocity because we wanted to have well-defined hydrodynamic conditions to investigate the time dependence of the domain parameters. Furthermore, domains that nucleated at different supersaturation levels within the coexistence region could be compared. We found that the compression speed determines if seaweed-like or dendritic domains grow.

As a model system, we have chosen an erucic acid monolayer [16]. The isotherms showed a low transition pressure with a broad coexistence region at the selected conditions (low temperature, low pH). The coexistence region was not flat, indicating a decreasing molecular area of the LE phase during compression. To quantify this supersaturation, the lateral pressure of the LE/LC phase transition π_∞ at equilibrium was measured with low compression velocity v_c. We observed that domain nucleation occurred at lateral pressures slightly above π_∞ and continued within the coexistence region. The excess lateral pressure $\Delta\pi = \pi_\infty - \pi$ was found to be a convenient parameter since it is proportional to supersaturation at low values of $\Delta\pi$. The supersaturation concentration Δc in units of $Å^{-2}$ was calculated from the area compressibility of the LE phase (cf. Appendix A).

The domains were imaged with Brewster Angle Microscopy at the beginning of the coexistence regime when isolated domains grew and the flow of the lipids in the LE phase was not influenced by neighboring domains. Their fractal dimension was calculated as outlined in Appendix B.

2. Materials and Methods

2.1. Materials

Erucic acid was purchased from Sigma-Aldrich (Merck KGaA), Darmstadt, Germany (purity $\geq$ 99%, according to supplier). To obtain the acidic subphase (pH 3), pure 37% muriatic acid (HCl) was used from Merck, Darmstadt, Germany. The pure water was provided by a Milli-Q Synthesis system with a nominal conductance of 0.054 µS.

2.2. Pockels-Langmuir Trough and Isotherms

Compression surface isotherms ($\pi - A$ isotherms) are recorded on a Teflon trough (Riegler & Kirstein, Potsdam, Germany). A Wilhelmy plate surface pressure sensor with a filter paper as a plate (accuracy of 0.1 mN/m) was used. The trough area is 3.5 × 30 cm^2. The compression speed can be varied. The experiments were performed in ambient air. The trough temperature was kept constant ±0.1 °C with a thermostat (DC-30 Thermo-Haake, Haake Technik, Karlsruhe, Germany). The fatty acid was dissolved in chloroform solution (c = 0.1 mM). The solution was spread with a 100 µL syringe (model 1710, Hamilton, Bonaduz, Switzerland) and the chloroform was allowed to dissipate for a few minutes.

Then, the monolayer was compressed with a predetermined compression speed and the isotherm was recorded.

2.3. Brewster Angle Microscopy (BAM)

The lipid films were studied by Brewster angle microscopy (BAM). A nanofilm_ultrabam from Accurion (Göttingen, Germany) was used to record real-time grayscale movies of the dendrite growth. Real-time grayscale videos were recorded at 20 frames per second with an image covering a surface area of about 0.24 mm^2 (using Scheimpflug's principle), corresponding to 1360 pixels × 1024 pixels and a spatial resolution of 2 µm. Due to the implemented Scheimpflug optics, it is possible to generate an overall focused image. However, the obtained images are distorted. The rectification and the background correction are performed by Accurion_Image (Accurion, Göttingen, Germany, version 1.2.3.).

2.4. Image Processing

2.4.1. Contrast Enhancement

To examine different properties of the dendritic growth behavior, it is important to have sharp-edged structures. The edge of the domains is limited by the resolution of the camera and the contrast of the image. Therefore, the generated BAM images were contrast-enhanced with a combination of ImageJ (version 1.53i9) and Matlab (version R2021a). Further investigations, for instance, the determination of the fractal dimension, required a black and white image, which was created with a Matlab routine, separating every pixel with gray values above a predefined threshold as domain and pixels with gray values below as background, respectively.

2.4.2. Determination of the Fractal Dimension

The fractal dimension of the structures was determined with a boxplot algorithm, developed by F. Moisy [17]. A detailed description of the calculation can be found in Appendix B.

3. Results and Discussion

3.1. Isotherms of Erucic Acid Monolayers at Different Compression Velocities

We studied acid molecules with uncharged head groups. Therefore, isotherms of erucic acid were recorded at low subphase pH (pH = 3). The temperature was kept constant at $T = \mathbf{10}$ °C. To approach equilibrium thermodynamics, the monolayer was compressed with a low compression velocity of $v_C = \mathbf{1.2}$ **Å²**/(molecule · min). The onset of the lateral pressure increase occurs at a molecular area of **48 Å²**. At further compression, the lateral pressure increases slowly and monotonously until a kink occurs, which marks the phase transition pressure $\pi_t \stackrel{!}{=} \pi_\infty$=**12.4** mN/m. The corresponding molecular area is $A_t \stackrel{!}{=} A_\infty = \mathbf{27.5}$ **Å²**. On further compression, the so-called coexistence regime is reached. While the molecular area decreases, the lipids undergo a phase transition from the LE to the LC phase. In the LC phase, the alkyl chains are ordered [2,3]. In the coexistence regime, the increase in lateral pressure is smaller than in the LE phase [16,18]. Compared to phospholipid monolayers, the pressure increase in the coexistence regime is rather steep [3,19,20]. Once the molecules are ordered, further compression in the LC phase leads to a steep pressure increase. Eventually, at a lateral pressure of 25 mN/m, the molecular area is 20 $Å^2$ [16].

The influence of the compression speeds v_C on the isotherms has been investigated. Figure 1 shows three typical isotherms of different compression velocities. The blue curve represents a slowly compressed monolayer close to the thermodynamic equilibrium. The other ones (black and red) are isotherms measured at higher compression velocities, which did not allow relaxation towards the thermodynamic equilibrium.

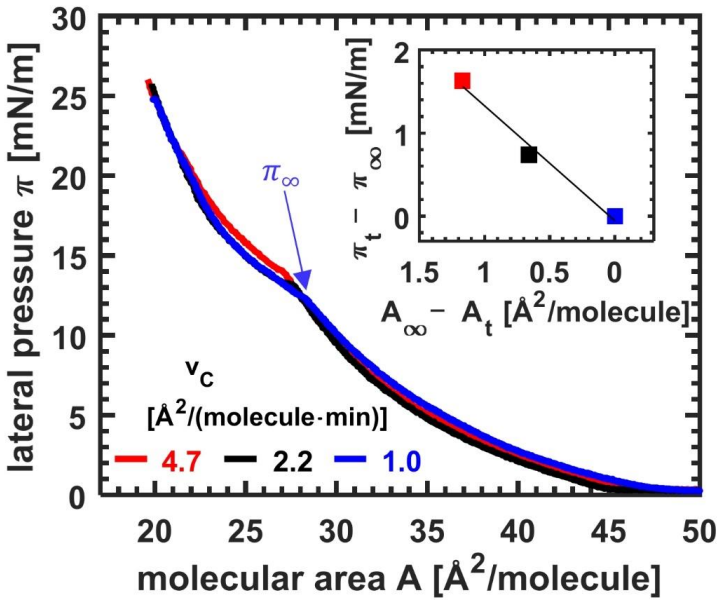

Figure 1. Isotherms of erucic acid monolayers at different compression velocities v_C at pH 3, $T = 10$ °C. The inset shows the shift of the phase transition lateral pressure $\pi_t - \pi_\infty$ in dependence on the shift in the molecular area, $A_\infty - A_t$, while v_C is increased. A blue arrow marks the transition pressure π_∞ for the isotherm measured at the lowest compression velocity, which is approximated as the equilibrium isotherm.

At large molecular areas, the isotherms are very similar. With the increase in the compression speed, the LE/LC phase transition occurs later, i.e., the lateral pressure π_t is increased while the molecular area A_t is decreased. From the inset of Figure 1, the intervals $A_\infty - A_t$ and $\pi_t - \pi_\infty$ are plotted for different compression speeds v_C. The slope of the line in the inset shows an increase in excess lateral pressure per molecular area decrease of $-\mathbf{1.38}$ mN/$\left(\mathrm{m} \cdot \mathbf{Å^2}\right)$.

3.2. Domain Growth Visualized with Brewster Angle Microscopy (BAM) Videos

The growth of domains was observed with Brewster Angle Microscopy (BAM). Domains started to grow at the beginning of the coexistence region, with a slight delay. Videos and isotherms were recorded simultaneously.

Figure 2 shows typical examples observed with different compression velocities v_C. Depicted is a time series of contrast-enhanced BAM images. At a low compression velocity (left, $v_C = 1.2$ $\mathbf{Å^2}/(\mathrm{molecule} \cdot \mathrm{min})$), a few domains nucleate. Figure 2 shows the growth of one domain during **72** s. These domains grew to a diameter of several 100 µm. The shape of the domains is somewhat arbitrary, and their side arms have a significant and not very well-defined separation. The described features are typically for seaweed domains [7].

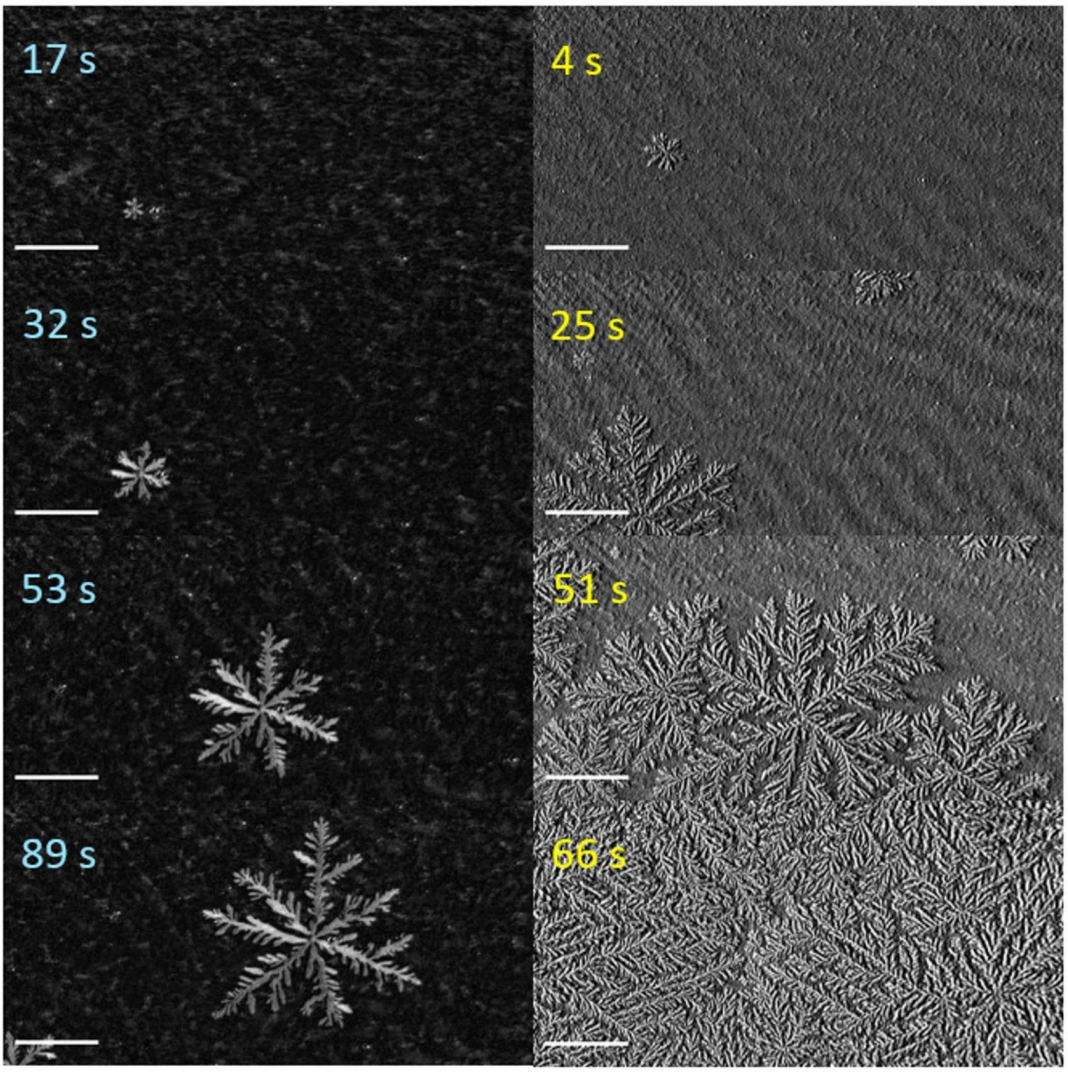

Figure 2. Domain growth in the LE/LC coexistence region of slowly (left, v_C = 1.2 $\mathbf{Å^2/}$(molecule · min)) and quickly compressed erucic acid monolayers (right, v_C = 2.3 $\mathbf{Å^2/}$(molecule · min)). The images were obtained with Brewster angle microscopy; all scale bars are 100 µm long. Experimental conditions as in Figure 1.

At a high compression velocity (Figure 2, right column, v_C = 2.3 $\mathbf{Å^2/}$(molecule · min)), a significantly higher number of domains nucleate and grow, in agreement with literature [21]. On further monolayer compression, the domains start interacting with each other, limiting their final size. After **62** s, the domain growth led to a carpet-like, wholly covered area. Compared to the seaweed domains, this suggests a faster domain growth. In contrast to the seaweed domains, the structures distinguish themselves by relatively thin and more straightened main and side branches. Additionally conspicuous is the significantly higher number of side branches, leading to needle-like forms. The described features are typical

for dendritic growth [7,13]. We conclude that depending on the compression velocity v_C, either seaweed or dendritic domains grow.

3.3. Parameters Characterizing Domain Growth

3.3.1. Influence of the Compression Velocity v_C on Fractal Dimension D_F

Fractals are visible in the observed structures. The fractal dimension D_F has been determined. The complexity of a pattern is quantified by the ratio of the change in detail to the change in scale [22]. A detailed description of the procedure is given in Appendix B. We determined the fractal dimension of a complete image, not only of a single domain. The limitation was the resolving power of the BAM. Figure 3 shows the fractal dimension's evolution as a function of time. At the beginning (t < 5 s), the domains are small, and so is the fractal dimension. The diameter of the domains is similar to the resolution of the BAM (2 µm). Therefore, the fractal dimension at an early growth stage has a broad error. The increase in the fractal dimension at the beginning is attributed to adding branches to the domain nuclei. After about twenty seconds, the fractal dimension is constant (within error). Additionally, Figure 3 shows that at a low compression velocity v_C, the fractal dimension D_F of the seaweed domains is considerably smaller than for dendrites grown at a larger v_C. For seaweed domains, $D_F = \mathbf{1.61}$ has been measured, whereas D_F is above 1.85 for dendritic domains. In the experiments shown, the fractal dimension D_F increases with v_C. The larger number of side branches leads to more complex structures and causes an additional increase in D_F. Concluding, the fractal dimension is an indicator to distinguish between the two growth classes with different pattern evolution.

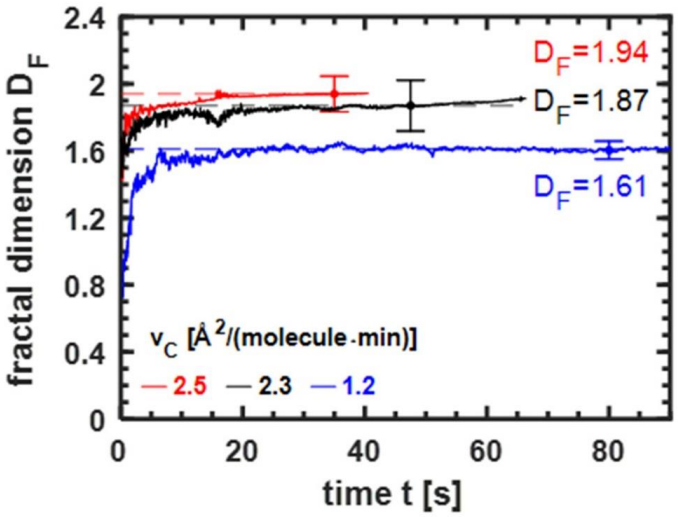

Figure 3. Fractal dimension D_F of the domains in the coexistence region of erucic acid monolayers (experimental conditions as in Figure 1) at different compression velocities v_C as a function of time t. The fractal dimension was determined as described in Appendix B. Exemplary error bars are included.

3.3.2. The Growth Speed v_R of the Domains

In Figure 2, the different time scales for LC domains in seaweed and dendritic growth regimes were apparent. To quantify this observation, the growth speed v_R was determined. Scheme 1 shows the investigated properties of a domain. To determine the growth speed v_R we focus on the main branches (cf. Figure 4, bottom). The branch length l defines the length of a main branch. From its time-dependent increase, the growth speed v_R is calculated (cf Figure 4, bottom).

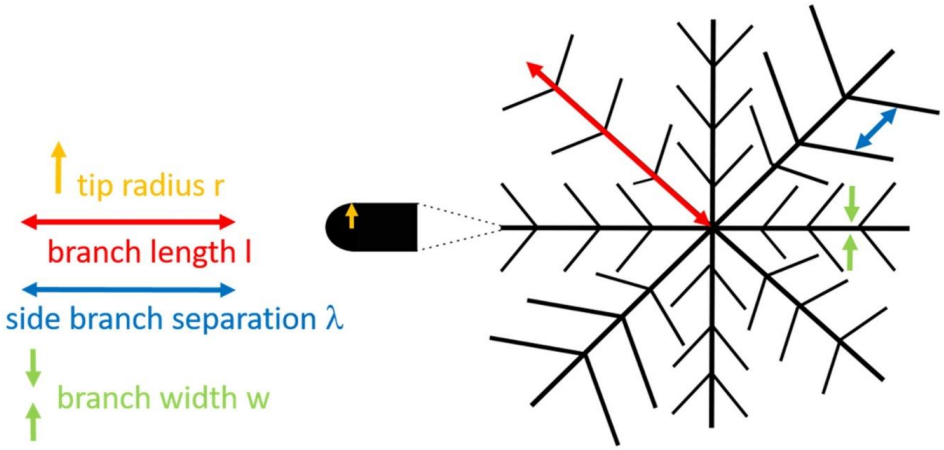

Scheme 1. The parameters characterizing a domain with a fractal dimension are branch length l, tip radius r, side branch separation λ, and branch width w.

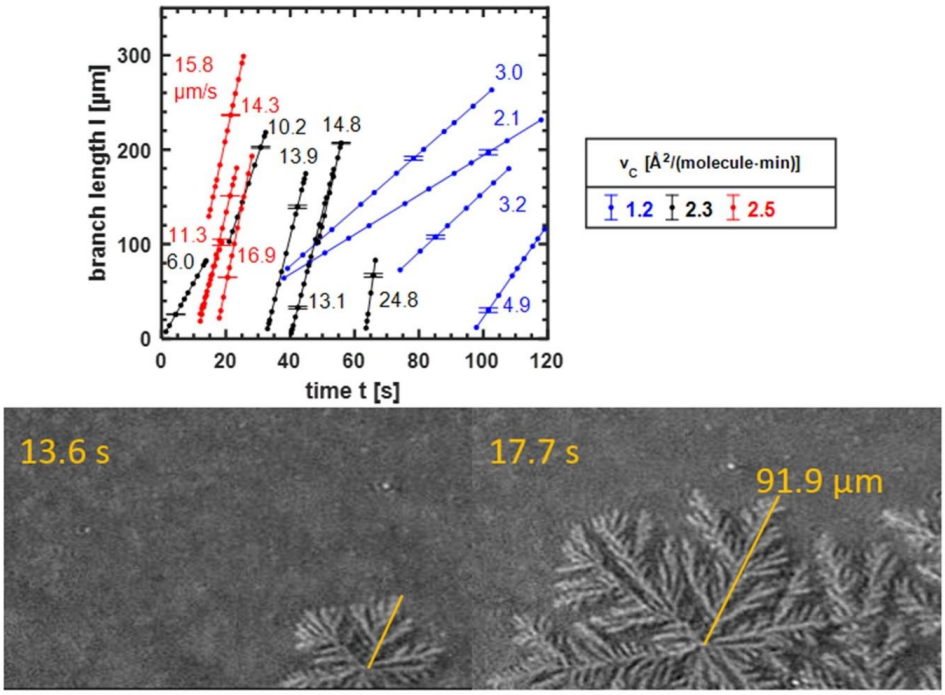

Figure 4. Bottom: Determining the length of a main branch at different times from BAM images of an erucic acid monolayer compressed at $v_C = 2.5$ Å^2/(molecule · min)) (experimental conditions as in Figure 1). Top: The length of the main branch of different domains in dependence on the time t. Three monolayers were analyzed, each with a different compression speed v_C as indicated. The lines are linear fits, whose slopes correspond to the constant growth velocity v_R as indicated. Exemplary error bars are included. For each monolayer, $t = 0$ s refers to the first observation of a domain. For a selected domain, the lowest value of t corresponds to the first observation of this domain, when it is still very small.

A typical video of this study contains the images during the complete compression of the erucic monolayer at a defined compression velocity. We focus on the part of the movie which shows the nucleation until the domains reach a very high surface coverage, when the different side branches can no longer be resolved. After a contrast-enhancement procedure, the boundaries of the domains were analyzed in detail. To determine the growth speed, a selected domain was compared in the different frames of a movie. The formalism of the determination of v_C is illustrated in Figure 4 (bottom). The length of a main branch was measured with the software ImageJ, then the length was converted from pixels into micrometers. Every **50** ms the camera recorded one image. The growth speed v_C is the quotient of the increment in branch length, Δl per time increment, delta Δt. Domains often drifted out of the image section of the CCD camera, which limited the observation time. Furthermore, we focused on isolated domains to avoid domain distortion by adjacent domains.

The growth kinetics of the domains are further analyzed in Figure 4 (top). Three different monolayers with three different compression velocities v_C were analyzed. The slowest compression speed leads to seaweed domains, the other ones to dendrites. Plotted is the time-dependent main branch length l. The main branches of dendrites showed the same growth speed. Therefore, each domain is represented by one main branch. One exception is the two upper blue lines (2.1 µm/s, 3.0 µm/s) which represent two branches of the same seaweed domain, growing in different directions. The different growth speed is attributed to the somewhat arbitrary structure of seaweed domains (cf. Figure 2). The length of each investigated main branch increases linearly with time. Lines in Figure 4 (top) are least-square fits; the slope corresponds to the growth speed v_R, indicated by the numbers beside the respective lines. Therefore, each main branch exhibits a constant growth speed v_R. However, the domains grown at a higher compression velocity v_C show a faster growth speed v_R. If one monolayer is considered, the main branches of domains that nucleated at later times grow faster (cf. Figure 4, top). Note that later times indicate lower molecular areas and higher excess lateral pressure. Depending on the film parameters, the growth speed v_R varies by an order of magnitude, from 2.1 µm/s to 24.8 µm/s.

3.3.3. Dependence of Growth Speed v_R on Compression Velocity and Supersaturation

In Figure 5, the dependence of the growth speed v_R on the excess lateral pressure $\Delta\pi = \pi - \pi_\infty$ is quantified. There are two contributions to the excess lateral pressure $\Delta\pi$, the increase in the phase transition pressure π_t (cf. Figure 1) due to the compression velocity and the additional increase due to the non-flat coexistence regime. At the lowest compression velocity v_R, the growth of seaweed domains starts at low excess lateral pressures ($\Delta\pi \approx$ **0.5** nm), with the lowest growth velocity v_C observed (**2.1** μm/s). The growth speed of domains that nucleate later in the coexistence regime is about a factor of two larger. Monolayers that were subject to a larger compression velocity v_C show dendritic growth. The dendrites start to grow at larger excess lateral pressures $\Delta\pi$ than seaweed domains. The influence of the different domain growth kinetics on the growth speed v_R can be best seen at the excess lateral pressure $\Delta\pi \approx$ **2.0** − **2.4** mN/m. At this excess lateral pressure, the main branch of a seaweed domain grows at **4.9** µm/s, while the dendrite one grows twice as fast at 10.2 µm/s (cf. Figure 5) (respective compression velocities are 1.2 and 2.3 $\mathbf{Å^2}/(\text{molecule} \cdot \text{min})$).

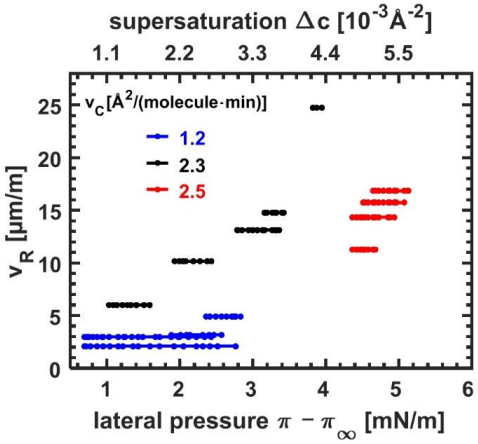

Figure 5. The growth speed v_R as a function of the excess lateral pressure $\Delta\pi = \pi - \pi_\infty$ for three monolayers compressed with three different compression velocity v_C as indicated. Additionally, shown is the supersaturation Δc in the LE phase. The data were derived from Figure 4.

The largest variation in growth speeds within one monolayer is observed for the monolayer which was compressed with v_C = **2.3** Å^2/(molecule · min) and exhibited dendrites. At the beginning of the coexistence regime, at low excess lateral pressure (**1** mN/m), the growth speed is **6.0** µm/s. At the end of the coexistence regime, the excess lateral pressure has quadrupled (**3.8** mN/m), and so has the growth speed (24.8 µm/s). A slightly larger compression velocity (**2.5** Å^2/(molecule · min)) leads to delayed nucleation at an excess pressure of **4.2** mN/m and a large growth speed, which varies little during further compression (between 11.3 and **16.9** μm/s).

In Appendix A, the supersaturation $\Delta c = 1/A - 1/A_\infty$ is calculated in dependence on the excess lateral pressure $\Delta\pi = \pi - \pi_\infty$. A linear relationship could be derived for small excess lateral pressures, which are found in the coexistence regime of erucic acid (cf. Figure 1). A shift in $\Delta\pi$ of 1 mN/m corresponds to a change in supersaturation of around 1.1×10^3 Å^{-2}; or a relative change in the supersaturation of **2.6%**. This small change can have a pronounced effect on the growth speed if compression velocity and additional supersaturation in the coexistence are suitable. This observation is in agreement with theoretical predictions [13].

To summarize, seaweed domains occurring at a lower monolayer compression velocity nucleate at a lower excess lateral pressure than dendrites; their main branches have a smaller growth speed. Once the main branch of a domain starts to grow, its growth speed is constant. The growth kinetics are established when the branch is nucleated. The constant growth speed is independent of the domain's shape, fractal dimension, or growth class. Furthermore, for any monolayer, a shift toward higher growth speed occurs for branches nucleating at higher initial excess lateral pressures.

3.3.4. The Influence of Excess Lateral Pressure $\Delta\pi$ and Supersaturation Δc on the Tip Radius r

Tip radii r of the main branches are sketched in Scheme 1. To measure them, the video images have been contrast-enhanced, as described before. Once formed, the tip radius of a domain does not change, while the domain grows (until the domain leaves the field of view). Figure 6 shows the dependence of the tip radii on the lateral excess pressure for the three investigated monolayers with different compression velocities v_C. Always, the tip radii decrease with increasing excess lateral pressure (supersaturation, respectively). The highest reduction was found for the seaweed domains: the tip radius decreases from nearly 3 µm to 1.3 µm, while the lateral pressure increases by **2.2** mN/m. The tip radii of dendrites are smaller: they start at **1.2** µm and decrease to **0.95** μm.

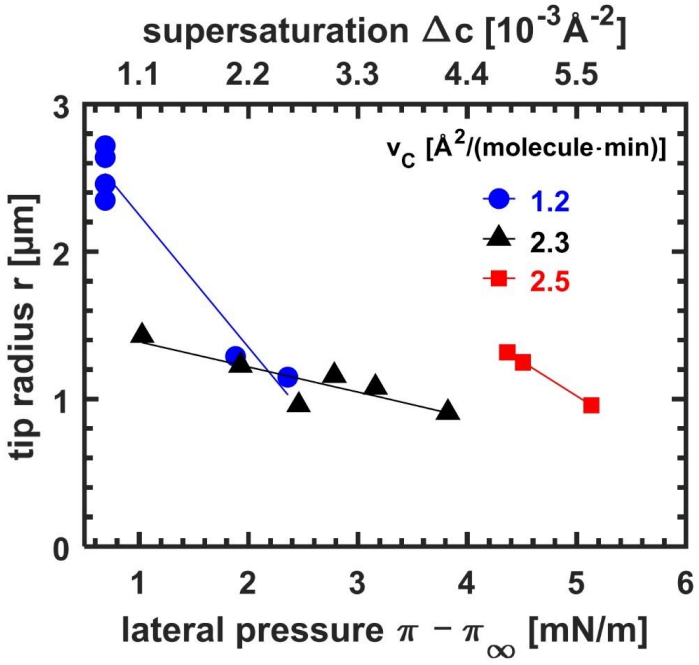

Figure 6. Tip radius r of domains from three different monolayers characterized by different compression velocity v_C (indicated) as a function of the excess lateral pressure $\Delta\pi = \pi - \pi_\infty$, the lateral pressure above the LE/LC phase transition of erucic acid (cf. Figure 1) at equilibrium conditions. The tip radius is shown at the lateral pressure where it could be first unambiguously resolved. With further compression of the monolayer, the tip radius did not change. As long as $\Delta\pi$ is small, it is proportional to the supersaturation $\Delta c = 1/A - 1/A_\infty$ in the LE phase, which is also shown.

For all structures, a linear decrease in the tip radii with increasing supersaturation was observed, in agreement with theoretical predictions [23,24]. In the past, the large tip radii of seaweed domains in lipid monolayers were taken as a hallmark of the seaweed domains [7]. We find that this correlation has to be used with some care, since the tip radius depends, for seaweed domains, sensitively on the lateral pressure. For dendrites, the dependence of the tip radius on the lateral pressure is weaker.

3.3.5. Side Branch Separation λ for Seaweed Domains and Dendrites

The side-branch separation is sketched in Figure 1. Theoretically, side branches of dendrites should be closer to each other than of seaweed domains [13]. A comparison of the BAM pictures seen in Figure 2 for seaweed-domains and dendrites suggests that the side branches of the seaweed domains appear more irregular, and their formation is more arbitrary. Furthermore, they are farther apart. To quantify this behavior, the side branch separation λ was measured for monolayers compressed at different velocities v_C. Figure 7 shows the findings, averaged over 20 measurements from different domains. The separation of the side branches is independent of the excess lateral pressure. It numerically confirms the visual observations. Indeed λ is significantly larger in the seaweed than in the dendritic growth regime. The large error bars found in the seaweed regime indicate the higher irregularity of the domain shape. This leads to the conclusion that the driving mechanism of irregular growth, propagating with a mode $q = 2\pi/\lambda$ at the LE/LC boundary of the growing domain, is different in the two growth regimes, in agreement with theoretical predictions [11,13,24].

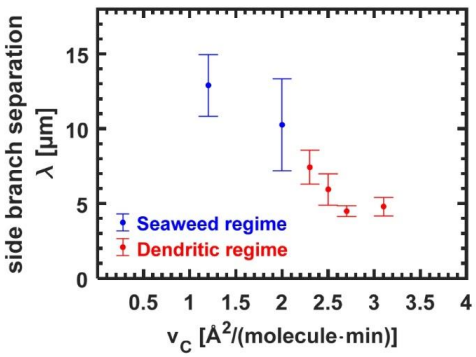

Figure 7. Side branch separation λ versus the compression velocity v_C for six different monolayers of erucic acid (cf. Figure 1). For each monolayer, about 20 different domains were analyzed. The domains nucleated at different lateral excess pressure $\Delta\pi$.

3.3.6. Influence of the Compression Velocity on the Flow in the LE Phase

Up to now, mesoscopic quantities of the domains have been analyzed, such as main branch growth velocity, the average separation between side branches, and the tip radius. With these parameters, the growth kinetics of seaweed domains could be characterized. The domain growth is made possible by the flow in the LE phase towards the domains. We cannot measure the flow next to the domains directly, but we can estimate the flow velocity far away from a domain, v_∞, but flowing toward the domain. We estimated v_∞ from the main branch growth speed v_R. The latter is influenced by the compression velocity v_C that is calculated from the velocity of the barrier of the Langmuir trough, $v_{Barrier}$, and the dimensions of the Langmuir trough.

A measurement was carried out in the coordinate system of the laboratory, hence the LE/LC boundary moves. Since the number of amphiphilic molecules is constant, one can state [13]:

$$v_\infty \cdot c_\infty = v_R \cdot (c_S - c_0) \quad (1)$$

with c_∞ the lateral concentration in the LE phase far away from the boundary of the domains. c_S denotes the surface concentration in the LC phase and c_0 the surface concentration in the LE phase close to the boundary domain.

For erucic acid, c_∞ has been calculated from the molecular area at the LE/LC phase transition (1/27.5 $\mathbf{Å^2}$), c_S from the molecular area determined by X-ray diffraction [16] in the LC phase (1/20 $\mathbf{Å^2}$). The surface concentration of the LE phase c_∞ is reduced close to the domain by a location-dependent excess surface concentration $\Delta c'$ to c_0 [25],

$$c_0 = c_\infty - \Delta c' \quad (2)$$

Rearranging Equation (2) and assuming that c_0 does not deviate much from c_∞ (true within 10%, cf. Table A1 in Appendix A), a dependency of the flow speed v_∞ from the growth speed v_R can be found:

$$v_R = \frac{c_\infty}{c_S - c_0} v_\infty \approx \frac{c_\infty}{c_S - c_\infty} v_\infty \quad (3)$$

Using the numbers from the erucic acid monolayers (cf. Figure 1), one obtains

$$v_R = \frac{\frac{N}{27.5}}{\frac{N}{20} - \frac{N}{27.5}} v_\infty \approx \mathbf{2.67} v_\infty \quad (4)$$

N denotes the number of molecules in the monolayer. Note that v_∞ is about a factor of three slower than the growth speed of the main branch of a domain. The values for the

flow velocity are listed in Table 1. v_∞ calculated from the different growth speeds is shown in Table 1, which contains representative values of v_R deduced from Figure 4 (top).

Table 1. Comparison of velocities influencing domain growth. v_C is the compression velocity calculated from the dimensions of the Langmuir trough and the barrier velocity $v_{Barrier}$. v_R is the growth velocity of the main branch and v_∞ the flow velocity in the LE phase of molecules far away from the domain, yet flowing already toward the domain.

v_C [Å^2/(molecule · min)]	$v_{Barrier}$ [cm/min]	$v_{Barrier}$ [µm/s]	v_R [µm/s]	v_∞ [µm/s]
1.2	0.46	76.67	2.1–4.9	0.8–1.2
2.3	1.08	180.00	6.0–24.8	3.8–5.5
2.5	1.20	200.00	11.3–16.9	4.3–6.3

Note that the velocity of the barrier is larger than the growth speed of the main branch. This is to be expected because the barrier speed moves in one dimension, however, the domains grow in two dimensions. Table 1 allows us to qualitatively compare v_R with $v_{Barrier}$:

$$v_{Barrier} \approx \mathbf{24.37} \cdot v_{R,Seaweed} \tag{5a}$$

$$v_{Barrier} \approx \mathbf{12.18} \cdot v_{R,Dendrite} \tag{5b}$$

This result is consistent with the experimental observation that the growth speed of domains is higher than the barrier velocity. It also suggests that dendrites grow generally faster than seaweed domains.

$$\frac{v_{R,\ Dendrite}}{v_{R,Seaweed}} \approx \mathbf{2} \tag{6}$$

This shows that the hydrodynamic flow of the subphase causes a larger growth velocity.

4. Conclusions

We used uncharged monolayers of erucic acid to describe the different growth instability classes. Theoretically, seaweed growth is predicted when lipid diffusion dominates, whereas dendritic growth is expected when adjunctive diffusion contributes to the lipid movement [13]. The monolayer was especially suitable for these studies because in the LE/LC coexistence region, the lateral pressure and, thus, the supersaturation increased. By varying the compression speed, either seaweed or dendritic growth was obtained.

Using Brewster Angle Microscopy (BAM, Accurion, Göttingen Germany), we analyzed the shape of the domains. The fractal dimension of seaweed domains was lower than that of dendritic domains, a feature described for a few other lipid monolayers [7]. The main branches of seaweed domains have a smaller growth speed than dendrites and the separation of the side branches is larger and shows more scatter. The tip of the main branch has a larger radius.

We compared the domains of monolayers compressed with the same compression velocity, but which nucleated at different degrees of supersaturation within the LE/LC coexistence regime. With increasing supersaturation (excess lateral pressure), the radii of the tips of the main branches decreased while their growth speed increased. The former feature has been predicted theoretically [23,24], the latter is new (to the best of our knowledge). In addition, the main branches of dendrites have a growth speed of about a factor of two greater than the main branches of seaweed domains. The faster growth speed is seen as evidence of adjunctive flow.

Finally, we would like to compare the unidirectional compression velocity of the monolayer (**75** μm/s to 200 µm/s) with the speed of blood (between **500** μm/s and **2.5** $\times$ **10^5** μm/s). These numbers suggest that the subphase does influence lipid movement. We find that the detailed study of domain growth in lipid monolayers is a tool to explore the different flow mechanisms which cause lipid movement in biological membranes.

Author Contributions: Conceptualization, F.G., H.A. and C.A.H.; methodology, F.G., H.A. and C.A.H.; software, F.G.; validation, F.G.; formal analysis, F.G.; investigation, F.G., H.A., H.W. and C.A.H.; resources, F.G., H.W. and C.A.H.; data curation, F.G. and H.A.; writing—original draft preparation, F.G. and C.A.H.; writing—review and editing, F.G. and C.A.H.; visualization, F.G. and C.A.H.; supervision, H.A., H.W. and C.A.H.; project administration, C.A.H.; funding acquisition, C.A.H. All authors have read and agreed to the published version of the manuscript.

Funding: This research was funded by Deutsche Forschungsgemeinschaft (DFG) in the Framework of the RTG 1947, grant number 231396381.

Acknowledgments: Cooperation within the CRC 1270 Elaine (SFB 1270/1,2–299150580) is gratefully acknowledged.

Conflicts of Interest: The authors declare no conflict of interest.

Appendix A

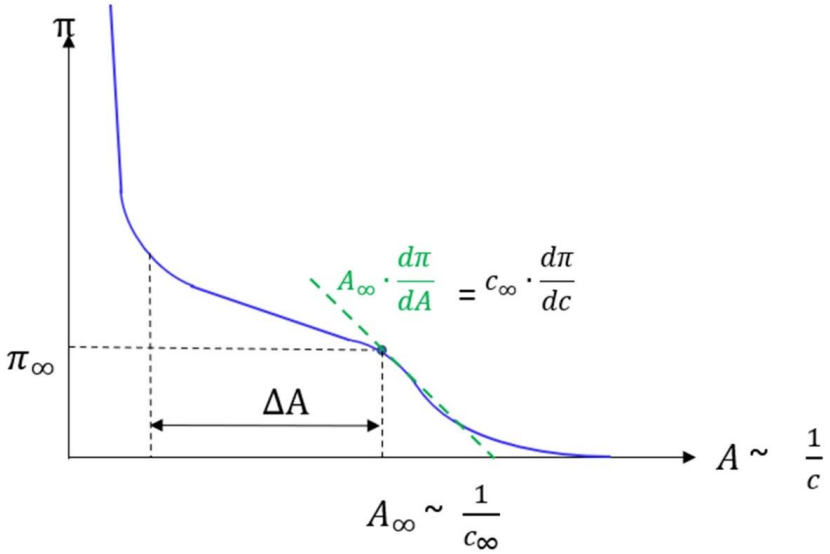

Scheme A1. The correlation between molecular area A and surface concentration c in the coexistence region of monolayers is indicated in an exemplary isotherm.

The number of molecules N per area in the coexistence region of the LE/LC phase transition is constant during monolayer compression. Therefore, the concentration c can be expressed as the inverse of the molecular area increase in units of Å^{-2}.

$$c = \frac{1}{A} \tag{A1}$$

The high compression speed v_R leads to an increased concentration Δc in the LE-phase, the supersaturation. It can be calculated as follows:

$$\Delta c = c - c_\infty = \frac{1}{A} - \frac{1}{A_\infty} = \frac{-\Delta A}{A_\infty \cdot A} \tag{A2}$$

with A_∞, c_∞ the phase transition molecular area and density, respectively. From the isotherms shown in Figure 1, it can be seen that this excess concentration close to the phase transition pressure π_∞ is always connected to an increased pressure $\Delta\pi = \pi - \pi_\infty$.

ΔA is the associated molecular area increase. Using the compression modulus κ a linear dependency of ΔA from $\Delta\pi$ can be found [14,26]:

$$\kappa = -A_\infty \frac{d\pi}{dA} = -A_\infty \frac{\Delta\pi}{\Delta A} \tag{A3}$$

Solving Equation (A3) for ΔA yields:

$$\Delta A = -A_\infty \frac{\Delta\pi}{\kappa} \tag{A4}$$

The calculation is applied to the data of the isotherms of erucic acid shown in Figure 1. For the specified experimental conditions (pH, temperature), the molecular area A_∞ at the phase transition is

$$A_\infty = \mathbf{27.5\ Å^2} \tag{A5}$$

The compression modulus κ was calculated numerically according to Equation (A3). Close to the phase transition pressure at equilibrium conditions, π_∞, one obtains $\kappa = \mathbf{39.2}$ mN/m (cf. Scheme A1). Therefore, in the LE phase the relationship between the molecular area decrease ΔA and the lateral pressure increase $\Delta\pi$ is

$$\Delta A = A - A_\infty = -\frac{\mathbf{27.5}}{\mathbf{39.2}}\Delta\pi = \mathbf{0.702 \cdot \Delta\pi}, \text{ with} \pi \text{ in [mN/m]} \tag{A6}$$

Values representing the coexistence regime of erucic acid (cf. Figure 1) are given in Table A1. Even at the highest lateral excess surface pressure of $\approx$ **5** mN/m, the normalized supersaturation is small ($\Delta c/\Delta c_\infty \leq \mathbf{15\%}$). Therefore, a linear relationship for lateral pressures up to 4 mN/m is reasonable, as shown in Figure A1.

Table A1. The measured molecular area A of erucic acid in the coexistence regime (cf. Figure 1), $\Delta A = A - A_\infty$, the supersaturation Δc (calculated with Equation (A2)) and the normalized supersaturation $\Delta c/c_\infty$ (calculated from Equation (A6)), for an excess lateral pressure $\Delta\pi = \pi - \pi_\infty$.

$\Delta\pi$ [mN/m]	A [Å^2]	ΔA [Å^2]	Δc [Å^{-2}]	$\Delta c/c_\infty$
0	27.50	0.00	0.0000	0.000
0.4	27.22	0.28	0.0004	0.010
1	26.80	0.70	0.0010	0.026
2	26.10	1.40	0.0020	0.054
3	25.40	2.10	0.0030	0.083
4	24.70	2.81	0.0041	0.114
5	24.00	3.51	0.0053	0.146
6	23.30	4.21	0.0066	0.181

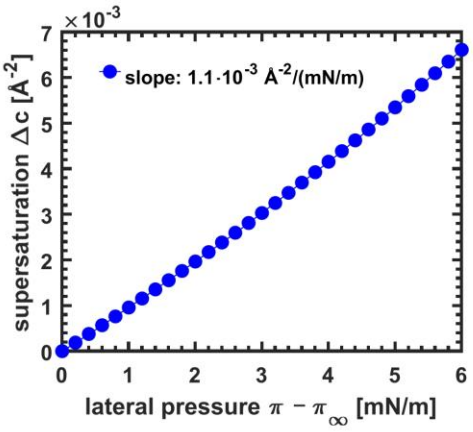

Figure A1. Supersaturation Δc in dependence of $\Delta\pi = \pi - \pi_c$, the lateral pressure above the LE/LC phase transition at equilibrium conditions, of erucic acid of Figure 1.

Appendix B

Determination of the Fractal Dimension

A well-established method to determine the fractal dimension (Minkowski-Bouligand dimension) numerically is the box-counting method [27,28]. Herby, a grid with a certain lattice constant is laid over a picture, containing the structure to be analyzed. The number of square boxes N covering the interface of the boundary of the structure is counted. Then, the box size R is altered and the number of boxes is reevaluated. Thereby the size of the picture acts as an upper limit of the box size and the pixel size as a lower limit, respectively. The fractal dimension can now be determined by plotting the number of the boxes covering the boundary versus the size of these boxes, using a double logarithmic representation, and then calculating the slope of the graph in the linear regime.

Such a box-counting algorithm has been developed by F. Moisy [17]. The code was slightly customized for the BAM pictures. The procedure is the following: In the first step the algorithm reads in the contrast-enhanced black and white picture as binary matrix C: every white pixel belonging to the structure is set to one and every black pixel associated with the background is set to zero. In the second step, the algorithm counts the number N of D-dimensional boxes of size R needed to cover the nonzero elements of matrix C, in the manner described above. The box sizes are powers of two, i.e., $R = 1, 2, 4 \ldots 2^P$, where P is the smallest integer such that the bigger value of either length (columns) or width (rows) of $C \leq 2^P$. If the size of C in any dimension is smaller than 2^P, C is padded with zeros, respectively to reach size 2^P (e.g., a 320-by-200 image is padded to 512-by-512). This allows processing pictures of arbitrary size with little effort. The algorithm has been implemented in a home-written Matlab routine, which allowed analyzing a complete BAM movie in one go. Typical boxplots of seaweed and dendritic structures are depicted below (Figures A2 and A3).

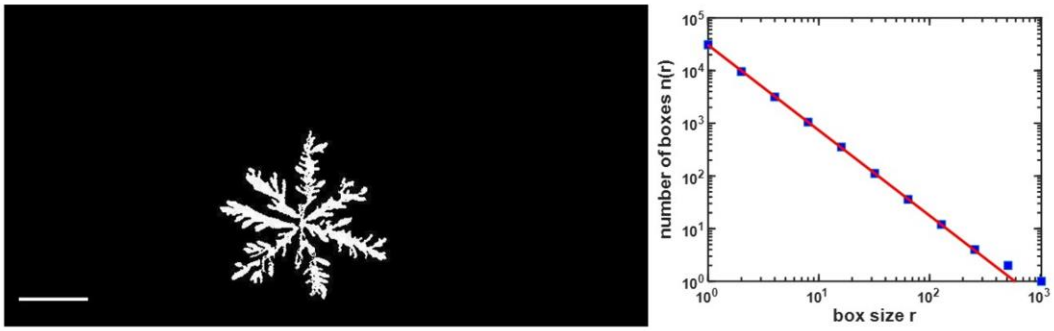

Figure A2. Left: The contrast-enhanced black and white picture of a typical seaweed structure at $t = 49.9$ s. The scale bar is **100** µm. **Right**: The deduced boxplot leading to a fractal dimension of $D_F = 1.62 \pm 0.06$.

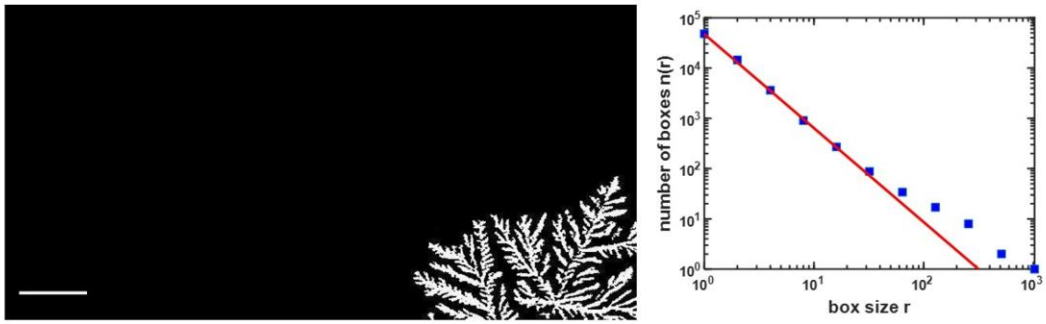

Figure A3. Left: The contrast-enhanced black and white picture of a typical dendrite at $t = 8.3$ s. The scale bar is 100 µm. **Right**: The deduced double logarithmic boxplot leading to a fractal dimension of $D_F = 1.87 \pm 0.15$.

References

1. Oliveira, O.N., Jr.; Caseli, L.; Ariga, K. The past and the future of Langmuir and Langmuir–Blodgett films. *Chem. Rev.* **2022**, *122*, 6459–6513. [CrossRef] [PubMed]
2. Kaganer, V.M.; Möhwald, H.; Dutta, P. Structure and phase transitions in Langmuir monolayers. *Rev. Mod. Phys.* **1999**, *71*, 779–819. [CrossRef]
3. Blume, A. Lipids at the air–water interface. *ChemTexts* **2018**, *4*, 1–25. [CrossRef]
4. Stefaniu, C.; Brezesinski, G.; Möhwald, H. Langmuir monolayers as models to study processes at membrane surfaces. *Adv. Colloid Interface Sci.* **2014**, *208*, 197–213. [CrossRef]
5. Miller, A.; Helm, C.A.; Möhwald, H. The colloidal nature of phospholipid monolayers. *J. Phys.* **1987**, *48*, 693–701. [CrossRef]
6. Miller, A.; Möhwald, H. Diffusion limited growth of crystalline domains in phospholipid monolayers. *J. Chem. Phys.* **1987**, *86*, 4258–4265. [CrossRef]
7. Gutierrez-Campos, A.; Diaz-Leines, G.; Castillo, R. Domain growth, pattern formation, and morphology transitions in Langmuir monolayers. A new growth instability. *J. Phys. Chem. B* **2010**, *114*, 5034–5046. [CrossRef]
8. Flores, A.; Corvera-Poire, E.; Garza, C.; Castillo, R. Pattern formation and morphology evolution in Langmuir monolayers. *J. Phys. Chem. B* **2006**, *110*, 4824–4835. [CrossRef] [PubMed]
9. Akamatsu, S.; Bouloussa, O.; To, K.; Rondelez, F. Two-dimensional dendritic growth in Langmuir monolayers of D-myristoyl alanine. *Phys. Rev. A* **1992**, *46*, R4504. [CrossRef]
10. Yoon, D.K.; Zhu, C.; Kim, Y.H.; Shen, Y.; Jung, H.-T.; Clark, N.A. Dendritic growth in a two-dimensional smectic E freely suspended film. *Mol. Syst. Des. Eng.* **2020**, *5*, 815–819. [CrossRef]
11. Mullins, W.W.; Sekerka, R.F. Morphological stability of a particle growing by diffusion or heat flow. *J. Appl. Phys.* **1963**, *34*, 323–329. [CrossRef]

12. Mullins, W.W.; Sekerka, R. Stability of a planar interface during solidification of a dilute binary alloy. *J. Appl. Phys.* **1964**, *35*, 444–451. [CrossRef]
13. Bruinsma, R.; Rondelez, F.; Levine, A. Flow-controlled growth in Langmuir monolayers. *Eur. Phys. J. E* **2001**, *6*, 191–200. [CrossRef]
14. Luviano, A.S.; Campos-Terán, J.; Langevin, D.; Castillo, R.; Espinosa, G. Mechanical properties of DPPC–POPE mixed langmuir monolayers. *Langmuir* **2019**, *35*, 16734–16744. [CrossRef]
15. Espinosa, G.; López-Montero, I.; Monroy, F.; Langevin, D. Shear rheology of lipid monolayers and insights on membrane fluidity. *Proc. Natl. Acad. Sci. USA* **2011**, *108*, 6008–6013. [CrossRef]
16. Vollhardt, D. Effect of unsaturation in fatty acids on the main characteristics of Langmuir monolayers. *J. Phys. Chem. C* **2007**, *111*, 6805–6812. [CrossRef]
17. Moisy, F. Boxcount (MATLAB Central File Exchange). 2008. Available online: https://ww2.mathworks.cn/matlabcentral/fileexchange/13063-boxcount (accessed on 18 June 2022).
18. Vysotsky, Y.B.; Belyaeva, E.; Fainerman, V.; Vollhardt, D.; Aksenenko, E.; Miller, R. Thermodynamics of the clusterization process of cis isomers of unsaturated fatty acids at the air/water interface. *J. Phys. Chem. B* **2009**, *113*, 4347–4359. [CrossRef]
19. Miller, A.; Knoll, W.; Möhwald, H. Fractal growth of crystalline phospholipid domains in monomolecular layers. *Phys. Rev. Lett.* **1986**, *56*, 2633. [CrossRef]
20. Li, J.; Miller, R.; Möhwald, H. Characterisation of phospholipid layers at liquid interfaces 2. Comparison of isotherms of insoluble and soluble films of phospholipids at different fluid/water interfaces. *Colloids Surf. A Physicochem. Eng. Asp.* **1996**, *114*, 123–130. [CrossRef]
21. Helm, C.A.; Moehwald, H. Equilibrium and nonequilibrium features determining superlattices in phospholipid monolayers. *J. Phys. Chem.* **1988**, *92*, 1262–1266. [CrossRef]
22. Mandelbrot, B.B. *The Fractal Geometry of Nature*; WH Freeman and Company: New York, NY, USA, 1982; Volume 1.
23. Ivantsov, G. Temperature Field Around a Spherical, Cylindrical, and Needle-Shaped Crystal, Growing in a Pre-Cooled Melt. In *Temperature Field Around a Spherical*; Akademiya Nauk SSR: Kiev, Ukraine, 1985; Volume 58, pp. 567–569.
24. Ihle, T.; Müller-Krumbhaar, H. Fractal and compact growth morphologies in phase transitions with diffusion transport. *Phys. Rev. E* **1994**, *49*, 2972. [CrossRef] [PubMed]
25. McFadden, S.; Browne, D.J. A generalised version of an Ivantsov-based dendrite growth model incorporating a facility for solute measurement ahead of the tip. *Comput. Mater. Sci.* **2012**, *55*, 245–254. [CrossRef]
26. Dhar, P.; Eck, E.; Israelachvili, J.N.; Lee, D.W.; Min, Y.; Ramachandran, A.; Waring, A.J.; Zasadzinski, J.A. Lipid-protein interactions alter line tensions and domain size distributions in lung surfactant monolayers. *Biophys. J.* **2012**, *102*, 56–65. [CrossRef] [PubMed]
27. Bouda, M.; Caplan, J.S.; Saiers, J.E. Box-counting dimension revisited: Presenting an efficient method of minimizing quantization error and an assessment of the self-similarity of structural root systems. *Front. Plant Sci.* **2016**, *7*, 149. [CrossRef] [PubMed]
28. Dehkhoda, P.; Tavakoli, A. Crown-Sierpinski microstrip antenna: Further reduction of the size of a crown square fractal. In Proceedings of the 2005 IEEE Antennas and Propagation Society International Symposium, Washington, DC, USA, 3–8 July 2005; pp. 247–250.

12.3. Article 3

Article 3

Influence of Surface Flows on the Shape of Fractal Domains

Florian Gellert, Heiko Ahrens and Christiane A. Helm

Langmuir

2023, Volume 39, 9078−9084

Published: June 26th, 2023

Supplementary information can be found in: DOI: 10.1021/acs.langmuir.3c00815

This research was originally published in Langmuir, **Gellert, F.**; Ahrens, H.; Helm, C. A., Oxidation of Unsaturated Phospholipids: A Monolayer Study. *Langmuir* **2023,** *39*(26), 9078−9084.

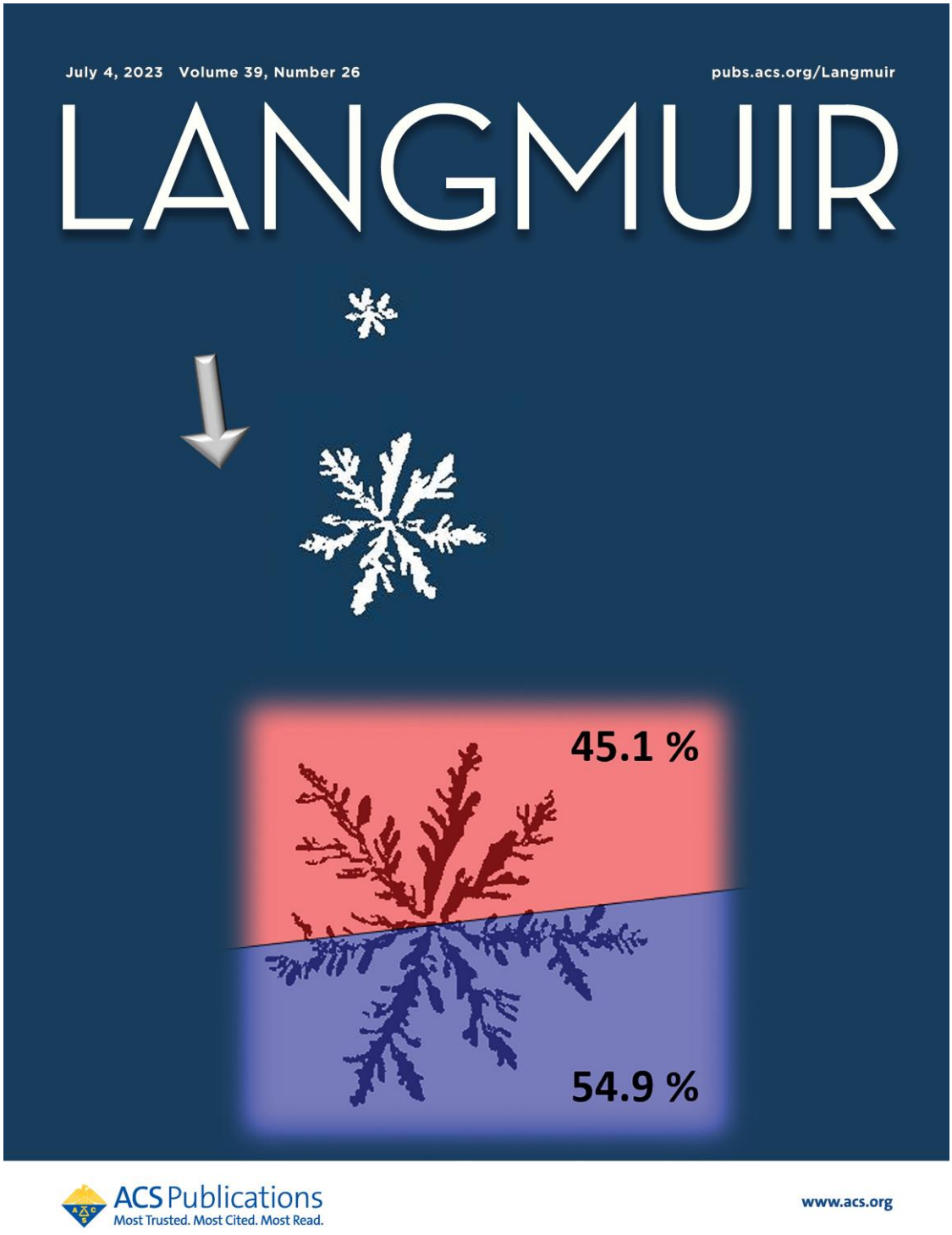
July 4, 2023 Volume 39, Number 26
pubs.acs.org/Langmuir
LANGMUIR
45.1 %
54.9 %
ACS Publications
Most Trusted. Most Cited. Most Read.
www.acs.org

LANGMUIR

pubs.acs.org/Langmuir Article

Influence of Surface Flows on the Shape of Fractal Domains

Florian Gellert, Heiko Ahrens, and Christiane A. Helm*

Cite This: *Langmuir* 2023, 39, 9078−9084 Read Online

ACCESS | Metrics & More | Article Recommendations | Supporting Information

ABSTRACT: Tidal breathing is associated with a 30% change of the surfactant-covered alveolar surface occurring about 16 times per minute. To model this highly dynamic process, erucic acid monolayers at the air−water interface were compressed fast. Brewster angle microscopy imaged the fractal liquid-condensed (LC) domains and quantified the surface flow in size, direction, and duration. Radial branch distribution of the domains has a minimum in the flow direction, as was shown with directionality histograms. The fast Fourier transform of the domains shows a preferential growth perpendicular to the flow direction. Additionally, at the beginning of the flow, the downstream side of the domain grows faster than the upstream side. Surface flows act on the mm to cm scale, cause an anisotropic flow in the liquid expanded phase surrounding the LC domain, and affect the overall domain shape. On the μm-scale, the dendritic or seaweed domains' branches were only slightly disturbed. These results may help to understand pulmonary surfactant layers.

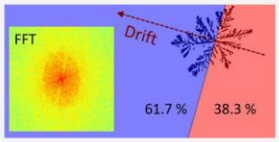

INTRODUCTION

Aqueous solutions covered with lipid monolayers occur in biology and medicine mainly in tear films[1] and in pulmonary alveoli.[2] Common to both systems is that the surface area increases and decreases very rapidly. In tear films, it happens when the eyes blink, and in the alveoli, when breathing.[3]

Breathing is a highly dynamic process: the respiratory rate of a resting adult lies between 12 and 20 respirations per minute,[4] such that compression and expansion of the pulmonary surfactant monolayer at the air−alveolus interface are very fast. The area change is 30%.

To study the biologically important properties of lipid films in vitro, Langmuir monolayers of lipids at the air-water interface have provided an experimentally accessible model system.[5] To reflect the biological reality, cholesterol and proteins have been added to the lung surfactant monolayer.[6] However, most of these publications focus on the equilibrium composition of the monolayer and do not investigate the dynamics.

Langmuir monolayers are a popular model system since temperature and molecular area are easy to control.[7] The latter can be adjusted by mechanical barriers, enabling compression or expansion of the lipid monolayer. Under suitable experimental conditions, compression leads to a phase transition from the liquid-expanded (LE) phase to a liquid-condensed (LC) phase.[8] Domain formation can be observed,[9] using fluorescence[10] or Brewster angle microscopy.[11,12]

In the present study, we use a Langmuir monolayer. The surface flow is induced by a high and constant compression speed. To optically observe the effects of surface flow, we imaged monolayers with domains as observed in lung surfactant monolayers.[5] We chose a system where the local flux in the LE phase affects the shape of the LC domain, i.e., we selected a system with fractal domains. A circular domain would be unsuitable because it shows only weak deformations (it may become elliptical).

Furthermore, we need a reason for flow within the LE phase. Continuous nucleation of domains causes short-term lateral inhomogeneities in the lateral density of the LE phase. The lateral density in the LE phase decreases around the newly formed domains. Within the LE phase, molecules move in the direction of the newly formed LC domain and cause flow. The magnitude of flow drops when the lateral density of the LE phase gets homogeneous. The next LC domain that nucleatess causes flow in new directions.

The LC domains in many phospholipid monolayers have a high line tension.[13] Therefore, the activation energy for nucleation is so high that all domains form simultaneously.[14] After nucleation, the domains grow simultaneously and have a similar nonfractal shape and area. Therefore, we consider phospholipid monolayers challenging for studying dynamics.

For continuous nucleation, a low line tension is helpful because a decrease in the line tension lowers the nucleation energy,[13] and enables continuous nucleation. That is why we chose monolayers of erucic acid at a suitable temperature and pH of the aqueous solution.[15] Other monolayers with optimized temperature and subphase[12,16] will show similar behavior. The influence of flow on the domains is investigated in terms of the magnitude, direction, and duration.

Most experiments of Langmuir−Blodgett monolayers are conducted near the thermodynamic equilibrium. This is

Received: March 25, 2023
Revised: June 9, 2023
Published: June 26, 2023

https://doi.org/10.1021/acs.langmuir.3c00815
Langmuir 2023, 39, 9078−9084

enabled by a slow compression speed of the monolayer, allowing the LE phase to relax when molecules condense into domains in the LC phase. Consequently, hydrodynamic flows are slow. Hence, the transport of molecules toward the phase boundary of domains is due to Brownian motion on a molecular length scale,[17] and the domain growth is dominated by lipid diffusion in the LE phase.[18]

A nonequilibrium system can be created by sudden pressure jumps[10,12] or by using high and constant compression speed.[15,19] Then, two different flows may occur: (i) convective flows in the subphase below the monolayer, which are caused by hydrodynamic coupling of the monolayer to subphase movement, known as the Marangoni effect (also important for the dynamics of tear films).[18,20] The convective flows are in the order of magnitude of the growth velocities of the branches of the LC domains.[18] (ii) Flows at the surface of the monolayer can be characterized by the drift velocity of the domains. The continuous nucleation of domains in the coexistence regime is attributed to such flows.[15] During monolayer compression, the proportion of LC phase growths but only the LE phase can be compressed, leading to anisotropic surface flows. As soon as the barrier stops, the monolayer film relaxes and the surface flows disappear. Flows can also originate from draughts. However, the latter can be eliminated for our experiments, since the complete Langmuir-Blodgett trough was shielded during experiments.

The first kind of listed flows, hydrodynamic coupling of the monolayer to subphase movement influences the morphology of the domains: they lead to a dendritic shape with higher fractal dimension, higher growth velocities, and well-defined side branching. In contrast, seaweed domains nucleate and form when domain growth is based on two-dimensional diffusion in the LE phase only.[15,19] The present work focuses on surface flows. The influence of surface flow on domain growth is analyzed using constant and variable barrier velocities to compress the monolayer. BAM videos of the growth of the domains were recorded during the compression of the monolayer. Contrast-enhanced BAM pictures at different recording times were analyzed with classical image analysis tools, two-dimensional Fast Fourier transform (FFT) spectra, and directionality histograms.

Description of the Experiment. Erucic acid monolayers at the air-water interface serve as a model system. The subphase is characterized by pH = 3 and the temperature is T = 10°C. At these conditions, the monolayer is uncharged and the isotherms show a transition from the LE phase to the LC phase at $\pi_\infty \approx 12$ mN/m with an unusually steep coexistence regime. At surface pressures above π_∞, BAM images show the formation and growth of seaweed or dendritic domains, depending on the compression speed v_C. The dimension of both types of domains is fractal. At constant v_C, the domain nucleation is continuous.[15] Seaweed-like domains were observed at low v_C. Their shape was arbitrary and side branches originated at large, not well-defined separations. The growth velocities of the main branches were slow; furthermore, only a few domains nucleated. However, at high compression speed v_C, dendrites with high nucleation rates, fast growth velocities, and small tip radii were observed. Side branch separation was small and well-defined. At the end of the LE/LC coexistence regime, the final size of the dendrites was smaller than that of the seaweed domains, since much more dendrites nucleated than seaweed domains.

In addition to the growth of the domains, we observed during each experiment domains drifting with uniform drift velocity v_D across the field of view. The direction of this surface flow was arbitrary and changed from monolayer to monolayer.

We suggest that the surface flow in the coexistence regime is correlated with the continuous nucleation of LC domains. The molecules in the LE phase are compressed with the increasing pressure in the LE/LC coexistence region and must also move toward the domain boundaries. Since the nucleation pattern is random, this leads to local inhomogeneous surface flows within the LE phase. In this study, we show that this local drift velocity v_D influences the symmetry and growth direction of drifting domains.

MATERIALS AND METHODS

Chemicals. Erucic acid with a purity ≥99% was used from Sigma-Aldrich (Merck KGaA), Darmstadt, Germany. The fatty acid was dissolved in chloroform (c = 0.1 mM) from Carl Roth, Karlsruhe, Germany. Pure 37% muriatic acid (HCl) was purchased from Merck, Darmstadt, Germany. It was then diluted in ultrapure water (Milli Q, Millipore, 0.054 μS) to obtain an acidic subphase of pH 3.

Methods. *Experimental Setup.* The development and growth of the erucic acid domains were analyzed using a Langmuir Blodgett trough and a Brewster Angle Microscope. The trough area was 30 × 3.5 cm^2 (Riegler & Kirstein, Potsdam, Germany). A thermostat (DC-30 Thermo-Haake, Haake Technik, Karlsruhe, Germany) provided isothermal conditions (±0.1 °C). The fatty acid solution was spread on the subphase with a 100 μL syringe (model 1710, Hamilton, Bonaduz, Switzerland). All experiments were performed in ambient air. The Langmuir Blodgett Trough was shielded from air draughts by an enclosure. A nanofilm_ultrabam Brewster Angle Microscope (Accurion, Göttingen, Germany) allowed the recording of real-time grayscale movies of the domain growth at 20 frames per second. Each frame corresponds to an overall focused image of a surface area of about 0.24 mm^2 (1360 pixels × 1024 pixels, spatial resolution of 2 μm). The camera of the BAM is positioned above the center of the Langmuir trough. Two movable barriers enable a symmetric monolayer compression simultaneously from the left and the right. The barrier speed has been varied between v_C = 77−314 μm/s for different monolayers.

Image Processing. Because of image distortion due to the employed Scheimpflug optics, all movies were rectified at first and then background-corrected with Accurion_Image (Accurion, Göttingen, Germany, version 1.2.3.). Contrast enhancement was performed using ImageJ[21] (version 1.53i9) and Matlab[22] (version R2021a). Further, the plugin "Overlay" provided by ImageJ was applied to measure the displacement of the domains.

We used a Matlab routine to calculate the two-dimensional FFT spectrum. The directionality diagrams were created using the ImageJ plugin "Directionality."[23] This plugin is based on Fourier spectrum analysis. For a square image, structures with a preferred orientation generate a periodic pattern at +90° orientation in the Fourier transform of the image, compared to the direction of the objects in the input image. The plugin chops the image into square pieces and computes their Fourier power spectra. The latter are analyzed in polar coordinates, and the power is measured for each angle using spatial filters.[23] Exemplary calculations of schematic dendrites are shown in the SI; they illustrate the relation between geometry, FFT, and directionality histograms (Figures S1−S4).

RESULTS AND DISCUSSION

Drift Velocity. To understand the influence of surface flows, we quantified the drift velocity as a first step. Figure 1 (left) shows two superimposed images of the same dendritic domain at different times. The dendritic domain grows and additionally moves within the field of view. The drift velocity v_D is calculated by dividing the displacement of the domain

https://doi.org/10.1021/acs.langmuir.3c00815
Langmuir 2023, 39, 9078−9084

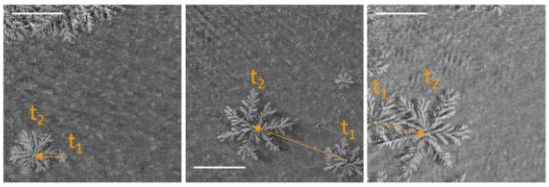

Figure 1. Determination of drift velocity for a dendrite (left) and two seaweed domains (middle and right) in the LE/LC region of three different erucic acid monolayers. Shown are contrast-enhanced, superimposed BAM images. The first image was taken at time t_1 followed by a second image at t_2. The deduced drift velocities are v_D = 38 μm/s with $\Delta t = t_2 - t_1$ = 1.45 s (left), v_D = 27 μm/s with Δt = 7.1 s (middle), and v_D = 7 μm/s with Δt = 14 s (right). The respective compression speeds were v_C = 182 μm/s (left), 305 μm/s (middle), and 212 μm/s (right). All scale bars are 100 μm.

center by the time increment. Given the known frame rate, the time interval is deduced from the respective video frames. In this way, we recorded the direction and absolute value of the drift velocity. Figure 1 (middle and right) shows drifting seaweed domains. The drift velocities range from v_D = 4 to 65 μm/s. We analyzed drifting domains from fourteen different monolayers. Figure S5 gives an overview of the measured drift velocities (absolute value).

Fourier Transformation of the Domains. To better characterize the domain shapes, the contrast-enhanced BAM images were further processed to obtain binary, black-and-white images. Then, we calculated the two-dimensional FFT spectrum (Figure 2). The FFTs show point symmetry. One of

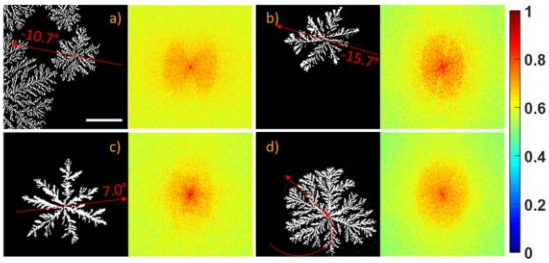

Figure 2. Different domains (left) and their corresponding two-dimensional FFT spectra (right). Contrast-enhanced BAM images of dendrites (a, b, d) and a seaweed domain (c) of four different monolayers are shown. The red arrow indicates the direction of the drift velocity. In images (a–c), the drift velocity during domain growth has a constant direction and decreases with consecutive images: v_D = 44 μm/s (a), 22 μm/s (b), and 4 μm/s (c). In image (d), the drift direction changes during domain growth ($v_{D,\,max}$ = 38 μm/s). The respective compression speeds were v_C = 180 μm/s (a), 162 μm/s (b), 77 μm/s (c), and 314 μm/s (d). Two-dimensional FFT spectra are presented as false-color images and are normalized to the dominant frequency. The scalebar (100 μm) shown in (a) can be applied to all images.

the lowest drift velocities found is v_D = 4 μm/s. Figure 2c shows a seaweed domain that grew in such a low surface flow. The derived FFT spectrum is symmetrical. One can discern the main branches with their six-fold symmetry. Here, the surface flow has no impact on the symmetry of the domain. The dendrite shown in Figure 2b was subject to a more significant drift velocity (v_D = 22 μm/s), flowing from the bottom right. Therefore, the dendrite is slightly tilted to the right. The corresponding two-dimensional FFT spectrum shows only a two-fold symmetry, with small incisions at ∼10° and ∼190°. During its growth, the dendrite shown in Figure 2a was exposed to a high drift velocity (v_D = 44 μm/s). The corresponding FFT spectrum exhibits a dumbbell shape. With the increased drift velocity, the incisions observed in Figure 2b become deep trenches in Figure 2a. In summary, we find that with increasing drift velocity v_D, the calculated FFT spectra show a two-fold symmetry and the incisions along the symmetry axis get deeper and wider.

Figure 2d shows a slightly different phenomenon: the dendrite was subject to a drift velocity which changed its direction during its growth. The deduced FFT spectrum is almost circular and has no discernible symmetry axis. Figure S6 in the SI shows the drift velocity's v_D dependence on the compression speed v_C. There is no direct correlation; however, note that the highest drift velocities were measured at the highest compression speeds.

Figure S4 demonstrates that the Fourier transform of long and thin lines leads to very low values in Fourier space. Conversely, short branches in real space lead to greater expansion in Fourier space. Therefore, the incisions in the Fourier spectra observed in Figure 2a,b,d indicate that the domains grow preferentially in the direction parallel to the incision.

Domain Growth Parallel and Perpendicular to the Drift Velocity. Since domains exposed to a drift velocity with a constant direction show a two-fold symmetry in their FFT spectra, we investigated the correlation between the direction of the symmetry axis and the flow direction employing directionality histograms. These histograms are based on contrast-enhanced BAM images, which are integrated along the radii passing through the center of the domain. They are analyzed in polar coordinates, which run from −90° to +90° due to their point symmetry. Typical examples are shown in the SI (Figures S1–S3). The correlation between the schematic dendrite and the directional histogram can be seen in Figure S1: narrow and high maxima are observed along the main branches (at −30°, +30°, and at ±90°). These maxima represent the main growth directions of the dendrites. In addition, broad, low maxima at ±60° represent the side branches. Incisions in the directionality histogram occur in directions where particularly little grows.

Figure 3 shows domains with a vector indicating the direction of the drift velocity and the deduced directionality histograms. The directionality histograms in Figure 3a–c show all pronounced minima, indicating the slowest growth at a specific angle. Invariably, the minimum coincides with or is very close to the flow direction (±8°). Typical is the dendrite and the deduced directionality histogram shown in Figure 3b. The position of the minimum almost coincides with the direction of the drift velocity v_D (−15.7°). The deviation is due to minor changes in the drift direction during domain growth. In the FFT of the same dendrite shown in Figure 2b, the slightly tilted symmetry axis has a minimum at +12°, almost perpendicular to the drift direction. Concluding, while the directionality diagram shows that the domain does not grow in the drift direction, the FFT shows that it grows preferential perpendicular to the drift direction. These two approaches to analyzing the domains are complementary, and the results reinforce each other.

https://doi.org/10.1021/acs.langmuir.3c00815
Langmuir 2023, 39, 9078−9084

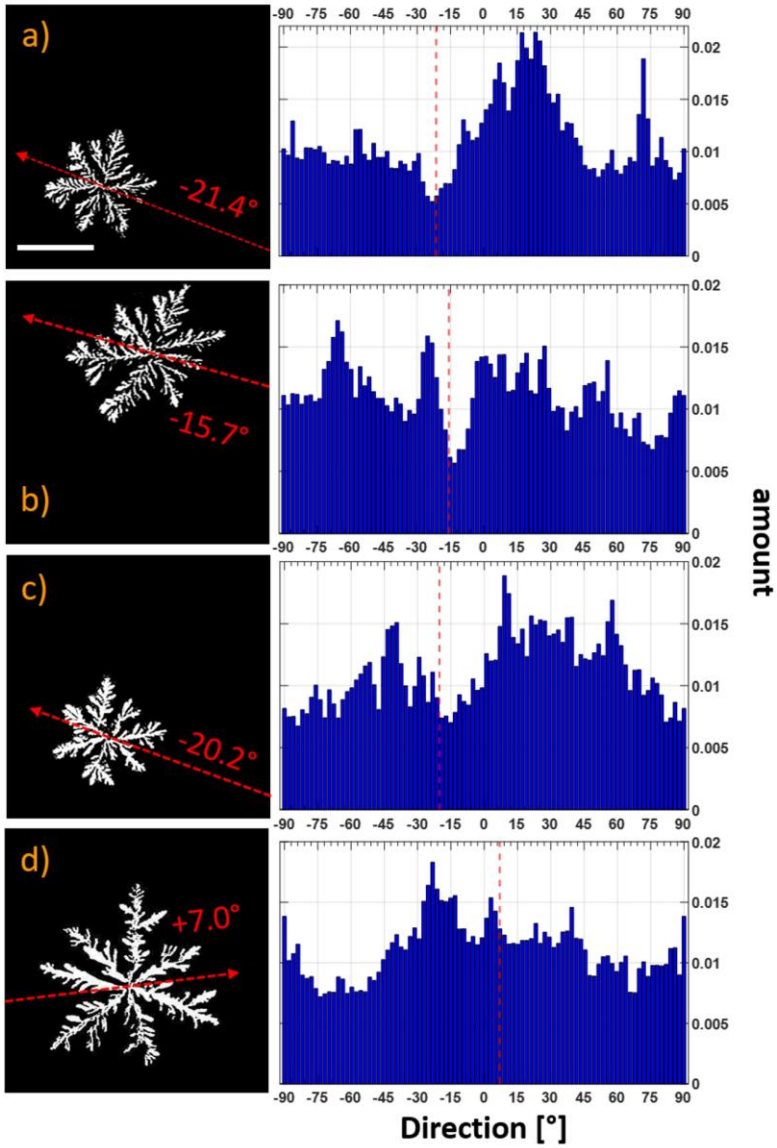

Figure 3. Influence of the direction of the drift velocity on the growth directions of dendrites (a, b) and seaweed domains (c, d). Left panel: contrast-enhanced BAM images of domains are shown together with red dashed arrows, indicating the direction of the drift velocity. Right panel: the deduced directionality diagrams. The red dashed line indicates the direction of the drift velocity and coincides within a few degrees for all images with the minima of the direction histograms (except for d). The scale bar shown in (a) is 100 μm and can be applied to all images. Drift velocities were v_D = 13 μm/s (a), 22 μm/s (b), 27 μm/s (c), and 4 μm/s (d). Compression speeds were v_C = 212 μm/s (a), 162 μm/s (b), 242 μm/s (c), and 77 μm/s (d). Note that the dendrite in (b) is the same as in Figure 2b and the seaweed domain in (d) coincides with the one shown in Figure 2c.

We conclude that the lipid diffusion in the LE phase toward the LE/LC boundary is affected by the drift velocity and is no longer isotropic. This effect is less pronounced for small drift velocities. The domain depicted in Figure 3d leads to no distinctive minimum in the directionality histogram, which is attributed to the small drift velocity (v_D = 4 μm/s). Note that the corresponding two-dimensional FFT (Figure 2c) shows no two-fold symmetry axis with incisions. More domains with their directionality histograms are shown in the SI (Figure S7). Again, large drift velocities led to pronounced minima in the directionality histograms.

So far, we have shown an increased growth perpendicular and a reduced growth parallel to the flow direction. Due to their point symmetry, directionality histograms cannot distinguish upstream and downstream growth. To find out if there are differences between upstream and downstream growth, the domains were split into a downstream side A_{down} and an upstream side A_{up}. The dividing line is drawn

https://doi.org/10.1021/acs.langmuir.3c00815
Langmuir 2023, 39, 9078−9084

perpendicular to the flow direction and through the domain's center. The area fraction of the downstream side is obtained by:

$$A_{\text{down}}\ [\%] = \frac{\text{Pixels}_{\text{down}}}{\text{Pixels}_{\text{down}} + \text{Pixels}_{\text{up}}} \times 100\% \quad (1)$$

and vice versa for the upstream side. Figure 4 shows BAM images of domains and the deduced area fractions. On average, the area fraction of the downstream side is always larger.

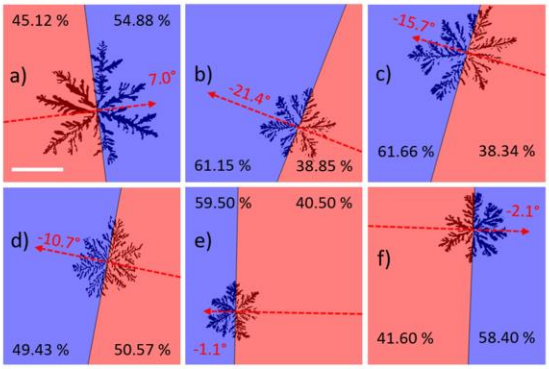

Figure 4. Representative seaweed domain (a) and dendrites (b–f) in the surface flow, ordered by increasing drift velocity v_D. Indicated are the direction of the drift velocity (red dashed arrow), the downstream (blue) and upstream side (light red) of the domains, and their respective area fraction. The domain images were obtained from contrast-enhanced BAM images. The scalebar (100 μm) shown in the top left image can be applied to all images. Drift velocities were v_D = 4 μm/s (a), 13 μm/s (b), 22 μm/s (c), 44 μm/s (d), 55 μm/s (e), and 65 μm/s (f). Compression speeds were v_C = 77 μm/s (a), 212 μm/s (b), 162 μm/s (c), 180 μm/s (d) 305 μm/s (e), and 314 μm/s (f). Note that the seaweed in (a) is the same as in Figures 2c and 3d; the dendrite in c is the same as in Figures 2b and 3b and the dendrite in b coincides with the one shown in Figure 3a.

Drift Duration. Analyzing many domains in multiple monolayers, it turned out that the drift velocity v_D is not the only parameter influencing the domain distortion. In the last paragraphs, we described the effects of absolute value and direction of v_D. Next, we focus on its duration t_D. The initial time was set to the point at which the drift direction was constant. Drift duration t_D was defined as the period between the beginning of a fixed drift direction and the time when the fractal domain was imaged. Note, that drift often takes longer than t_D, however when a domain moves out of the field of view, we cannot make a statement. The distribution of measured durations t_D is shown in Figure S8 in the SI. Most drifts were short, below 20 s (in detail: nine measurements below 20 s, five above).

Figure 5 shows the dependence of the area fractions A_{up} and A_{down} on the measured drift duration t_D (Figure 5, top) and the velocity v_D (bottom) for fourteen different monolayers. Domains with an area ratio of ~50:50 have been observed at 10 μm/s$\leq v_D \leq$ 45 μm/s. We conclude that the absolute value of the drift velocity v_D does not determine the anisotropy of the domains. Figure 5 (top) shows that most drifts did not last long (t_D < 16 s). Interestingly, the short drift times led to high area ratios A_{down} : A_{up} (cf. Figure 5, top). Longer, constant drift velocities lead to area ratios closer to 50:50. A domain that

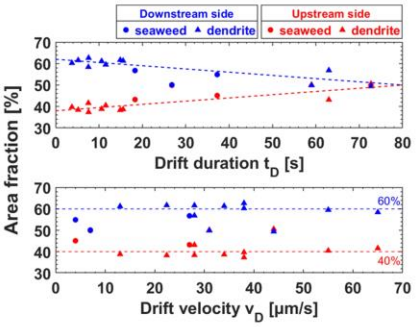

Figure 5. Dependence of the area fraction of the upstream and downstream side of domains on the drift duration t_D at the moment of observation (top) and drift velocity v_D (bottom). Seaweed (circles) and dendritic (triangles) domains are labeled. Each data point corresponds to a different monolayer. The dashed lines are guides to the eye.

experienced a long drift duration (t_D = 73 s) is shown in Figure 4d.

Dendrites form when the compression speed v_C is high, while seaweed domains form when v_C is small. Since the monolayer compression takes longer with low compression speeds, most dendrites were only observed for small drift durations, however, there were some exceptions. Concluding, the domain distortion occurs in the same way. It does not matter if a dendrite or a seaweed domain is considered.

Immediately after a change in drift direction, the domain grows preferentially in the downstream direction. When the drift velocity remains constant for long times t_D (40–80 s), growth gets isotropic. We conclude that the change in drift direction leads to temporarily different local flow velocities in the LE phase that can explain the large area ratios A_{down} : A_{up}. At long t_D (40–80 s), the surface flows upstream and downstream are similar, and upstream and downstream domain growth is identical. However, the two-fold symmetry in the 2-dimensional FFT spectra remains (cf. Figure 2). Therefore, perpendicular to the flow direction, domain growth remains pronounced. If the drift duration has an influence perpendicular to the flow direction, it is below our resolution.

Furthermore, it is noteworthy that v_D is not a criterion for whether dendrites or seaweed domains form. Both growth regimes occur at similar drift velocities v_D (cf. circles and triangles in Figure 5). This is somewhat unexpected since the drift velocity has similar values as the growth velocity of the main branches of the domains (below 5 μm/s for seaweed domains and between 6 and 25 μm/s for dendrites).[15] We did not observe any change in the growth velocity of the domain branches at different drift velocities.[15] Therefore, we conclude that the mechanisms which lead to surface flows and domain growth are different and superimposed. The drift velocities appear to be caused by large inhomogeneities in the LE phase. In contrast, the growth velocity of the main branches is due to the diffusion of lipids in the LE phase toward the domain edge. The lipid diffusion in the LE phase is strongly or weakly coupled to the flow in the subphase and leads to the different domain shapes.[18]

https://doi.org/10.1021/acs.langmuir.3c00815
Langmuir 2023, 39, 9078–9084

CONCLUSIONS

Surface flow has a pronounced impact on domain growth and the isotropy of fractal domains at the air−water interface. Therefore, it must be considered when looking at mechanisms determining domain shape. We used two-dimensional FFT and directionality histograms to monitor domain shapes. The directionality histograms were derived from the domains; their minima correlate with the flow direction, provided the drift velocity is large (above ≈10 μm/s). The depth and width of the minima are a measure of the reduced domain growth parallel to the drift direction. They depend on the absolute value of the drift velocity. Perpendicular to the drift direction, domain growth is preferred as the FFT shows. Furthermore, downstream growth is preferred for short drift times. However, downstream and upstream growth is similar for long drift times (40−80 s).

We conclude that the hydrodynamic flows in the subphase[18] and surface flows are superimposed, both act on lipids in the LE phase. Hydrodynamic flows act on μm scale and influence the domain morphology (distance between side branches, and tip radius) and the growth speed of the main branches. Hydrodynamic flows are independent of surface flows. Surface flows act on the mm to cm scale, cause an anisotropic flow in the LE phase surrounding the domain, and thus affect the overall domain shape.

At the air−alveolus interface, fast compression occurs during exhaling or coughing. The presented experiments suggest that the domain shapes are affected by the exhalation speed, but the processes at the μm-level and below (lipid aggregation to domain edge, local multilayer formation) are not affected.

ASSOCIATED CONTENT

Supporting Information

The Supporting Information is available free of charge at https://pubs.acs.org/doi/10.1021/acs.langmuir.3c00815.

> Examples include directionality diagrams and FFTs of simple, schematic dendrites, additional directionality histograms of analyzed domains, an overview of measured drift velocities and durations, and the (nonexisting) correlation between compression speed and drift velocity (PDF)

AUTHOR INFORMATION

Corresponding Author

Christiane A. Helm − *Institute of Physics, University of Greifswald, D-17489 Greifswald, Germany*; orcid.org/0000-0001-5181-1688; Email: helm@uni-greifswald.de

Authors

Florian Gellert − *Institute of Physics, University of Greifswald, D-17489 Greifswald, Germany*

Heiko Ahrens − *Institute of Physics, University of Greifswald, D-17489 Greifswald, Germany*

Complete contact information is available at: https://pubs.acs.org/10.1021/acs.langmuir.3c00815

Notes

The authors declare no competing financial interest.

ACKNOWLEDGMENTS

Discussions within and financial support of the CRC 1270 Elaine (SFB 1270/1,2-299150580) funded by the German Research Foundation (DFG) is gratefully acknowledged.

REFERENCES

(1) (a) Braun, R. J. Dynamics of the tear film. *Annu. Rev. Fluid Mech.* **2012**, *44*, 267−297. (b) Maïssa, C.; Guillon, M. Tear film dynamics and lipid layer characteristics—effect of age and gender. *Cont. Lens Anterior Eye* **2010**, *33*, 176−182.

(2) Grotberg, J. B. Pulmonary Flow and Transport Phenomena. *Annu. Rev. Fluid Mech.* **1994**, *26* (1), 529−571.

(3) (a) Zhang, Z.; Kleinstreuer, C. Transient airflow structures and particle transport in a sequentially branching lung airway model. *Physics of Fluids* **2002**, *14* (2), 862−880. (b) Kleinstreuer, C.; Zhang, Z.; Li, Z. Modeling airflow and particle transport/deposition in pulmonary airways. *Respiratory physiology & neurobiology* **2008**, *163* (1-3), 128−138.

(4) Chourpiliadis, C.; Bhardwaj, A. *Physiology, Respiratory Rate*; StatPearls Publishing: Treasure Island (FL), 2023.

(5) (a) Zasadzinski, J. A.; Ding, J.; Warriner, H. E.; Bringezu, F.; Waring, A. J. The physics and physiology of lung surfactants. *Curr. Opin. Colloid Interface Sci.* **2001**, *6*, 506−513. (b) Lalchev, Z.; Todorov, R.; Exerowa, D. Thin liquid films as a model to study surfactant layers on the alveolar surface. *Curr. Opin. Colloid Interface Sci.* **2008**, *13*, 183−193. (c) Castillo-Sánchez, J. C.; Cruz, A.; Pérez-Gil, J. Structural hallmarks of lung surfactant: Lipid-protein interactions, membrane structure and future challenges. *Arch. Biochem. Biophys.* **2021**, *703*, 108850.

(6) (a) Nylander, T. Interfacial structure of pulmonary surfactants revisited: Cholesterol and surface pressure effects. *Biophys. J.* **2022**, *121*, 3305−3306. (b) Post, A.; Nahmen, A.; Schmitt, M.; Ruths, J.; Riegler, H.; Sieber, M.; Galla, H. Pulmonary surfactant protein C containing lipid films at the air-water interface as a model for the surface of lung alveoli. *Mol. Membr. Biol.* **1995**, *12*, 93−99. (c) Krol, S.; Ross, M.; Sieber, M.; Künneke, S.; Galla, H.-J.; Janshoff, A. Formation of three-dimensional protein-lipid aggregates in monolayer films induced by surfactant protein B. *Biophys. J.* **2000**, *79*, 904−918. (d) Walther, F. J.; Gordon, L. M.; Waring, A. J. Advances in synthetic lung surfactant protein technology. *Expert Rev. Respir. Med.* **2019**, *13*, 499−501.

(7) (a) Marsh, D. Lateral pressure in membranes. *Biochim. Biophys. Acta, Rev. Biomembr.* **1996**, *1286*, 183−223. (b) Kaganer, V. M.; Möhwald, H.; Dutta, P. Structure and phase transitions in Langmuir monolayers. *Rev. Mod. Phys.* **1999**, *71*, 779−819. (c) Blume, A. Lipids at the air−water interface. *ChemTexts* **2018**, *4*, 3.

(8) Möhwald, H. Phospholipid and phospholipid-protein monolayers at the air/water interface. *Annu. Rev. Phys. Chem.* **1990**, *41*, 441−476.

(9) Möhwald, H.; Dietrich, A.; Böhm, C.; Brezesinski, G.; Thoma, M. Domain formation in monolayers. *Mol. Membr. Biol.* **1995**, *12*, 29−38.

(10) Miller, A.; Möhwald, H. Diffusion limited growth of crystalline domains in phospholipid monolayers. *J. Chem. Phys.* **1987**, *86*, 4258−4265.

(11) (a) Hoenig, D.; Moebius, D. Direct visualization of monolayers at the air-water interface by Brewster angle microscopy. *J. Phys. Chem.* **1991**, *95*, 4590−4592. (b) Flores, A.; Corvera-Poiré, E.; Garza, C.; Castillo, R. Pattern formation and morphology evolution in Langmuir monolayers. *J. Phys. Chem. B* **2006**, *110*, 4824−4835.

(12) Gutierrez-Campos, A.; Diaz-Leines, G.; Castillo, R. Domain growth, pattern formation, and morphology transitions in Langmuir monolayers. A new growth instability. *J. Phys. Chem. B* **2010**, *114*, 5034−5046.

(13) Blanchette, C. D.; Lin, W.-C.; Orme, C. A.; Ratto, T. V.; Longo, M. L. Using nucleation rates to determine the interfacial line tension of symmetric and asymmetric lipid bilayer domains. *Langmuir* **2007**, *23*, 5875−5877.

https://doi.org/10.1021/acs.langmuir.3c00815
Langmuir 2023, 39, 9078−9084

(14) Möhwald, H. Surfactant layers at water surfaces. *Rep. Prog. Phys.* **1993**, *56*, 653.
(15) Gellert, F.; Ahrens, H.; Wulff, H.; Helm, C. A. Seaweed and Dendritic Growth in Unsaturated Fatty Acid Monolayers. *Membranes* **2022**, *12*, 698.
(16) Suresh, K.; Nittmann, J.; Rondelez, F. Pattern formation during phase transition in Langmuir monolayers near critical temperature. *Europhys. Lett.* **1988**, *6*, 437.
(17) (a) Klingler, J. F.; McConnell, H. M. Brownian motion and fluid mechanics of lipid monolayer domains. *J. Phys. Chem.* **1993**, *97*, 6096−6100. (b) Saffman, P.; Delbrück, M. Brownian motion in biological membranes. *Proc. Natl. Acad. Sci. U. S. A.* **1975**, *72*, 3111−3113. (c) Sickert, M.; Rondelez, F.; Stone, H. Single-particle Brownian dynamics for characterizing the rheology of fluid Langmuir monolayers. *Europhys. Lett.* **2007**, *79*, 66005. (d) Vutukuri, H. R.; Hoore, M.; Abaurrea-Velasco, C.; van Buren, L.; Dutto, A.; Auth, T.; Fedosov, D. A.; Gompper, G.; Vermant, J. Active particles induce large shape deformations in giant lipid vesicles. *Nature* **2020**, *586*, 52−56.
(18) Bruinsma, R.; Rondelez, F.; Levine, A. Flow-controlled growth in Langmuir monolayers. *Eur. Phys. J. E: Soft Matter Biol. Phys.* **2001**, *6*, 191−200.
(19) Gehlert, U.; Vollhardt, D. Nonequilibrium structures in 1-monopalmitoyl-rac-glycerol monolayers. *Langmuir* **1997**, *13*, 277−282.
(20) Fischer, T. M.; Dhar, P.; Heinig, P. The viscous drag of spheres and filaments moving in membranes or monolayers. *J. Fluid Mech.* **2006**, *558*, 451−475.
(21) Schindelin, J.; Arganda-Carreras, I.; Frise, E.; Kaynig, V.; Longair, M.; Pietzsch, T.; Preibisch, S.; Rueden, C.; Saalfeld, S.; Schmid, B.; Tinevez, J. Y.; White, D. J.; Hartenstein, V.; Eliceiri, K.; Tomancak, P.; Cardona, A. Fiji: an open-source platform for biological-image analysis. *Nat. Methods* **2012**, *9*, 676−682.
(22) Schweizer, W. MATLAB® kompakt. In *MATLAB® Kompakt*; De Gruyter Oldenbourg, 2022.
(23) (a) Liu, Z.-Q. Scale space approach to directional analysis of images. *Appl. Opt.* **1991**, *30*, 1369−1373. (b) Tinevez, J.; Rueden, C.; Cardone, G.; Schindelin, J.; Eglinger, J.; Hiner, M. Directionality. ImageJ Plugin. 2018. https://imagej.net/plugins/directionality (accessed February 2023).

https://doi.org/10.1021/acs.langmuir.3c00815
Langmuir 2023, 39, 9078−9084

13. Eigenständigkeitserklärung

Hiermit erkläre ich, dass diese Arbeit bisher von mir weder an der Mathematisch-Naturwissenschaftlichen Fakultät der Universität Greifswald noch einer anderen wissenschaftlichen Einrichtung zum Zwecke der Promotion eingereicht wurde.
Ferner erkläre ich, dass ich diese Arbeit selbstständig verfasst und keine anderen als die darin angegebenen Hilfsmittel und Hilfen benutzt und keine Textabschnitte eines Dritten ohne Kennzeichnung übernommen habe.

Unterschrift des*der Promovend*in